NEUTRON ELECTRIC DIPOLE MOMENT AND DRESSED SPIN

BY

PING-HAN CHU

DISSERTATION

Submitted in partial fulfillment of the requirements
for the degree of Doctor of Philosophy in Physics
in the Graduate College of the
University of Illinois at Urbana-Champaign, 2011

Urbana, Illinois

Doctoral Committee:

Professor Douglas H. Beck, Chair
Professor Gordon A. Baym, Contingent Chair
Professor Jen-Chieh Peng, Director of Research
Professor Russell W. Giannetta

ABSTRACT

The neutron electric dipole moment (EDM) experiment has played a unique role in examining the violation of fundamental symmetries and understanding the nature of electroweak and strong interaction. A non-zero neutron EDM is one of direct evidence for CP and T violation and has the potential to reveal the origin of CP violation and to explore physics beyond the Standard Model.

A new neutron EDM experiment will be built to improve a factor of 100 by using a novel technique of ultra-cold neutrons(UCN) in superfluid ^{4}He at the Spallation Neutron Source (SNS) at the Oak Ridge National Laboratory (ORNL). In the experiment, ^{3}He in the measurement cell will be used as a neutron spin analyzer and a comagnetometer. The absorption between UCN and ^{3}He atoms will emit scintillation light in the superfluid ^{4}He depending on the angle between nuclear spins of two particles. Consequently, the neutron precession frequency can be derived by the scintillation light amplitude. Furthermore, the ^{3}He precession frequency can be measured by the superconducting quantum interference device (SQUID).

A dressed-spin technique will also be applied to measure the small precession frequency change due to a non-zero neutron EDM. The dressed-spin technique is used to modify the effective precession frequencies of neutrons and ^{3}He atoms to make them equal by applying an oscillatory field (dressing field) that is perpendicular to the static magnetic field. The phenomenon of the dressed spin for ^{3}He in a cell should be demonstrated before the proposed neutron EDM experiment. A successful measurement over a broad range of the amplitude and frequency of the dressing field was done at the University of Illinois. The observed effects can be explained by using quantum optics formalism. The formalism is diagonalized to solve the solution and confirms the data.

In addition, the application of the dressed-spin technique was investigated. The modulation and the feedback loop technique should be considered with the dressed-spin technique for the measurement of the small EDM effect. The modulation of the dressing field arbitrarily changes the relative precession frequency between UCN and ^{3}He. Through the feedback loop, the effective neutron precession frequency can be measured. The corresponding sensitivity of neutron EDM will be estimated. A future neutron EDM experiment could be improved if the dressed-spin technique can be carefully considered and applied.

ACKNOWLEDGMENTS

The sunshiny summer days in the campus remind me of the first day I arrived at the University of Illinois. It was a sunny day. Sky was blue and ground was green. All buildings looked shiny. It was my first time in the United States. Here was the starting point of my American dream. Since then, eight years have passed. I gained a lot and also lost a lot on the road. Honestly, I think this journey is still quite worthwhile. However, if you ask me whether I want to do it again, I guess one time is enough.

First of all, I wish to thank my advisor, Prof. Jen-Chieh Peng. The story began six years ago. The year, 2005, was not my year. I had a difficult time in another group. Prof. Peng accepted my transferring to the nuclear physics group. He gave me the opportunity to work with him on this challenging project, the neutron EDM. Since then, he has shared with me a lot of his knowledge and research insight helping me to succeed in the project. His personality as a physicist and his philosophy of life have also affected me for these years. His friendship and many interesting stories he shared with me will be joyful memories in my life.

Many people have participated and contributed a lot in the neutron EDM project at the University of Illinois, including Prof. Douglas H. Beck, Dr. Steven Williamson, Dr. Jacob Yoder, Andrea Esler, Dr. Steve Clayton, and the technical staff, Eric Thorsland and John Blackburn. Their help is crucial for the success of the UIUC dressed spin experiment. I enjoyed the moment when I discussed physics and experiment with them and learned a lot from them. I also wish to thank several summer students and undergrads for their sincere help, including, Bei-Zhen Hu, Yi Jiang, S. Y. "Jack" Ngan, Chun-Hong Sham and Lok-Hang So.

I would like to express my appreciation to my thesis committee members, including Prof. Gordon A. Baym, Prof. Douglas H. Beck and Prof. Russell W. Giannetta. They are experts in different fields of physics and provide diverse points of views to this project. I also thank the staff members in the Physics Department, especially Penny A. Sigler, Mike Suchor and Wendy R. Wimmer, who helped me a lot in different aspects like traveling, visa, etc. and made my life easier here.

I also wish to thank many members in the Nuclear Physics Group and the Physics Department of University of Illinois for their help and friendship. I appreciate the time I shared with my office-mates in Loomis 417, including Seth Ryland Ely, Mat Muether, Wah-Kai Ngai and Youcai Wang. We discussed a lot on physics and cultures between East and West. Some of them shared with me on their experience and

thought of Americans. Some of them discussed with me the politics and the experience in China and Taiwan. I also remember the days with my classmates, especially Yang Liu, Xin Lu and Zhenhua Yu, discussing homeworks and sharing dinners.

I would like to mention the friendship with several friends in the States, including Chien-Chia Cheng, Chih-Chun Chien, Shih-Chieh Hsu, Hsiang-Yeh Hwang, Kuo-Chun Pan, Yu-Shao Shiao, Shen-Fu Tsai, Chao-Hsin Wu, Man Hong Yung, etc. I remember those days with them playing badminton, having road trips, watching movies and drinking in the bars. They accompanied me in joyful as well as frustrating days.

I appreciate my parents for their support in the last few years. Even though I am the eldest son in my family, I needn't worry about the family. I could pursue my dream in the fundamental physics without too many concerns. I thank them for their understanding that I cannot always accompany them.

Finally, I would like to express my deep appreciation to my dear wife, Hao-Wen Ge. Meeting her is one of the best things in my life. I thank her for her understanding that I cannot always be with her when she needs me. She always encouraged me when I was struggling for jobs and supported me for continuing the career of research. I look forward to our new life in the future.

In the end, I would like to quote Robert Frost's poem, "Two roads diverged in a wood, and I– I took the one less traveled by, And that has made all the difference." I will be a postdoc in Prof. Haiyan Gao's group at the Duke University in this fall. The road in front of me is still uncertain. I wish the journey will be meaningful in the end.

TABLE OF CONTENTS

CHAPTER 1

INTRODUCTION : THE DREAM BEYOND THE STANDARD MODEL

The search for violation of fundamental symmetries is one of the most important methods in understanding nature. Most notably, tests of the discrete symmetries, charge conjugation (C), parity (P), and time reversal (T) have played a significant role in the development of the Standard Model. C, P and T had been respectively considered to be good symmetries. In 1956 Lee and Yang [47] first proposed the possibility of the P violation in the weak interaction and suggested some experiments to examine. Later in 1957, the first P violation was experimentally discovered by Wu *et al.* [87] in the β decay of ^{60}Co while C violation was also clearly observed in meson decays. However, the combination of C and P had been considered to be invariant until 1964 when the first CP violation in the decays of neutral kaons was discovered by Christenson, Cronin, Fitch and Turlay [16]. The result can be explained by the Kobayashi-Maskawa mechanism [42] which directly motivated the experiments of the CP violation in the B meson decay at Belle (at KEK, Japan)[1] and Babar (at SLAC, USA)[4].

One important reason to study CP violation is the matter-antimatter asymmetry in the Universe, the so-called baryon asymmetry of the Universe (BAU). The asymmetry can be defined in terms of the baryon-to-photon ratio $\eta \equiv n_B/n_\gamma$, where n_B is the net baryon density and n_γ is the photon density at freeze-out. The Wilkinson Microwave Anisotropy Probe (WMAP) measurement of the cosmic microwave background and Big Bang Nucleosynthesis (BBN) both determined $\eta \sim 10^{-10}$ [25]. In 1967 Sakharov [74] pointed out the three key ingredients for the BAU: (1) a violation of baryon number (B) conservation; (2) a violation of both C and CP symmetries; and (3) interactions under thermal non-equilibrium. Here the second condition will be addressed. There must be new physics beyond the Standard Model (SM) to account for the extra CP violation, since the BAU cannot be explained by the currently observed CP-violating sources in the kaons and the B mesons.

If the CPT symmetry [10][46][76] is conserved, the evidence of the CP violation implies T violation. The search for permanent electric dipole moment (EDM) becomes attractive since a non-zero EDM implies T violation. Therefore, the discovery of permanent EDMs could indicate new sources of CP violation. Any new physics beyond the SM has to pass the test of EDMs. Therefore, EDM searches remain compelling even after the Large Hadron Collider (LHC) at CERN produces evidence for new physics beyond the Standard Model.

In this chapter I will present the reason why EDM violates time reversal symmetry and the theoretical

background of the neutron EDM.

1.1 Overview of electric dipole moment

If an elementary particle has a nonzero EDM, the EDM must be parallel to the spin direction, which is the only direction available for describing the particle. The EDM $\vec{d}$ can be written as

$$\vec{d} \equiv \int d^3 r \rho_e(\vec{r})\vec{r} = \frac{d}{|\vec{S}|}\vec{S}, \tag{1.1}$$

where $\vec{S}$ is the spin and $\rho_e(\vec{r})$ is the charge distribution. Eq. 1.1 relates a vector $\vec{d}$ to an axial vector $\vec{S}$. Under the parity (P) transformation, the spin stays the same and $\vec{d}$ becomes $-\vec{d}$. Under time reversal (T) transformation, the neutron spin $\vec{S}$ becomes $-\vec{S}$ and $\vec{d}$ stays the same. Therefore, a nonzero EDM violates both parity and time reversal symmetries.

   The test of the parity symmetry was one of the purposes of EDM searching, suggested first by Purcell and Ramsey [65] in 1950 and again by Lee and Yang [47] in 1956. However, after Smith *et al.* [84] published the upper limit of the neutron EDM, a puzzle arose as to why EDMs are so small while parity violation is huge in the weak interaction. Later, Landau [45] pointed out that a non-zero EDM also violates the time reversal symmetry. If the CPT symmetry is conserved, the T violation implies CP violation. CP violation is known to be very small; therefore, it is reasonable to have such small values of EDMs even if the parity violation is huge.

   A permanent EDM can exist in a composite system such as a molecule due to its internal structure. It is important to understand why these EDMs do not violate time reversal symmetry. We consider a diatomic molecular consisting of two different atomic species. Two atoms can have an EDM along the axis linking two atoms. Meanwhile, the rotational angular momentum of the diatomic molecular is perpendicular to this axis. Therefore, $\vec{d}$ is perpendicular to $\vec{S}$, and it does not violate T symmetry.

1.2 Neutron EDM (nEDM) in Standard Model

There are two sources of CP violation in Standard Model (SM) which can generate EDMs, the strong interaction and the electroweak interaction. For the strong interaction, a nontrivial structure of vacuum in Quantum Chromodynamics (QCD)[6] allows a term in the QCD Lagrangian, called θ-term, which violates both P and CP symmetries. For the electroweak interaction, the complex phase in the Cabibbo-Kobayashi-Maskawa (CKM) matrix[42] can also generate CP violation leading to non-zero EDMs.

   The total QCD Lagrangian can be divided into two distinct parts: $\mathcal{L} = \mathcal{L}_0 + \mathcal{L}_\theta$ where the first term, $\mathcal{L}_0$, describes the quarks and gluons together with their interactions. The second term, called the θ-term, is

given by

$$\mathcal{L}_\theta = \theta \frac{g^2}{32\pi^2} G_{\mu\nu} \tilde{G}^{\mu\nu}. \tag{1.2}$$

$G^{\mu\nu}$ is the gluonic field strength tensor analogous to the electromagnetic field tensor $F^{\mu\nu}$ and the dual field tensor is defined by $\tilde{G}_{\mu\nu} = \frac{1}{2}\epsilon_{\mu\nu\alpha\beta}G^{\alpha\beta}$. The $G_{\mu\nu}\tilde{G}^{\mu\nu}$ term is analogous to $F_{\mu\nu}\tilde{F}^{\mu\nu}$ in quantum electrodynamics (QED) which is proportional to $\vec{E} \cdot \vec{B}$ in electromagnetism. Since $\vec{E} \cdot \vec{B}$ is CP-odd, this term violates CP symmetry. However, the term $F_{\mu\nu}\tilde{F}^{\mu\nu}$ is a total four-divergence so that it generates no observable effects in electromagnetism. In QCD, however, unlike the QED, the $G_{\mu\nu}\tilde{G}^{\mu\nu}$ term has nonzero net contribution to the QCD Lagrangian because of contribution from the interactions of the gluon.

The magnitude of the parameter θ is unknown; it seems natural to choose $\theta = 0$ as it cannot be determined by the theory itself. However, when the Higgs field acquires its vacuum expectation value, the Yukawa couplings with fermions produce the quark mass matrices. The diagonalization of these matrices produces a shift in θ, yielding

$$\bar{\theta} = \theta - ArgDet[\mathcal{M}_q] \tag{1.3}$$

where $\mathcal{M}$ is the original (nondiagonal) mass matrix. The effective $\bar{\theta}$ term can generate a neutron EDM at the order of $\bar{\theta} \times 10^{-15}$ e cm[6][23]. The upper limit of the neutron EDM of $|d_n| < 2.9 \times 10^{-26}$ e cm [5] implies $|\bar{\theta}| < 10^{-10}$. This extremely small value requires a huge fine tuning of a pure QCD angle θ and the phases of the quark mass matrices. This is the strong CP problem [14]. There are two main ideas to solve the problem: relaxation and cancellation. Peccei and Quinn proposed a solution involving an additional symmetry[58][59] to "relax" the angle to zero. This symmetry, however, predicts the existence of a light pseudoscalar, called axion, which has been sought after extensively without success for many years [89][90]. Another proposal by Nelson [54][55]and Barr [7][8] is to choose an appropriate quark mass matrix with a real value determinant. Because of the cancellation of the phases from the quark mass matrices, one can take the original QCD vacuum angle $\theta = 0$. Both Peccei-Quinn and Nelson-Barr's ideas can be extended in supersymmetric models. The strong CP problem remains a considerable enigma of the SM.

In the electroweak interaction of the SM, the single complex phase in the Cabibbo-Kobayashi-Maskawa (CKM) matrix[13][42] can also contribute to the neutron EDM. The neutron is composed of three valence quarks u, d and d, which can have non-zero EDMs. However, the single-quark EDM can only come from diagrams involving at least three-loop due to the unitarity of the CKM matrix [79]. This brings the quark contribution down to $\sim 10^{-34}$ e cm. One could also consider all three quarks simultaneously instead of dealing with a single quark. The diquark moments were analyzed by Nanopoulos et $al.$ [52]. They obtained a larger numerical estimate for the neutron EDM at $\sim 10^{-31}$ e cm since the two-loop diagrams can now contribute to the EDM when two quarks are involved. This value is six orders of magnitude below the

experimental upper limit [5].

1.3   Physics beyond the Standard Model

One advantage of using EDMs as a probe for new physics beyond the SM is that any signal of an EDM at a level greater than the SM prediction can be identified as a signal of physics beyond SM. Therefore, EDMs have been searched for in various systems extensively. The physical systems include point particles like e, μ, τ, nucleons like neutron, proton, atoms like Hg, Xe, Ti, Cs, Rn, Ra and molecules like TiF, YbF, PbO, etc., where each object has its own particular advantages[39]. The SM predictions for the magnitude of EDMs are far below the sensitivity of present measurements. However, several theories can induce larger EDMs through different mechanisms or a combination of them for fundamental particles and composite systems. Fig. 1.1[39] shows the relation between theoretical models and observed EDMs in various systems. The benefit of using neutrons is that the neutron is neutral and relatively simple, containing the information of quark and strong CP violation. Together with lepton experiments, which have dominant contributions from the electroweak, one may determine the origins of the EDM. The full set of EDM studies provides a powerful tool for understanding CP violation. Together with LHC studies, EDM searches may reveal the mystery of BAU.

One example of new theories is the minimal supersymmetric Standard Model (MSSM) of which the mass parameter space is shown in Fig. 1.2. The red region has been excluded by the Large Electron Positron Collider(LEP) at CERN, while the light blue region is ruled out by existing limits on the electron EDM. Black hashed regions are those that would lead to the observed BAU in the MSSM. The region that the LHC and the neutron EDM experiments can respectively access are also displayed. Consequently, the absence of the MSSM signal at the LHC would not exclude the possibility of MSSM. The destiny of MSSM could still be determined by future precise EDM experiments.
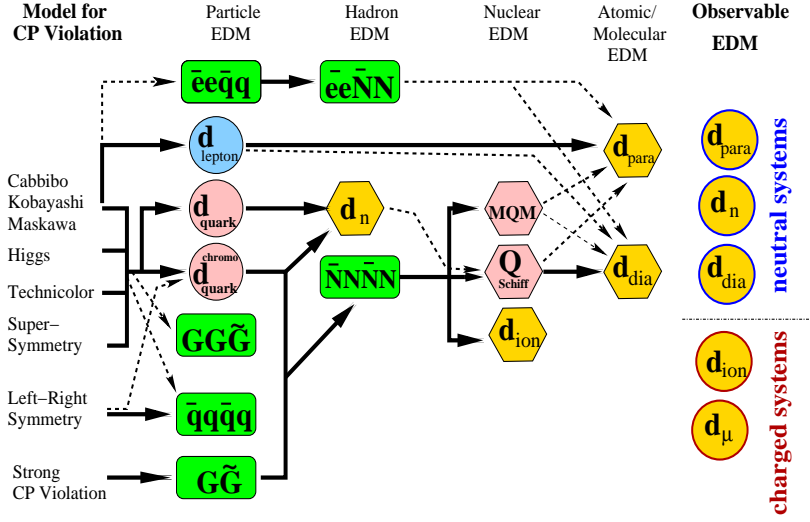
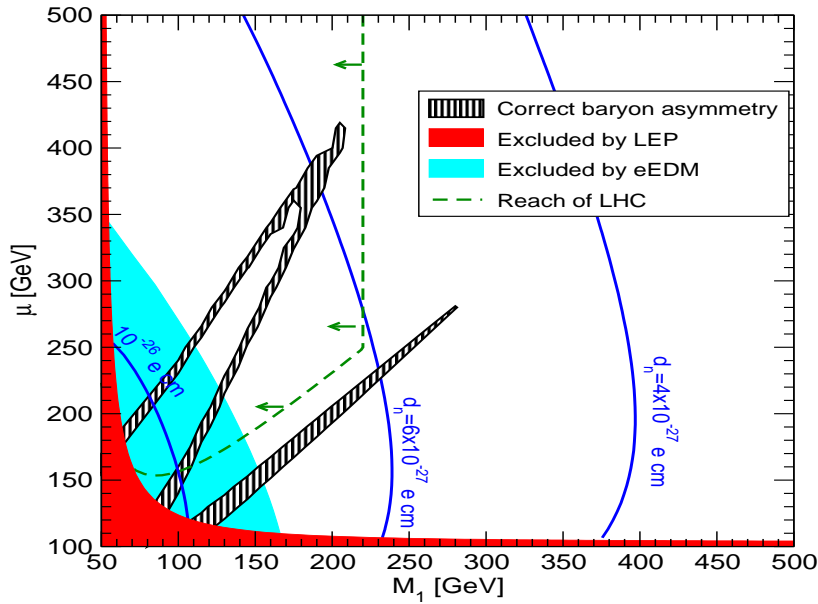Figure 1.1: The relation between models and observed EDMs[39].

Figure 1.2: Regions of the MSSM mass parameters μ and M_1 that govern the neutralinos consistent with the electroweak baryogenesis for the fixed CP-violating phase ϕ_μ, $\sin \phi_\mu = 0.5$ [73].

CHAPTER 2

EXPERIMENTAL TECHNIQUES FOR NEUTRON EDM

Almost all electric dipole moment (EDM) experiments detect EDM via the tiny Stark splitting [85] linearly induced by an electric field. The electric field (E_0) is either parallel or antiparallel to the constant magnetic field (B_0). The Hamiltonian of the system is

$$H = -(\mu \vec{B}_0 + d\vec{E}_0) \cdot \frac{\vec{S}}{|\vec{S}|},$$
(2.1)

where d and μ are the electric and magnetic dipole moments, and $\vec{S}$ is the angular momentum of the particle. For the ordinary magnetic Zeeman effect, an energy splitting due to the magnetic dipole moment and the magnetic field in the different directions $(\vec{B}_0 \parallel \vec{S}$ or $\vec{B}_0 \parallel -\vec{S})$ can cause a resonant frequency (Larmor precession frequency) at $\omega_0 = \frac{2\mu}{\hbar} B_0 \equiv \gamma B_0$, where γ is the gyromagnetic ratio. A change in the Larmor precession frequency due to the electric field can reveal the EDM value. The resonant frequency is given by

$$\omega_{res} = \frac{2}{\hbar}(\mu B_0 \pm dE_0).$$
(2.2)

The difference in the precession frequencies of neutrons placed in a strong $\vec{E}_0$ field parallel or antiparallel to B_0 is $\Delta\omega_{res} = 4\frac{dE_0}{\hbar}$, so that the value of the EDM is given by

$$d = \frac{\hbar \Delta\omega_{res}}{4E_0}.$$
(2.3)

For a typical experiment, a number of polarized particles (N) are stored in a cell and uniform magnetic and electric fields (E_0) are applied. The particle will precess for a certain amount of time (T). Using the uncertainty principle [1], the statistical uncertainty of the EDM, δd, is given by

$$\delta d = \frac{\hbar}{2E_0 T \sqrt{mN}}$$
(2.4)

where m represents the number of separate complete measurements [40]. Therefore, the goal of all experiments is to measure a small change in the Larmor frequency due to EDM and to reduce the systematic uncertainties such as the coupling of the magnetic dipole moment to the magnetic field.

_____
[1]See Appendix A.

The neutron EDM has been sought after for more than half a century. Purcell and Ramsey first pointed out the possibility of EDM [65] and used the data of Havens, Rabi and Rainwater's neutron scattering experiment [37] to get an upper limit of neutron EDM at $3 \times 10^{-18} e\ cm$. Seven years later, Smith, Purcell and Ramsey [84] published the improved upper limit of neutron EDM at $5 \times 10^{-20} e\ cm$ by using a neutron-beam magnetic resonance method which was invented by Alvarez and Bloch [3]. The precession frequency can be accurately measured by using the technique of the separated oscillatory field developed by Ramsey [67][72]. Since then, several neutron EDM experiments have been done and have improved the upper limit of neutron EDM significantly. For example, Shull and Nathan obtained an upper limit of $5 \times 10^{-22}\ e\ cm$ by using the method of Bragg diffraction of polarized neutrons off a CdS crystal [82]. Most later experiments used the neutron-beam magnetic resonance technique until the ultra-cold neutrons were introduced. The historical development is shown in Fig. 2.1 and the experiments are described in [62]. This chapter will review the main features of experimental techniques of the neutron EDM experiment proposed at the Spallation Neutron Source(SNS) at Oak Ridge National Laboratory.

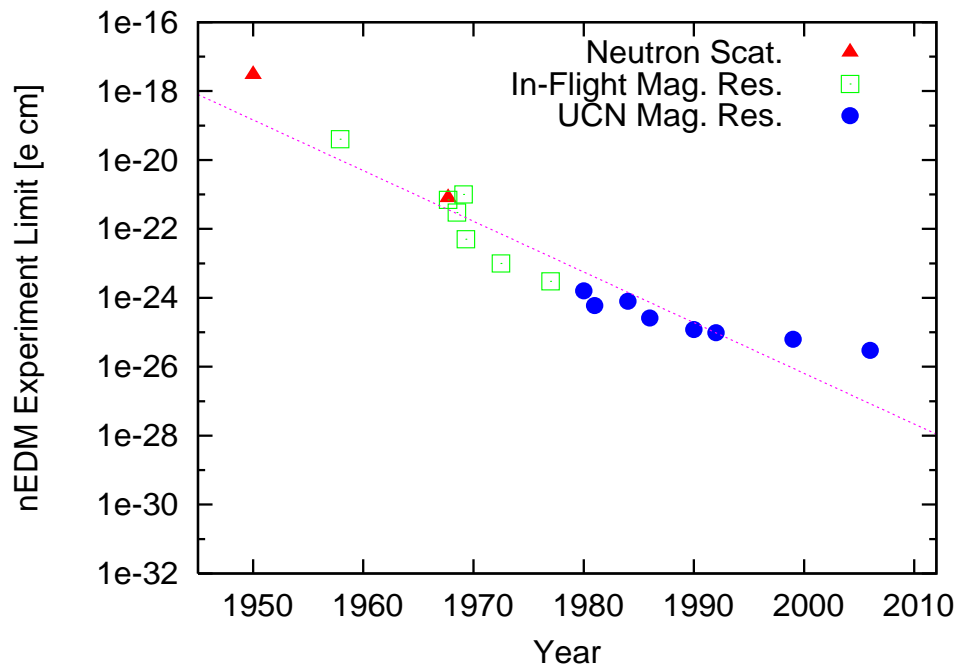Figure 2.1: Upper limits of neutron EDM as a function of year of publication.

2.1 Separated oscillatory fields

Smith, Purcell and Ramsey's pioneering neutron EDM experiment [84] used the Separated Oscillatory Fields technique [68][69][70] to free neutrons. The idea apparently arose when Ramsey was teaching undergraduates about the Michelson interferometer [60]. The technique is like a two-slit experiment with

the slits separated in time rather than in space [36].

The technique can be treated semiclassically. First, we discuss the $\pi/2$ pulse. Imagine a neutron with its magnetic moment (parallel to the spin) aligned parallel to a static homogeneous magnetic field, $\vec{B}_0$, in the longitudinal direction $\hat{z}$. A transverse oscillatory field $\vec{B}_1(t) = B_1 \cos(\omega t) \, \hat{x}$ is applied to the system. Then the total field is

$$\vec{B} = B_0 \, \hat{z} + B_1 \cos(\omega t) \, \hat{x}. \tag{2.5}$$

Ramsey solved the dynamics of the spin by using the semiclassical approach [83]. $\vec{B}_1$ can be decomposed into two rotating components, one rotating clockwise and the other counterclockwise, denoted in two equations:

$$\vec{B}_R = \frac{B_1}{2}(\cos \omega t \, \hat{x} + \sin \omega t \, \hat{y}), \tag{2.6}$$

$$\vec{B}_L = \frac{B_1}{2}(\cos \omega t \, \hat{x} - \sin \omega t \, \hat{y}). \tag{2.7}$$

By using Bloch equations [11],

$$\begin{aligned}
\frac{d\vec{\mu}}{dt} &= \vec{\mu} \times \gamma[B_0 \, \hat{z} + B_1 \cos \omega t \, \hat{x}] \\
&= \vec{\mu} \times \gamma[B_0 \, \hat{z} + \frac{B_1}{2}(\cos \omega t \, \hat{x} + \sin \omega t \, \hat{y}) + \frac{B_1}{2}(\cos \omega t \, \hat{x} - \sin \omega t \, \hat{y})],
\end{aligned} \tag{2.8}$$

where $\vec{\mu}$ is the magnetic moment and γ is the gyromagnetic ratio, the equation of motion of $\vec{\mu}$ is obtained.

If the system is transformed from the lab frame into the rotating frame at a frequency, ω, the equation becomes

$$\frac{d\vec{\mu}}{dt} = \vec{\mu} \times \gamma[(B_0 - \frac{\omega}{\gamma}) \, \hat{z}' + \frac{B_1}{2} \, \hat{x}' + \frac{B_1}{2}(\cos 2\omega t \, \hat{x}' - \sin 2\omega t \, \hat{y}')]. \tag{2.9}$$

In the situation $B_1 \ll B_0$, the counterclockwise field at 2ω is ignored in the "rotating wave approximation" (RWA), which ignores the high frequency term. Then

$$\frac{d\vec{\mu}}{dt} = \vec{\mu} \times \gamma[(B_0 - \frac{\omega}{\gamma}) \, \hat{z}' + \frac{B_1}{2} \, \hat{x}'] \equiv \vec{\mu} \times \gamma \vec{B}_{eff}. \tag{2.10}$$

If $B_1(t)$ is at the resonance of the Larmor frequency , i.e., $\omega = \omega_0 \equiv \gamma B_0$, the effective field is simply $\frac{B_1}{2} \, \hat{x}'$. The neutron in the rotating frame will see a fixed horizontal field and begin to precess about it. A magnetic moment at $\hat{z}'$-axis would precess in the $\hat{y}' - \hat{z}'$ plane about $\hat{x}'$-axis at frequency $\gamma B_1/2$ in the rotating frame. A $\pi/2$ pulse, which is applied for a period of time τ given by

$$\frac{\gamma B_1}{2}\tau = \frac{\pi}{2} \longrightarrow \tau = \frac{\pi}{\gamma B_1}, \tag{2.11}$$

can rotate the magnetic moment by 90° from the $\hat{z}$-axis to the $\hat{x} - \hat{y}$ plane.
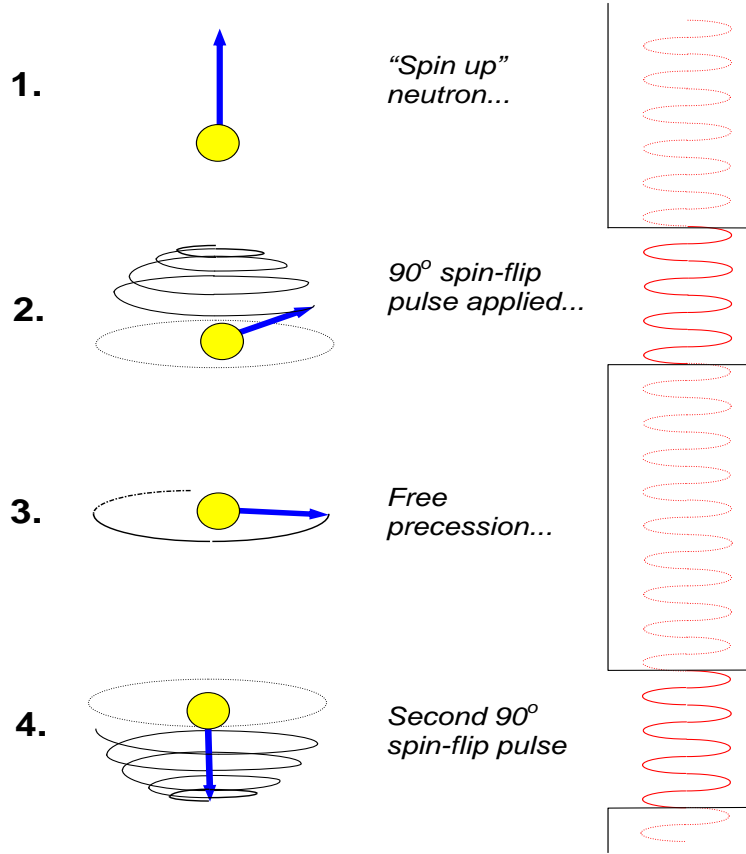

Figure 2.2: Ramsey's technique of separated oscillatory fields [36].

After the introduction on the principle of the $\pi/2$ pulse, we can discuss next the separated oscillatory fields technique. Following Fig. 2.2 [36], let us imagine a polarized neutron with a magnetic moment along $\hat{z}$ enters a region of static homogeneous magnetic field $B_0\,\hat{z}$. At the entrance, a $\pi/2$ pulse is applied, and the magnetic moment starts to spiral. Once the magnetic moment is reoriented to $\hat{x} - \hat{y}$ plane ($-\hat{y}'$-axis in the rotating frame), the oscillatory field $\vec{B}_1$ would be turned off. The magnetic moment starts to freely precess about the static field $B_0\,\hat{z}$ for some time $T \gg \tau$ before a second $\pi/2$ pulse is applied, which is coherent with the first one. If the frequency of the oscillatory fields matches the neutron's precession frequency (Larmor frequency), the second pulse will completely flip the magnetic moment of the neutron by another $\pi/2$ so that the magnetic moment will be aligned antiparallel to $\hat{z}$-axis.

If the frequency of the oscillatory fields and the Larmor frequency are slightly different, the magnetic moment will be off the $-\hat{z}$-axis in the end. Following the discussion in [40], one can derive that the

magnetic moment will precess about the effective field in the rotating frame:

$$\vec{B}_{eff} = (B_0 - \frac{\omega}{\gamma})\hat{z}' + \frac{B_1}{2}\hat{x}' = \Delta B\hat{z}' + \frac{B_1}{2}\hat{x}',$$

$$|\vec{B}_{eff}| = \sqrt{(\Delta B)^2 + (\frac{B_1}{2})^2}. \tag{2.12}$$

If $\Delta B \ll B_1$, the first $\pi/2$ pulse still can rotate the magnetic moment roughly from $\hat{z}$-axis to $\hat{x} - \hat{y}$ plane. After the $\vec{B}_1(t)$ is turned off, the effective field in the rotating frame is

$$\vec{B}_{eff} = \Delta B\hat{z}', \tag{2.13}$$

and the magnetic moment will precess about the $\hat{z}'$-axis at frequency $\gamma\Delta B$. For a time period T, a phase difference $\phi \approx \gamma\Delta BT$ will be accumulated. Therefore, the magnetic moment would not be perpendicular to the transverse field along $\hat{x}'$ in the rotating frame. The magnetic moment vector will be

$$\vec{\mu} = \mu(-\cos\phi\hat{y}' + \sin\phi\hat{x}'). \tag{2.14}$$

After the second $\pi/2$ pulse, only the component at $-\hat{y}'$-axis of the magnetic moment can be rotated from x'-y' plane to $-\hat{z}'$-axis. The projection of the magnetic moment along the $-\hat{z}'$-axis will be $-\mu\cos\phi$. At the end of the second $\pi/2$ pulse, a spin analyzer for the $\hat{z}$-component of the magnetic moment is applied. Thus we can determine the precession frequency relative to the oscillatory fields by measuring the final polarization of the neutrons.

For a real measurement, a polarized neutron beam with a velocity $\vec{v}$ passes through two oscillatory fields, generated by RF coils separated by a distance L. The frequency of the two oscillatory fields is varied. Only when the frequency matches the Larmor frequency of the neutron, the flip of the magnetic moment of neutron is π or 180°, i.e., two $\pi/2$ pulses. Once the frequency is off the resonance frequency, the projection of the magnetic moment along the $\hat{z}$-axis is proportional to $\cos\phi$ as described before. Fig. 2.3 shows an example of an actual measurement. The oscillations are called fringes in analogy to an interferometer. The phase difference between two fringe peaks is $\Delta\phi = 2\pi$. The frequency difference would correspond to $\Delta\omega \cdot T = 2\pi$ and T is the time period for neutrons passing between two oscillatory fields, given by $T = L/v$. It shows that better frequency determination can be obtained,

$$\Delta f_{RF} = \frac{\Delta\omega}{2\pi} = \frac{1}{T} = \frac{v}{L}, \tag{2.15}$$

if the neutron is slower. When $\Delta B > B_1$ where $\Delta B = B_0 - \frac{\omega}{\gamma}$, the $\pi/2$ pulse is no longer effective. The initial spin-flip probability will be reduced and then the oscillation fades. More details would require quantum mechanics calculation of the transition probability [66][69][70].
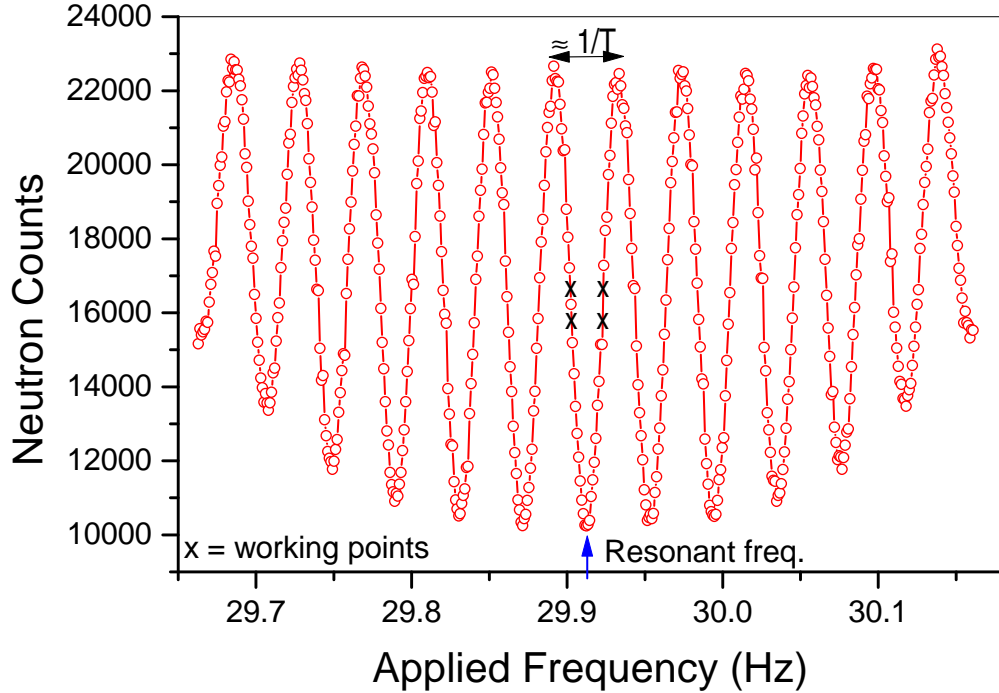
Figure 2.3: The number of neutrons remaining with their spins unflipped after application of Ramsey separated oscillatory fields, as a function of the frequency [33].

Following the inaugural work done by Smith, Purcell and Ramsey [84], several experiments had been done by using the separated oscillatory fields for decades [62]. The upper limits were pushed by researchers minimizing the statistical and systematic errors. The statistical uncertainty in d_n is

$$\delta d_n \propto \frac{\bar{v}}{E_0 L P \sqrt{\phi_n T}} \tag{2.16}$$

where $\bar{v}$ is the average velocity, T is the running time, E_0 is the electric field, L is the distance between RF coils, P is the polarization of the neutrons, and ϕ_n is the neutron flux. Additionally, several systematic errors have been identified . One of dominant systematic errors is $\vec{v} \times \vec{E}$, called the motion field effect, which will cause an additional magnetic field $\vec{B}_m = \frac{1}{c} \vec{v} \times \vec{E}$ viewed in the neutron rest frame, where $\vec{v}$ is the neutron velocity in the lab frame. If $\vec{E}$ is not perfectly parallel to $\vec{B}_0$, the consequent $\vec{B}_m$ will have a nonzero component along the $\vec{B}_0$ which will mimic the EDM effect. To overcome this issue, the use of the ultra-cold neutrons(UCN) is essential.

2.2   Ultra-cold Neutrons(UCN)

Enrico Fermi first realized that neutrons with very low energy can be stored in bottles. For ultra low energy neutrons with large de Broglie wavelengths, the effective potential, called Fermi potential U_F, of many materials, is repulsive. Therefore, the neutrons can totally reflect from the material's surface.

Consequently, neutrons with very low energy can be stored in the bottle. Those very low energy neutrons are called ultra-cold neutrons (UCU). UCN have the Fermi potential $U_F \sim 200 \ neV$, velocities of order of $5 \ m/sec$, wavelengths of order $500 \ \mathring{A}$ and an effective temperature of order $2 \ mK$ [40].

There are two dominant limitations in the neutron EDM searches using thermal or cold neutron beams–the motion field effect, $\vec{v} \times \vec{E}$, and the relatively short transit time (T) of neutron beams between two RF coils. In 1968, Shapiro [80] proposed the use of UCN to search for neutron EDM. The much lower velocity of UCN will highly suppress the effect of $\vec{v} \times \vec{E}$ and increase the coherence time T of UCN in a storage bottle to the order of $10^2 - 10^3 \ sec$. The increasing of T and the suppression of $\vec{v} \times \vec{E}$ can improve the sensitivity for EDM signals a factor of $10^4 - 10^5$ related to both the statistic and systematic errors. However, the trade-off is the low flux of UCN relative to the flux of cold neutron beams. In this section, we will discuss the production of UCN and the effort of increasing the density of UCN.

The energy spectrum of the neutrons in thermal equilibrium with the moderator follows the Maxwell-Boltzmann distribution. The density distribution between velocity v and $v + dv$ can be written as

$$\rho(v)dv = \frac{2\Phi_0}{\alpha}\frac{v^2}{\alpha^2}\exp\left(-\frac{v^2}{\alpha^2}\right)\frac{dv}{\alpha}, \tag{2.17}$$

where Φ_0 is the total thermal flux of neutrons, $\alpha = (2k_B T_n/m)^{\frac{1}{2}}$ and T_n is the neutron temperature [32]. The relative fraction of UCN in the Maxwell-Boltzmann distribution is tiny. Using $E = \frac{1}{2}mv^2$, the density distribution, Eq. 2.17, is integrated up to energy $E = U_F$ and, for $v \ll \alpha$, the density of neutrons with $E \leq U_F$ is

$$\rho_{UCN} = \frac{2}{3}\frac{\Phi_0}{\alpha}\left(\frac{U_F}{k_B T_n}\right)^{\frac{3}{2}}. \tag{2.18}$$

For $T_n = 300 \ K$, $\alpha = 2.2 \times 10^5 cm \ s^{-1}$ and $U_F = 2.5 \times 10^{-7} \ eV$ for Beryllium,

$$\rho_{UCN} = 10^{-13}\Phi_0 \ cm^{-3}. \tag{2.19}$$

For reactor-based sources, the neutron flux $\Phi_0 = 10^{15} \ n/(cm^2 \ s)$ gives a maximum UCN density of $10^2 \ cm^{-3}$.

The UCN density in the momentum phase space can be increased by using various devices such as neutron turbines. However, the Liouville's theorem dictates that the neutron density is a constant within a closed system. In order to overcome this limitation, the system has to be allowed to interact with another system inelastically. In 1975, Golub and Pendlebury pointed out that higher density of UCN can be obtained by using inelastic down-scattering process in specific materials [30]. The idea is to bombard a high intensity cold neutron beam on a suitable material such that the neutron energy is almost completely exhausted via an inelastic scattering process. An ideal material is superfluid ^{4}He [31]. As shown in Fig. 2.4, the energy-momentum dispersion curves for a free neutron and for a superfluid ^{4}He cross at the

wavelength $\lambda = \frac{2\pi}{k} = 8.9 \mathring{A}$. A neutron of incident momentum $\hbar \vec{k}_i$ is inelastically scattered off superfluid ^{4}He to a momentum of $\hbar \vec{k}_f$ and excites a phonon with energy E in superfluid ^{4}He. With energy and momentum conservation,

$$\vec{Q} = \vec{k}_i - \vec{k}_f, \tag{2.20}$$

$$\frac{\hbar^2 k_i^2}{2m} = \frac{\hbar^2 k_f^2}{2m} + E(Q), \tag{2.21}$$

while $\vec{Q}$ is the momentum transfer and $E(Q)$ is the energy-momentum dispersion relation for superfluid ^{4}He (Landau-Feynman dispersion curve). At a certain beam momentum, the incident neutron can transfer practically all its momentum and energy to the phonon of the superfluid ^{4}He and emerge as an ultra-cold neutron. This occurs at $k_i = 0.7038 \ \mathring{A}^{-1}$ ($\lambda = \frac{2\pi}{k} = 8.928 \mathring{A}$), the critical momentum k_c. We use a linear dispersion relation for the superfluid ^{4}He elementary excitations, $E(Q) = \hbar \omega = \hbar c Q$, where c is the phonon sound velocity ($c \approx 2.383 \times 10^4 \ cm/sec$). If the neutron beam is limited in the region, $k_i = k_c + k_{UCN} + \delta k$ where $k_{UCN} \approx 200$ neV and $k_c = 2 \ mc/\hbar$, energy conservation shows that

$$
\begin{aligned}
\frac{\hbar}{2m} \left[k_i^2 - k_f^2 \right] &= c \left| \vec{k}_i - \vec{k}_f \right|, \\
= \frac{c}{k_c} \left[(\vec{k}_c + \vec{k}_{UCN} + \delta \vec{k})^2 - k_{UCN}^2 \right] &= c \left| \vec{k}_c + \vec{k}_{UCN} + \delta \vec{k} - \vec{k}_{UCN} \right| \\
\approx \frac{c}{k_c} \left[(k_c + \delta k)^2 \pm 2 k_{UCN}(k_c + \delta k) \right] &= c \left| \vec{k}_c + \delta \vec{k} \right| \\
\rightarrow \frac{1}{k_c} \left[k_c + \delta k \pm 2 k_{UCN} \right] &= 1 \\
\rightarrow \delta k = \pm 2 k_{UCN}. &\tag{2.22}
\end{aligned}
$$

In reality, the angle between $\vec{k}_i$ and $\vec{k}_f$ should be considered. Numerical calculation shows a very narrow region to produce UCN with energy less than $200 \ neV$ and the production is angle-dependent. At $\theta = 0°$, k_f is always equal to k_i, corresponding to an elastic scattering. For $k_i > k_c$, all scattering angles are allowed and for $k_i < k_c$, only $\theta < 90°$ is allowed. For $k_i < 0.3777 \mathring{A}^{-1}$, no inelastic scattering is allowed and the neutron beam will traverse the superfluid ^{4}He without attenuation. The group velocity $d\omega/dk$ for free neutrons is equal to $k_i = 0.3777 \mathring{A}^{-1}$ and below this momentum, phonons travel faster than neutrons. Even when the neutron beam is at the critical momentum, from the detailed calculation [12], only around 0.07% of the scattered neutrons eventually become the UCN. The rest of the neutrons would not stay in the bottle because their energy is higher than the potential of the wall.
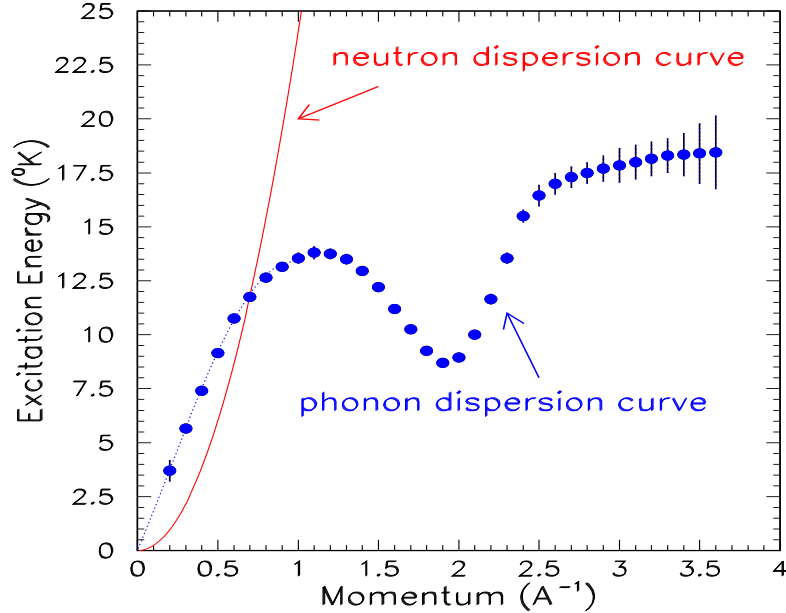
Figure 2.4: Dispersion curves for superfluid ^{4}He and for free neutron.

2.3 Comagnetometer

One important systematic error originates from the drift of the magnetic field, B_0. In Eq. 2.2, if the magnetic field B_0 has a fluctuation, the effect could cause a frequency shift mimicking the neutron EDM. One way to reduce this systematic error is to add a comagnetometer, which monitors the magnetic field fluctuations. A comagnetometer is usually a polarized atomic species, having much smaller EDM(or smaller upper limits) than the neutron. The nuclear magnetic resonance of the atoms can be measured at the same time and in the same region as the UCN. By measuring the polarization or precession frequency of the atoms, one can monitor the magnetic field experienced by the atoms and correct for neutron measurement.

Lamoreaux [43] suggested the use of ^{199}Hg as a comagnetometer and Pendlebury [61] later implemented it. First, the experimental upper limit of ^{199}Hg EDM [34] was much better than the level of the sensitivity of the neutron EDM. Besides, ^{199}Hg can be optically pumped and its polarization can be optically detected with 254 nm resonance radiation.

Subsequently, the ILL experiment [5] demonstrated the effectiveness of ^{199}Hg as a comagnetometer. In Fig. 2.5, the raw data in blue dots can be corrected to red dots by using the comagnetometer data. The electric field is around 10 kV/cm and the magnetic field is around 10 mG. Each cycle yielded about 14000 UCN counts. The density of ^{199}Hg is 3×10^{10} $atoms/cm^3$ and $\gamma_n/\gamma_{Hg} = -3.842$. By comparing the precession frequencies of neutron and ^{199}Hg, the ILL group published the result of the room-temperature EDM experiment in 2006 and pushed the upper limit to $|d_n| < 2.9 \times 10^{-26}$ e cm [5].

The use of ^{3}He as a comagnetometer was first mentioned by Ramsey in 1984 [71]. However, the
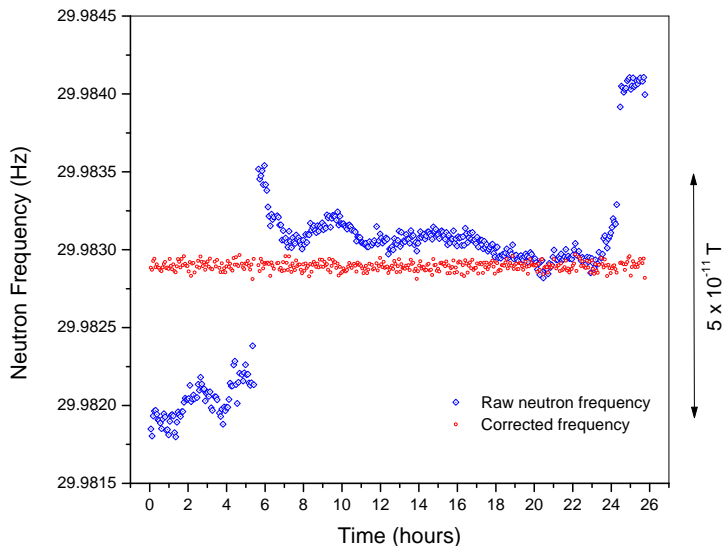
14

Figure 2.5: Neutron resonant frequency, measured over a 26 hour period, before and after magnetic field drift corrections [33]. The frequency shift is about 10^{-3} Hz while the magnetic field drift is around 5×10^{-4} mG. After the correction, the frequency shift can be reduced to 10^{-4} Hz.

difficulty measuring the polarization of ^{3}He prevented its implementation. Nevertheless, ^{3}He was proposed by Golub and Lamoreaux [29] as a comagnetometer for the new neutron EDM experiment at SNS [12]. The precession of ^{3}He atoms can be determined directly by using SQUID magnetometers sensitive to the changing magnetic field caused by the rotating magnetization of the ^{3}He. Another advantage of this method is that it can overcome the technical difficulty in the extraction of UCN from the bath. A dilute admixture of polarized ^{3}He atoms in the superfluid ^{4}He bath will be applied. The fractional density of ^{3}He $x = N(^3He)/N(^4He) \approx 10^{-10}$ will be used in the future neutron EDM experiment at the SNS. The following sections will focus on the experiment at SNS.

2.4 Measurement of the neutron precession frequency at SNS

Some interesting characteristics of ^{3}He atoms allow them to be used to analyze neutron precession frequency. First, UCN can be detected through the following reaction

$$n + {}^3He \rightarrow p + {}^3H + 764 KeV. \tag{2.23}$$

The charged particles, proton and triton, produced in this reaction will interact with liquid helium to produce scintillation light ($\sim 80nm$) [57]. If the measurement cells are coated with a wavelength shifter, deuterated tetraphenyl butadinene (dTPB), the scintillation light is converted to blue light which can be detected by photomultiplier tubes (PMT).

15

A crucial feature of the n+^{3}He absorption is that the reaction only occurs when the total spin of neutron and ^{3}He is equal to 0 ($J = 0$). At UCN energy, the absorption cross section can be written as

$$\sigma = \sigma_0 \frac{1 - \cos\theta_{n3}}{2}, \tag{2.24}$$

where $\sigma_0 = 11.0 \; barns$ and θ_{n3} is the angle between neutron spin and the ^{3}He spin. Consequently, the observed rate of scintillation depends on the relative angle between the neutron and ^{3}He spins and is proportional to

$$1 - P_3 P_n \cos[(\gamma_3 - \gamma_n)B_0 t]. \tag{2.25}$$

where P_3 and P_n are the polarizations of the ^{3}He and the neutrons respectively, and γ_3 and γ_n are the gyromagnetic ratios of the ^{3}He and the neutrons respectively. Together with the information of the ^{3}He precession, the precession of neutron can be exquisitely measured.

Instead of using "SQUID" to monitor the precession of ^{3}He, an alternative method, called "the dressed spin technique", was also proposed to search for the neutron EDM by Golub and Lamoreaux [29]. The main reason to use the technique is to reduce the systematic error from the magnetic field B_0. The scintillation light depends on the angle between neutron and ^{3}He, i.e., $\theta_{n3} = (\gamma_3 - \gamma_n)B_0 t$, where B_0 can have a significant drift. If $\gamma_3 - \gamma_n$ can be minimized, the error from B_0 drift will also be minimized. To reach this goal, a RF field, called "dressing field," can be applied to modify the magnetic moment of a particle. The particle is then "dressed," yielding an effective gyromagnetic ratio given by

$$\gamma' = \gamma J_0\left(\frac{\gamma B_d}{\omega_d}\right) \tag{2.26}$$

where B_d and ω_d are the amplitude and the frequency of the RF field, and J_0 is the zeroth order Bessel function. Neutron and ^{3}He can be made to precess at the same precession frequency by applying a proper dressing field so that

$$\gamma_n J_0\left(\frac{\gamma_n B_d}{\omega_d}\right) = \gamma_3 J_0\left(\frac{\gamma_3 B_d}{\omega_d}\right). \tag{2.27}$$

This situation is called "critical dressing." How to apply this property when searching for the neutron EDM will be the subject of this thesis. More details will be discussed in later chapters.

2.5 Measurement cycle at SNS

Following Fig. 2.6 [38], the proposed measurement cycle at SNS will now be summarized. The duration of each step remains to be optimized to reach the maximal sensitivity.

The conceptual design of the proposed apparatus is shown in Fig 2.7 [38]. The apparatus is divided into two parts: the lower cryostat for the measurement and the upper cryostat for the ^{3}He injecting into the cells and removing from the cells. Both lower and upper cryostats are surrounded by four layers of μ-metal magnetic shields to shield the apparatus from the ambient magnetic field and its temporal change.

The cutaway view of the lower cryostat is shown in Fig. 2.8 [38]. Two measurement cells are placed in the gaps between the high voltage(HV, 50 kV/cm) system and ground electrodes in opposite directions. Each cell is a rectangular acrylic tube of a dimension of $7.62cm \times 10.16cm \times 50cm$. The inner walls are coated with deuterated polystyrene to minimize neutron absorption by hydrogen. The deuterated polystyrene is loaded with deuterated tetraphenyl butadinene(dTPB) which serves as the wavelength shifter for the scintillation light from the neutron absorption of ^{3}He. The converted light is guided through the light guides and detected by PMTs.

The measurement cells, the light guides, the electrodes, and the variable capacitor are all immersed in a 1200 $liter$ bath of superfluid ^{4}He. Any heat sources in the measurement cell can induce phonons generating a non-uniformity in ^{3}He concentration. The superfluid ^{4}He bath can keep the temperature across the cells uniform and eliminate potential heat sources.

The measurement cells are initially filled with isotopically pure superfluid ^{4}He at 300 mK. Polarized ^{3}He atoms are accumulated and dissolved in the ^{4}He cell at a concentration of 10^{-10} [86]. The expected density of ^{3}He will be $10^{12}/cm^3$. After the transmission, the ^{3}He polarization is kept along the B_0 magnetic field direction in the measurement cells(Polarization 99%).

Polarized 8.9 $\mathring{A}$ cold neutron beam will be injected into the superfluid ^{4}He cell to produce polarized UCN [12]. The production rate of UCN is expected to be 0.3 UCN/cc/sec. If the storage time in the cell is 500 sec, the expected density will be $150/cm^3$ and the total UCN number will be at the order of 10^6. The UCN are polarized parallel to the B_0 field(Polarization 96%). The goal for the mean life of neutrons in the cell is about 500 sec as a result of β decay, wall interactions and ^{3}He capture, etc [53].

A $\pi/2$ pulse [2] is applied to simultaneously rotate the neutron and ^{3}He spins into the plane perpendicular to the B_0 field [2]. The difference in the precession frequencies of neutron and ^{3}He atoms is measured by detecting the scintillation light (the spectrum is centered at 80 nm from the spin-dependent UCN-^{3}He capture process). Two methods can be used to overcome the drift of B_0. The precession frequency of ^{3}He can be monitored by the SQUID pickup loop. In addition, an alternative method of the dressed spin technique will be considered.

After the precession measurement, the depolarized ^{3}He atoms due to the spin relaxation are removed from the measurement cells. The electric field will be flipped periodically. Then the measurement cycle will be repeated.

The goal of the neutron EDM experiment at SNS is to search for the neutron EDM with a sensitivity two orders of magnitude better than the present limit. Various R&D studies have been pursued to

---

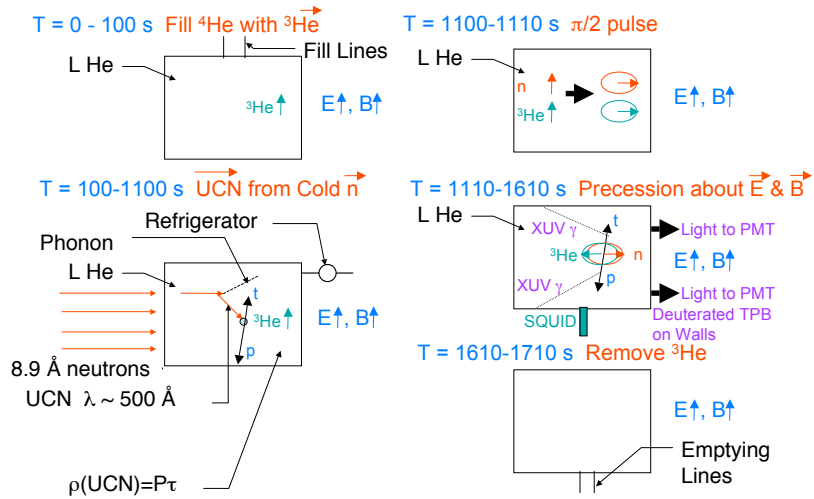[2]A detailed calculation is performed in Appendix B.

Figure 2.6: Illustrative description of a proposed measurement cycle. The duration of each step remains to be optimized to achieve maximal sensitivity. [38].
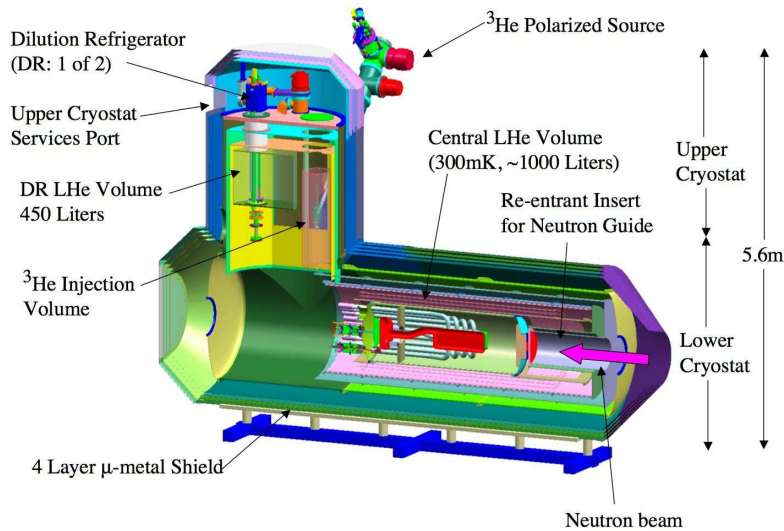

Figure 2.7: The schematic overview of the full detector apparatus [38]. The upper cryostat includes the ^{3}He system and the dilution refrigerator. The lower cryostat is the main part of the measurement, including the measurement cells, the neutron guides, the high-voltage, and the magnetic coils, etc.
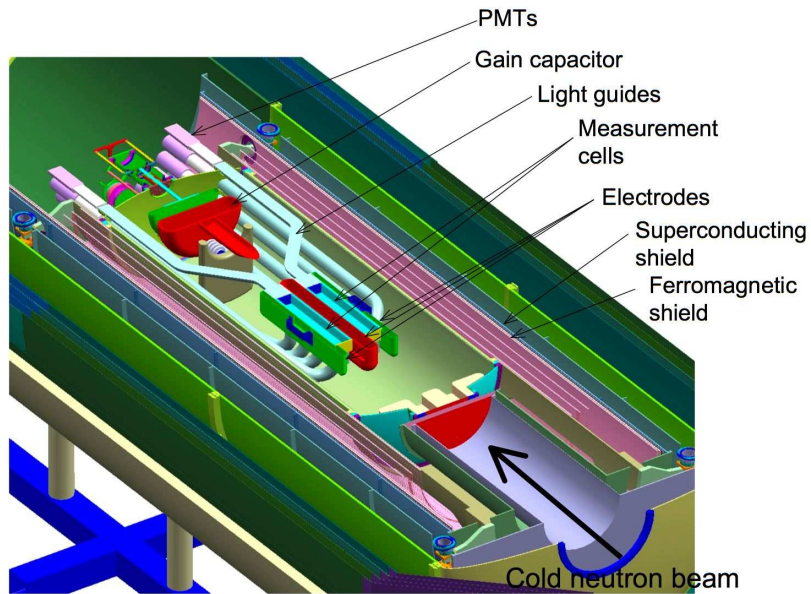
Figure 2.8: The central region of the detector illustrating the measurement cells, electrodes, light guides, HV generator and magnetic shields [38]. The SQUID magnetometers are mounted on the ground plates.

optimize the final design of the experiment. The purpose of the dressed spin technique is to reduce the systematic error of the magnetic field drift. If this method can be shown to be feasible, the neutron EDM experiment could significantly benefit from it. Therefore, careful studies of the sensitivity for the dressed spin technique are necessary and will be described in this thesis.

CHAPTER 3

MEASUREMENT OF THE DRESSED SPIN IN A ^{3}HE CELL

The dressed spin has been studied in several earlier experiments. Muskat *et al.* [51] used a polarized neutron beam and Esler *et al.* [26] used a polarized ^{3}He beam with the Ramsey separated oscillatory (SOF) field method [68][69][70]. Both measurements demonstrated that in the weak field limit, when the Larmor frequency is much smaller than the dressing field frequency, the modified effective gyromagnetic ratio becomes $\gamma' = \gamma J_0(x)$ where J_0 is the zeroth-order Bessel function of the first kind. Esler *et al.* [26] also observed the deviation from the Bessel function once the Larmor frequency was not so small comparing it with the dressing frequency.

The dressed spin technique is an important element for the neutron EDM experiment at SNS [29]. Since the EDM experiment will involve ^{3}He and neutron in a superfluid ^{4}He cell, it would be interesting to study the dressed spin phenomenon in a ^{3}He cell instead of using a ^{3}He beam, as in the experiment by Esler *et al.* [26]. An experiment has been carried out at UIUC to study dressed spin phenomenon using polarized ^{3}He in a room temperature cell. In this chapter, I will describe the experimental setup, the data-taking, the data analysis, and the results. The results will be compared with theoretical calculation presented in Chap. 4. A paper reporting the results of this study has been published [17].

3.1 Experimental method

The experimental setup is shown schematically in Fig. 3.1. A cylindrical Pyrex cell of 2.5 *cm* radius and 5.7 *cm* length, filled with ^{3}He gas of $\sim 1torr$ [48], is located in a uniform magnetic field B_0 along the $\hat{z}$-axis. The magnetic field is provided by a Helmholtz coil of 50.8 *cm* radius. Another Helmholtz coil along the $\hat{x}$-axis provides a homogeneous static magnetic field, B_q, to compensate the Earth vertical field. The parameters of both coils are shown in Tab. 3.1. Four 80-turns rectangular pickup coils of 5.08 *cm*× 6.35 *cm*

	Radius[M]	Distance[M]	Turns	R[Ω]	Amplitude[mG]
B_0	0.508	0.5207	15	1	261.5×I
B_q	0.254	0.244	6	0.8	212.4×I

Table 3.1: Geometric parameters of homogeneous static magnetic field coils. I is the input current with the unit of *Amp.*
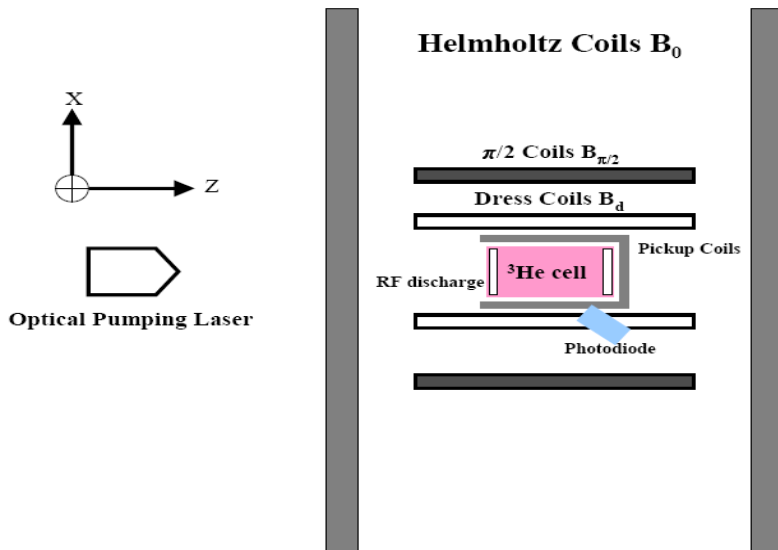
Figure 3.1: Schematic plot of the apparatus used for measuring the ^{3}He precession frequency.
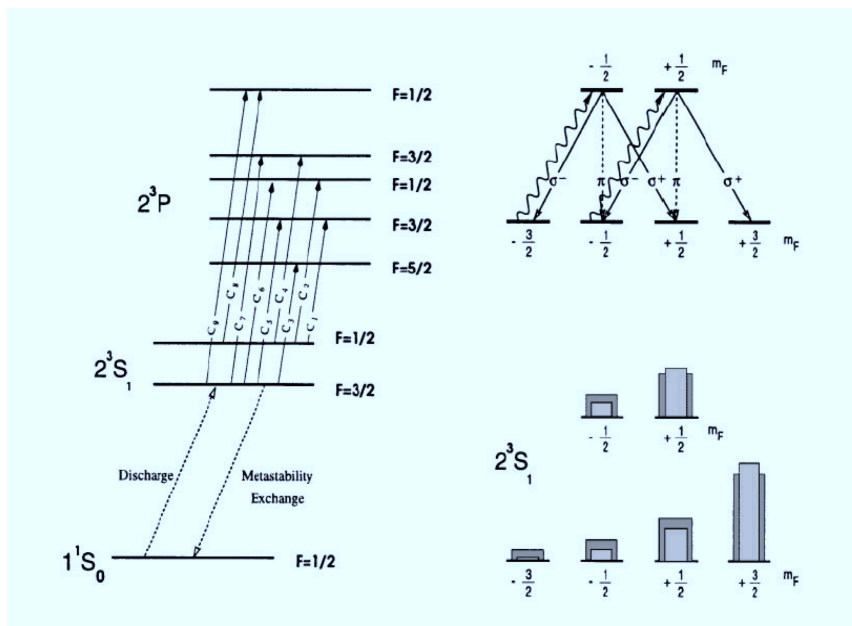
Figure 3.2: A schematics for the metastability exchange optical pumping of ^{3}He. The left diagram shows the nine optical transitions between the 2^3S and 2^3P states of ^{3}He. Top-right: The optical pumping scheme of metastable ^{3}He atoms with impinging right-handed (σ_+) circular polarized light for the C_9 transition. Bottom-right: The height of the light (dark) shaded columns indicate the distributions of the m_F levels for a nuclear polarization P=0.50 (0.33). The plots are from [64].

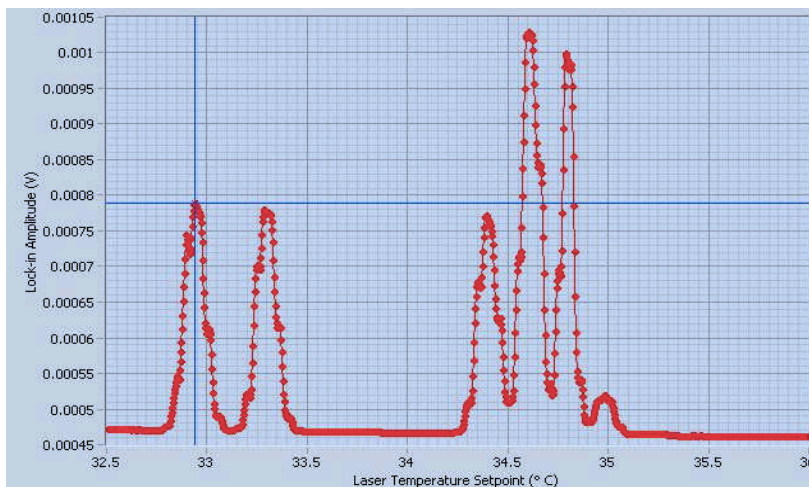Figure 3.3: The laser frequency tuning. The temperature of the laser grating is varied to tune the laser frequencies. The peaks correspond to transitions from 2^3S states to 2^3P states. The first peak from the left is the C_9 transition and the second peak is C_8, and so on.

in the $\hat{x} - \hat{z}$ plane surround the cell.

The ^{3}He gas is polarized using the optical pumping and the metastability spin exchange method [64, 22] with a circularly polarized laser light entering the cell along the holding magnetic field axis, $\hat{z}$. The GaAs semiconductor laser diode (Eagleyard photonics TO-3) delivers light at a wavelength near 1083 nm with maximum output power of 100 mW. The left plot of Fig. 3.2 shows nine transitions of ^{3}He atoms from the metastable states 2^3S_1 to excited states 2^3P. The C_9 transition, which was used for the optical pumping, can be pumped by the laser from the metastable 2^3S_1 ($F = \frac{3}{2}$) state to the 2^3P ($F = \frac{1}{2}$) state, where F is the sum of the total angular momentum of atoms and nucleus. As shown in the right-top plot of Fig. 3.2, the right-handed circularly polarized light (σ_+) can only excite the transition of $\Delta m_F = +1$ for $2^3S_1 \rightarrow 2^3P$, where m_F is the z component of F. In contrast, the de-excitation is distributed uniformly over all transitions of $2^3P \rightarrow 2^3S_1$. Therefore, repeating the process can depopulate the lower m_F levels so that the population distribution is shifted towards the higher m_F levels, as shown in the right-bottom plot of Fig. 3.2. Subsequently, through the so-called metastability exchange collisions via the process,

$$^3\overrightarrow{He}^\star +^3 He \rightarrow^3 \overrightarrow{He} +^3 He^\star \tag{3.1}$$

where the arrow means the polarized ^{3}He and the star means the excited state (metastable state) of ^{3}He, the polarization of the metastable atoms is transferred to the nuclear spin of the ground state atoms. Consequently, the nuclear spin of ^{3}He can be polarized. A polarization of 20 % of ^{3}He can be achieved in

our setup [56].

An RF electric field, applied to two electrodes on the outside surface of the cell, can generate a weak electrical discharge exciting ^{3}He atoms from the ground state to the metastable states. The frequency of RF is around 10~20 MHz. The amplitude of RF should be kept within a proper range with the output power around -20~-25 dBm, depending on temperature and other environmental situation. It cannot be so large as to destroy the pumping process, nor so small as to cease the optical pumping. Besides, the amplitude is modulated at a 40% level with a 670 Hz frequency for optical signal measurements. The RF is turned off during the NMR measurements.

An optical signal of a wavelength around 1083 nm is produced via the $2^3P \to 2^3S$ de-excitation process. The optical signal is modulated at the RF modulation frequency so that the signal can be measured using a lock-in amplifier. A photo diode is installed beside the cell to detect the modulated optical signal. The signal decreases if ^{3}He atoms are polarized along the laser polarization direction because polarized atoms can no longer interact with the circularly-polarized laser light [48]. Before doing the NMR measurements, laser tuning and Larmor frequency scan were carried out using the optical signals. Fig. 3.3 shows that various transitions can be observed depending on the laser frequency, which can be tuned by varying the temperature of the laser [64]. The first peak from left is the C_9 transition and the second is the C_8 transition. The rest are $C_7 - C_1$ transitions which have very similar energies. The scanning range of temperature for transitions of $2^3S_1 \to 2^3P$ is around $25 - 36°C$ and the C_9 transition is located at $\sim 29 - 31°C$.

A pair of coils for an oscillatory magnetic field, $B_1 \cos(\omega t)\hat{x}$, is placed near the ^{3}He cell and along $\hat{x}$-axis. At the nuclear Larmor frequency $\omega = \omega_0 = \gamma B_0$, the macroscopic nuclear magnetization precessing about the oscillatory magnetic field becomes alternatively parallel and antiparallel to the light beam, $\hat{z}$-axis. Therefore the oscillatory magnetic field modulates the relative metastable level populations and the optical signal intensity at the frequency γB_1. The optical signal amplitude will be maximal when the frequency, ω, is at the Larmor frequency since more ^{3}He atoms can be optically pumped. Therefore, by varying the frequency, ω, the Larmor frequency can be determined. The oscillatory optical signal can also be used to calibrate B_1. The calibration of B_1 will be discussed in Sec. 3.4.

Once the Larmor frequency is determined, a nuclear magnetic resonance (NMR) measurement can be performed. If $B_1 \cos(\omega_0 t)\hat{x}$ is applied for a duration τ, the magnetization vector rotates by an angle $\gamma \frac{B_1}{2}\tau$. Therefore, by applying a $\frac{\pi}{2}$ pulse for $\tau = \frac{\pi}{\gamma B_1}$[1], the polarization of ^{3}He atoms can be rotated from $\hat{z}$-axis to $\hat{x} - \hat{y}$ plane. ^{3}He atoms then precess at the Larmor frequency $\omega_0 = \gamma B_0$ in the $\hat{x} - \hat{y}$ plane. The precessing magnetization induces a current in the pickup coils, and the ^{3}He precession frequency can be determined by analyzing signals of the pickup coils via a lock-in amplifier. The output signal from the lock-in amplifier decays exponentially with a time constant T_2, the transverse relaxation time, as shown in Fig. 3.4.a [2]. The

---

[1] The number of cycles is $n = \tau \cdot \frac{\omega_0}{2\pi} = \frac{\omega_0}{2\gamma B_1} = \frac{B_0}{2B_1}$.

[2] The data of T_2 are listed in Appendix C. The magnitude of NMR signals is estimated in Appendix D.
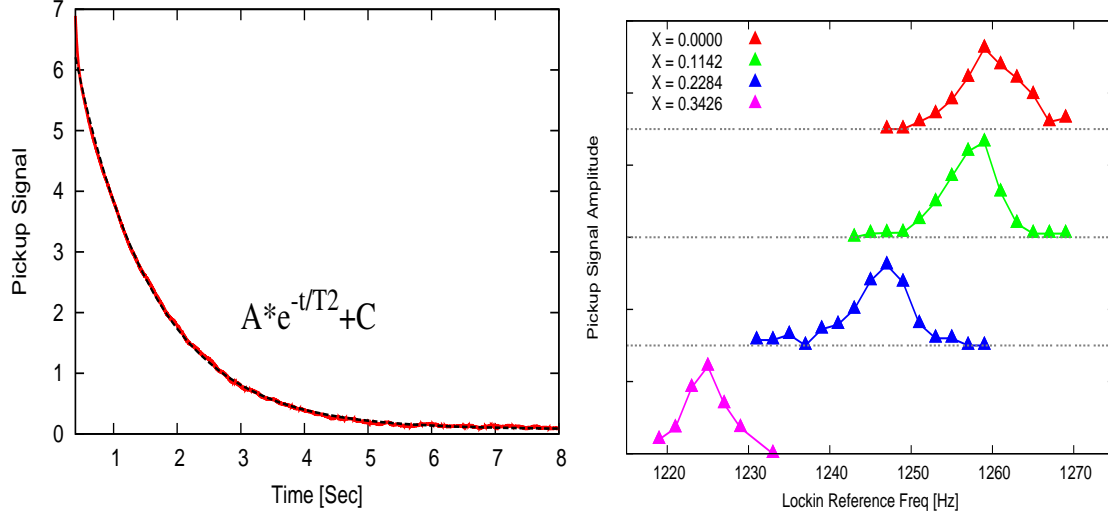
Figure 3.4: (a) Output of the lock-in amplifier averaging over 5 measurements. The dash line is the fitted curve. The parameter "A" corresponds to the amplitude of the signal which decays exponentially with time. (b) Pickup coils signal amplitude (A) vs. reference frequency. The resonance frequency shifts with the magnitude of the dressing field B_d ($x = \gamma B_d/\omega_d$). For these data $B_0 = 387.7 mG$, $\omega_0/2\pi = 1257 Hz$, and $\omega_d/2\pi = 7152.5 Hz$ ($y = 0.176$).

lock-in reference frequency is varied until maximal signal amplitude is found. This occurs when the reference frequency of the lock-in amplifier is the same as the ^{3}He precession frequency. The widths of the signal peaks in Fig. 3.4.b are mainly due to the bandwidth of the lock-in amplifier [3]. Another pair of coils providing a dressing field, $B_d \cos(\omega_d t)\hat{x}$, is placed near the ^{3}He cell and along the $\hat{x}$-axis. When the dressing field is applied, the ^{3}He precession frequency shifts to a different value, as demonstrated in Fig. 3.4.b. From these measurements, the effect of the dressing field can be detected.

We now will summarize the NMR measurement procedure. The holding field B_0 is always on. The optical pumping and metastability exchange are run for about 30-40 seconds to polarize the nuclear spin of ^{3}He atoms. After ^{3}He atoms are polarized, the RF is turned off. Then the $\frac{\pi}{2}$ pulse is applied to rotate the ^{3}He polarization from $\hat{z}$-axis to $\hat{x} - \hat{y}$ plane. The duration of B_1 depends on the amplitude and the Larmor frequency. After the $\frac{\pi}{2}$ pulse, ^{3}He atoms precess freely for 1 second until the RF quiets down. Subsequently, the dressing field $B_d \cos \omega_d t \hat{x}$ and the data-taking are both turned on. Data-taking takes 10 seconds due to the limitation of the relaxation time, T_2. The data from the pickup signal are stored in a computer through the PC DAQ board and await further analysis. Then the next measurement cycle is ready to start. The signals of the pickup coils are averaged several times(around 10 times) in order to reduce the noise.
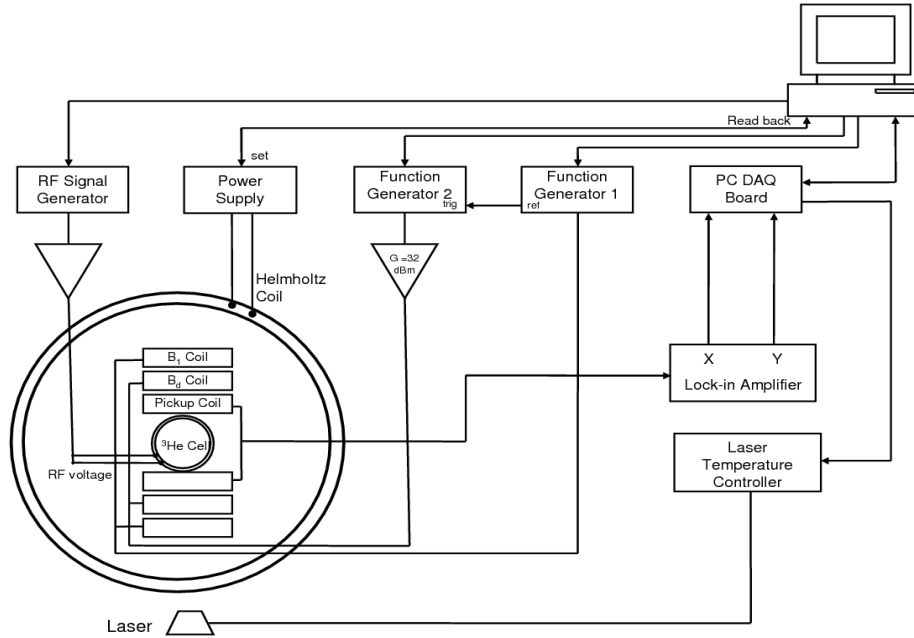
24

Figure 3.5: Block diagram of the NMR electronics.

3.2 Electronics

We briefly will describe the electronics we used. The laser temperature is controlled by Laser Diode Temperature Controller ITC 502. The holding field is provided by the Agilent N6702A Low Profile Modular Power System Mainframe, 1200W. The Earth compensating field is provided by the power supply HP - Agilent 6253A. Wavetek 2410 1100 MHz RF Signal Generator is used to generate RF signals and amplified by the Amplifier Research 50A220. Both B_1 and B_d are controlled by the Agilent 33220A Function/Arbitrary Waveform Generators and B_d is amplified using the PV 900 Watt Stereo power amplifier. The lock-in amplifier is the Stanford Research System SR830 Lock-in Amplifier. The electronics diagram is shown in Fig. 3.5.

3.3 Data

Measurements are performed at different B_0, and the dressing field frequencies ω_d and magnitudes B_d as shown in Tab. 3.2. At each dressing field frequency, the magnitude of the dressing field is varied over a broad range. Two dimensionless parameters which characterize various dressing field configuration are
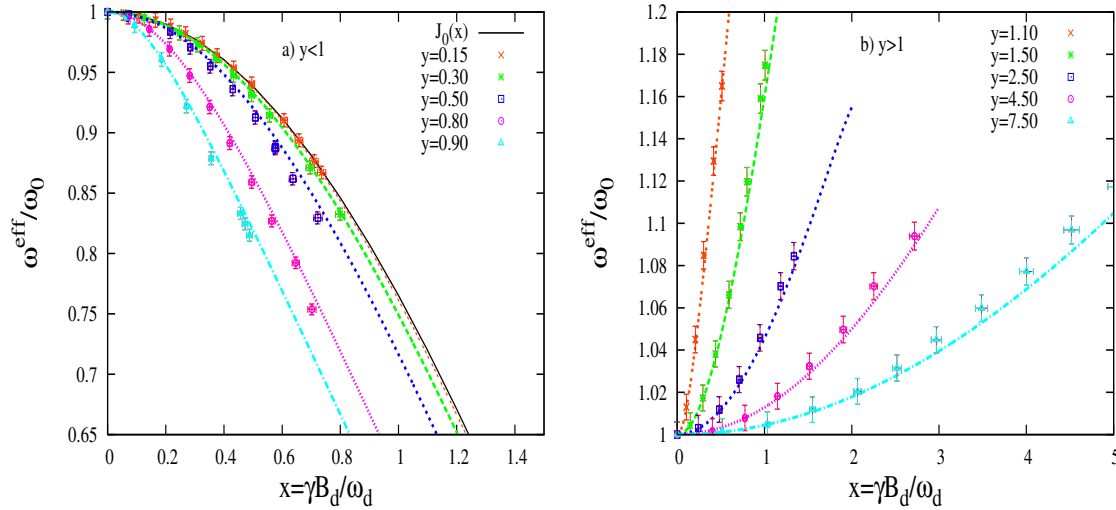
---

[3]See Appendix E.

25

Figure 3.6: Effective precession frequency ratio vs. x for (a) $y < 1$ (b) $y > 1$. The dashed curves are numerical calculations described in Sec. 4.6

y	$\frac{\omega_0}{2\pi}$ [Hz]	$\frac{\omega_d}{2\pi}$ [Hz]		y	$\frac{\omega_0}{2\pi}$ [Hz]	$\frac{\omega_d}{2\pi}$ [Hz]
0.15	1271	8473		1.1	1267	1151.8
0.3	1272	4240		1.5	1267	844.7
0.5	1267	2540		2.5	1267	506.8
0.8	1271	1588		4.5	1267	281.5
0.9	1271	1412		7.5	1270	169.33

Table 3.2: List of ω_0, ω_d, and $y = \omega_0/\omega_d$ for all sets of measurement. B_d and $x = \gamma B_d/\omega_d$ are varied over a broad range for each set.

defined as

$$x = \frac{\gamma B_d}{\omega_d} \tag{3.2}$$

and

$$y = \frac{\gamma B_0}{\omega_d}. \tag{3.3}$$

The results of our measurements are shown in Fig. 3.6 as functions of x and y. When y is close to 0, the effective precession frequency follows the Bessel function of x; however, as y increases, the deviation from Bessel function is clearly observed. When the dressing field frequencies are higher than the Larmor frequency, i.e., $y < 1$, the effective precession frequencies (ω^{eff}) are smaller than the Larmor frequency (ω_0) as shown in Fig. 3.6.a. The reverse is true for $y > 1$, where ω^{eff} becomes larger than ω_0, as shown in Fig. 3.6.b. All dashed lines are numerical calculations to be described in the next chapter.
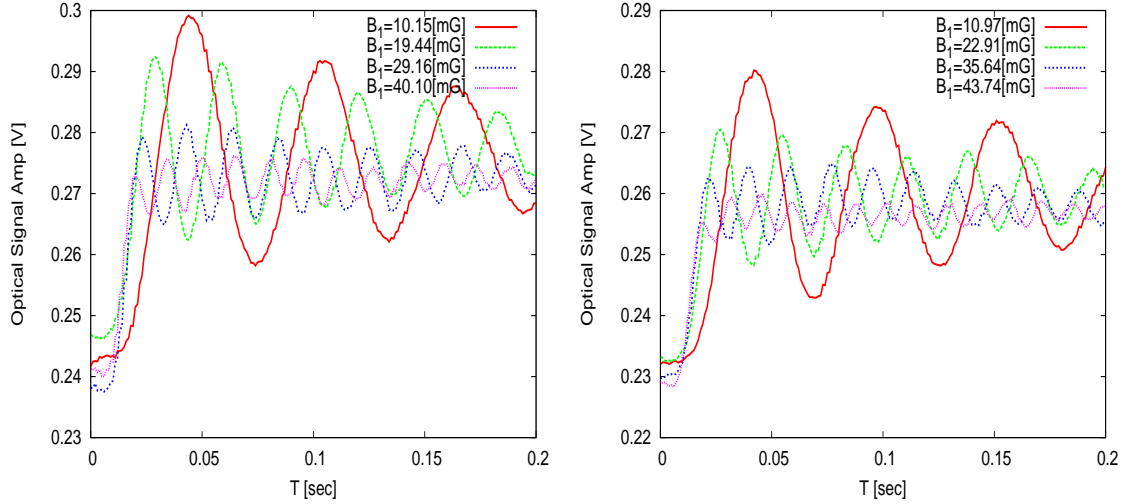
Figure 3.7: Optical signal while applying $B_1(t)$. top) $\omega_0/2\pi = 7153$ Hz. bottom) $\omega_0/2\pi = 2950$ Hz.

3.4 Calibration

The optical signal can be used to calibrate oscillatory magnetic fields. The optical signal maximizes when an RF pulse is applied to orient the magnetization of ^{3}He antiparallel to the B_0 axis, making the optical pumping maximally efficient. Several oscillatory optical signals in different setups are shown in Fig. 3.7. The amplitude of the oscillation damps as ^{3}He depolarizes. The separation in time between adjacent peaks is equal to

$$\Delta t = \frac{2\pi}{\gamma B_1/2} = \frac{4\pi}{\gamma B_1} \tag{3.4}$$

By measuring Δt in Fig. 3.7 and listed in Tab. 3.3, the magnetic field can be obtained via the equation

$$B_1 = \frac{4\pi}{\gamma \Delta t}. \tag{3.5}$$

The relations between B_1 and the function generator voltage V_{pp} are obtained as $B_1 = (19.809 \pm 0.1162) \times V_{pp}$ mG for $\omega_0/2\pi = 7153$ Hz and $B_1 = (21.898 \pm 0.1943) \times V_{pp}$ mG for $\omega_0/2\pi = 2950\ Hz$, as shown in Fig. 3.8. The calibration of B_1 does not impact on the dressed spin measurement. It determines the exact angular solution for the $\frac{\pi}{2}$ pulse and affects the amplitude of NMR signal, but does not affect the frequency shift due to the dressing field.

Using similar method, we can calibrate the dressing coils B_d. To reach larger values of B_d, an amplifier is added between the function generator and the dressing coils. However, the response of the amplifier is not as linear as the function generator. We measure the relation between the optical signal, which is related to B_d, and the corresponding current through a 5Ω resistor connected to the dressing coils. In the range shown in Fig. 3.10 and Tab. 3.4, the relation between V_{pp} and the current I is still linear so that we can get $B_d = (837.167 \pm 9.244) \times I$ mG. During the NMR measurement, we also measure the current
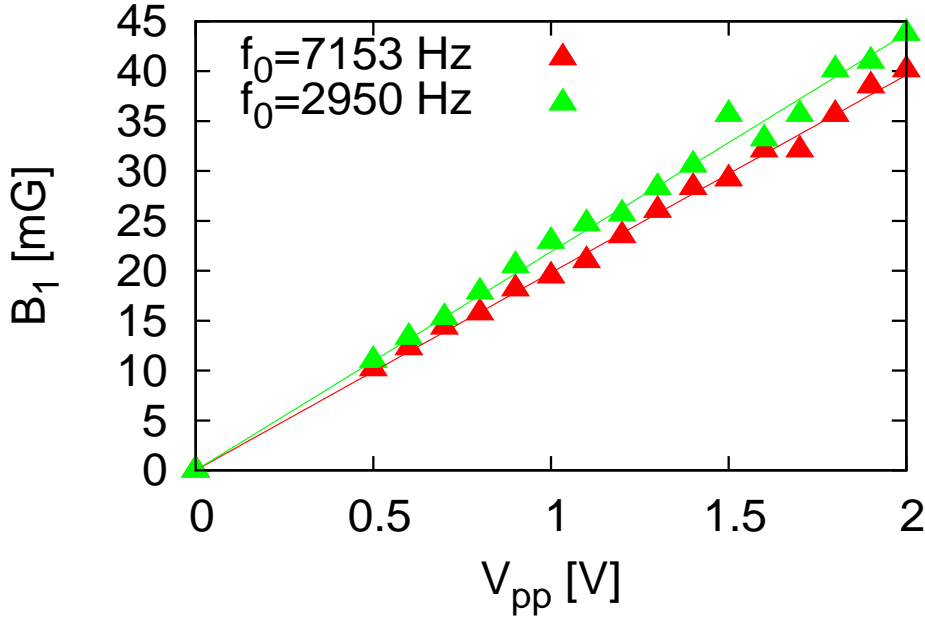
Figure 3.8: B_1 vs. V_{pp}. For $\omega_0/2\pi = 7153$ Hz, $B_1 = (19.809 \pm 0.1162) \times V_{pp}$ mG. For $\omega_0/2\pi = 2950$ Hz, $B_1 = (21.898 \pm 0.1943) \times V_{pp}$ mG.

	$f_0 = 7153$[Hz]		$f_0 = 2950$[Hz]	
V_{pp}[V]	Δt [sec]	B_1	Δt [sec]	B_1
0.5	0.0607842	10.14911381	0.056209	10.97514
0.6	0.0503265	12.25807007	0.046405	13.293989
0.7	0.0431371	14.3010486	0.040385	15.27577
0.8	0.0392157	15.73109146	0.034615	17.82171
0.9	0.0339869	18.15128074	0.03013	20.4748
1	0.0317308	19.44185975	0.026923	22.91371
1.1	0.0294117	20.9748421	0.025	24.67623
1.2	0.026282	23.47255777	0.024039	25.66324
1.3	0.0237179	26.01013426	0.021795	28.30518
1.4	0.0217949	28.30505134	0.020192	30.55154
1.5	0.0211539	29.16274367	0.017308	35.64363
1.6	0.0192307	32.07921518	0.01859	33.18535
1.7	0.0192307	32.07921518	0.017308	35.64343
1.8	0.0173076	35.64363421	0.015385	40.09865
1.9	0.0160256	38.49501818	0.015064	40.95205
2	0.0153846	40.09891472	0.014103	43.74412

Table 3.3: The calibration data of B_1. V_{pp} is the voltage of function generator output. For $f_0 = 7153$ Hz, fitting V_{pp} and B_1 gives the relation $B_1 = (19.809 \pm 0.1162) \times V_{pp}$ [mG]. For $f_0 = 2950$ Hz, fitting V_{pp} and B_1 gives the relation $B_1 = (21.898 \pm 0.1943) \times V_{pp}$ [mG]

V_{pp}[V]	I[A]	Δt [sec]	B_d[mG]
0.01	0.016	0.048739998	12.65707405
0.02	0.0312	0.025079999	24.59751953
0.03	0.0464	0.01668	36.984759
0.04	0.0608	0.012579999	49.03861643
0.05	0.076	0.01014	60.83883306
0.06	0.0912	0.008300002	74.32597849
0.07	0.1056	0.006979999	88.38192955
0.08	0.1216	0.006037998	102.1705753
0.09	0.1304	0.005417999	113.8622967

Table 3.4: The calibration data of B_d using optical signal. For $f_0 = 1257$ Hz, $B_d = (837.167 \pm 9.244) \times I$ mG. The amplifier is set at 32 dBm.

V_{pp}[V]	I[A]	n	B_d[mG]
0.05	0.076	70	63.03464
0.1	0.1504	34	129.7772

Table 3.5: The calibration data of B_d using NMR signal at $f_0 = 7152.51$ Hz. The amplifier is set at 32 dBm.

through the resistor to get the value of B_d, which is the dominant uncertainty of our measurement.

We can also use NMR signal for calibration. The dressing coil is used as a $\frac{\pi}{2}$ coil to rotate magnetization of ^{3}He. Using different pulse duration τ for B_d, the NMR signal amplitude (A) will be different so that we can fit A vs. τ to obtain the oscillation period. The period T_d is related to the B_d as

$$B_d = \frac{4\pi}{\gamma T_d} \qquad (3.6)$$

Combining results from the above two methods, we obtain $B_d = (842.969 \pm 7.782) \times I$ mG.

3.5 Systematic uncertainties

Many possible sources should be considered as systematic uncertainties. The left plot of Fig. 3.4 shows a 2 Hz measurement step. It gives $\sim 1\ Hz$ error for measuring the effective precession frequency, which is around 1000 Hz. It will contribute a 0.1% error. The drift of B_0 will contribute 0.5% error due to the power supply current stability limitation which has noise of $\sim 4.5\ mV$ compared with the operating voltage $1\ V$. The drift of B_d amplitude and frequency due to a function generator can be ignored here. The error of B_d due to the calibration is set at 1% by fitting the calibration data in Fig. 3.10. The total error is about 2%. Adding 2% error for x and 0.5% for the ratios, the results are shown in Fig. 3.6.
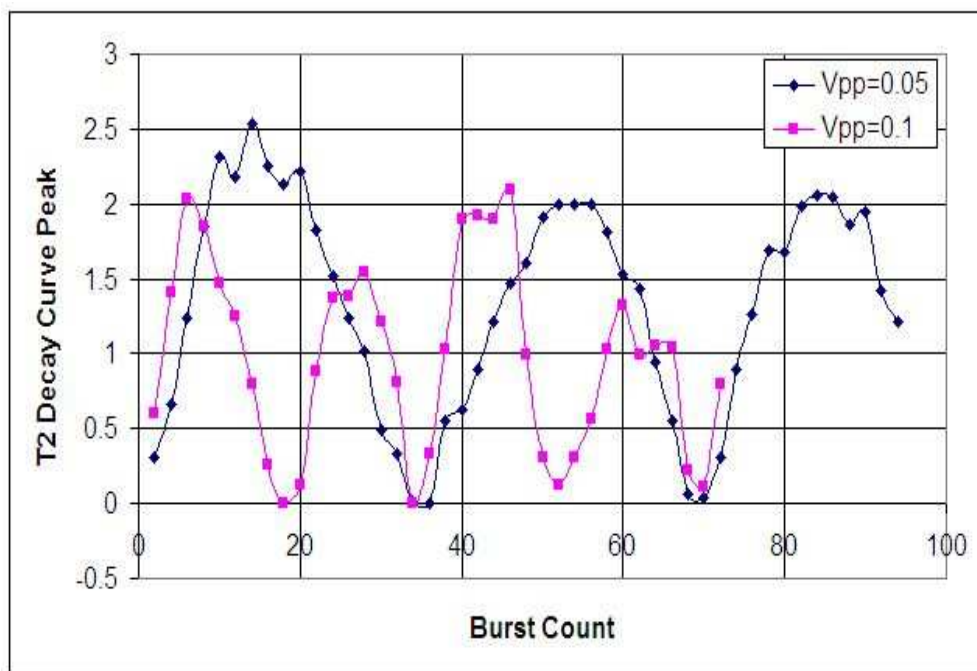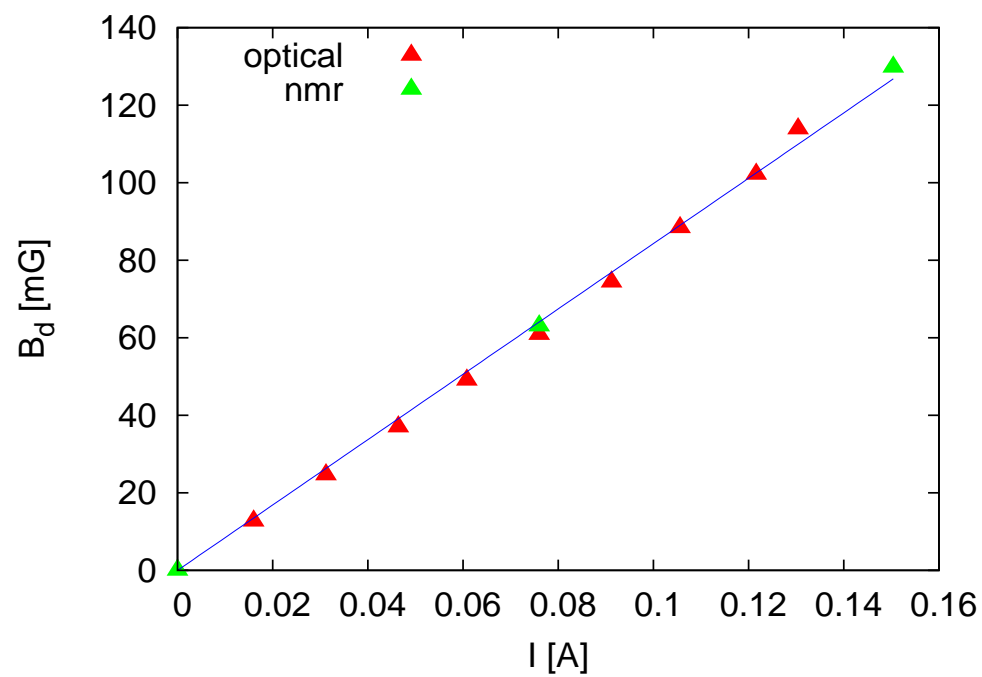
Figure 3.9: A vs. n

Figure 3.10: B_d vs. I. $B_d = (842.969 \pm 7.782) \times I$ mG

	Systematic uncertainty(%)
f_{eff}	0.1%
B_0 drift	0.5%
B_d calibration	1%
total	1.12%

Table 3.6: Systematic uncertainties.

CHAPTER 4

THEORY OF THE DRESSED SPIN

The dressed spin system was first studied by Cohen-Tannoudji *et al.* [19][20][21][35][63]. If a particle with a spin $S = \frac{1}{2}$ is placed in a uniform field B_0 and an RF field B_d that is perpendicular to B_0, the precession frequency will be modified by the RF field, i.e., the "dressing field". A spin with the modified precession frequency is called "the dressed spin". The spin is "dressed" since its precession frequency is modified. In this chapter, first we use a classical picture to explain the dressed spin – a larger or a smaller modified precession frequency. Then a quantum mechanical approach will be presented [19][20][21][63], in which the Hamiltonian can be written in terms of creation and annihilation operators of photon and other terms [81][88]. The eigenvalues can be calculated numerically for given B_0 and B_d. The modified precession frequency will then be obtained from the set of eigenvalues and compared with the experimental data.

4.1   Classical treatment

If a particle has a spin $\vec{S}$, its magnetic dipole moment $\vec{\mu}$ is proportional to $\vec{S}$,

$$\vec{\mu} = \gamma \vec{S}, \tag{4.1}$$

where the proportionality constant γ is called the gyromagnetic ratio. When this particle is placed in a magnetic field $\vec{B}$, it experiences a torque, $\vec{\mu} \times \vec{B}$. Therefore, the motion of a spin can be treated classically [83] as

$$\frac{d\vec{S}}{dt} = \vec{S} \times (\gamma \vec{B}(t)). \tag{4.2}$$

If the particle is in a uniform magnetic field $B_0 \hat{z}$, the transverse component of the spin precesses about B_0 at the Larmor frequency $\omega_0 = \gamma B_0$. Adding an RF field,

$$B_d \cos{(\omega_d t)} \hat{x}, \tag{4.3}$$

the precession frequency of the spin will be modified, which is called the "dressed spin". The RF field can be seen as a linear combination of a right-handed and a left-handed rotating fields,

$$B_d \cos{(\omega_d t)}\hat{x} = \frac{1}{2}[B_d(\cos \omega_d t\hat{x} + \sin \omega_d t\hat{y}) + B_d(\cos \omega_d t\hat{x} - \sin \omega_d t\hat{y})]. \tag{4.4}$$

In the frame rotating along $\hat{z}$ at the frequency ω_d, the RF field becomes

$$\frac{1}{2}[B_d + B_d(\cos 2\omega_d t\hat{x}' - \sin 2\omega_d t\hat{y}')]. \tag{4.5}$$

By using the rotating wave approximation, the second term can be ignored due to its high frequency. The total magnetic field becomes a static field $(B_0 - \frac{\omega_d}{\gamma})\hat{z} + \frac{B_d}{2}\hat{x}'$ in the rotating frame. Two parameters are defined as $x = \gamma B_d/\omega_d$ and $y = \gamma B_0/\omega_d$. The spin in this rotating frame precesses at a frequency

$$\gamma\sqrt{(B_0 - \frac{\omega_d}{\gamma})^2 + (\frac{B_d}{2})^2} = \omega_d\sqrt{(y-1)^2 + (\frac{x}{2})^2}. \tag{4.6}$$

Going back to the lab frame, if $(x/2)/(y-1) \ll 1$, the precession frequency becomes

$$\omega^{eff} \approx \omega_d + \omega_d\sqrt{(y-1)^2 + (\frac{x}{2})^2} \approx \omega_d + \omega_d[(y-1) + \frac{x^2}{8(y-1)}] = \omega_0 + \gamma B_d\frac{x}{8(y-1)}. \tag{4.7}$$

Eq. 4.7 shows that when $y > 1$ ($y < 1$), the effective ω^{eff} is bigger (smaller) than ω_0.

Numerical calculation using Eq. B.1 for different dressing field conditions have been carried out. The calculation will help us to visualize the behavior of spin in response to the dressing field. The corresponding Monte Carlo study will be described in Chap. 5.

4.2   Quantum mechanical approach

An RF field, $B_d(t)$, will be applied to the system of a uniform holding field $\vec{B}_0$. The quantized vector potential [21, 75] of the RF field can be written as

$$\vec{A} = \sum_{k,\xi} \frac{\alpha}{\sqrt{k}}[a_{\vec{k},\xi}\vec{\epsilon}_\xi e^{i\vec{k}\cdot\vec{r}} + a^\dagger_{\vec{k},\xi}\vec{\epsilon}^*_\xi e^{-i\vec{k}\cdot\vec{r}}], \tag{4.8}$$

where $\vec{\epsilon}_\xi$, the photon polarization vector, is a unit vector whose direction depends on the propagation direction $\vec{k}$ and $\xi = 1, 2$ is the polarization index parameter. For a given $\vec{k}$, $\vec{\epsilon}_1$ and $\vec{\epsilon}_2$ can be chosen so that $(\vec{\epsilon}_1, \vec{\epsilon}_2, \vec{k}/|\vec{k}|)$ form a right-handed set of orthonormal unit vectors. $a_{\vec{k},\xi}$ and $a^\dagger_{\vec{k},\xi}$ are annihilation and

creation operators. α is a constant proportional to the strength of the RF field. Thus the magnetic field is

$$\vec{B}_d = \nabla \times \vec{A} = -i \sum_k \sum_\xi \frac{\alpha}{\sqrt{k}} [a_{\vec{k},\xi} \vec{\epsilon}_\xi \times \vec{k} e^{i\vec{k}\cdot\vec{r}} - a_{\vec{k},\xi}^\dagger \vec{\epsilon}_\xi^* \times \vec{k} e^{-i\vec{k}\cdot\vec{r}}]. \qquad (4.9)$$

If only a single mode of the field is present (only one $\vec{k}$), the polarization $\vec{\epsilon}_\xi \times \vec{k}$ is equal to $\vec{\epsilon}$ and the module is the wave vector $|\vec{k}| = \frac{\omega_d}{c}$. Summing over ξ, the magnetic field can be simplified to

$$\vec{B}_d = \frac{\alpha}{\sqrt{k}} [a \vec{\epsilon} e^{i\vec{k}\cdot\vec{\rho}} + a^\dagger \vec{\epsilon}^* e^{-i\vec{k}\cdot\vec{\rho}}], \qquad (4.10)$$

(To eliminate the imaginary i, set $\vec{r} = \vec{r}_0 + \vec{\rho}$ and $kr_0 = \frac{\pi}{2}$.) Since atomic dimensions are much smaller than the wavelength of the RF field, we can set $e^{i\vec{k}\cdot\vec{\rho}} = 1$ and the magnetic field can be written as

$$\vec{B}_d = \frac{\alpha}{\sqrt{k}} [a \vec{\epsilon} + a^\dagger \vec{\epsilon}^*]. \qquad (4.11)$$

Coupling the magnetic dipole moment $\vec{\mu} = \gamma \hbar \vec{S}$ to the magnetic field $\vec{B}$, the classical interaction potential is $V_{cl} = -\vec{\mu} \cdot \vec{B} = -\gamma \hbar \vec{S} \cdot \vec{B}_d(t)$, which can be quantized as

$$V = \lambda \hbar \vec{S} \cdot [a \vec{\epsilon} + a^\dagger \vec{\epsilon}^*], \qquad (4.12)$$

where $\lambda = -\frac{\gamma \alpha}{\sqrt{k}}$. For the polarization of $\vec{\epsilon} = \hat{x}$, the potential can be written as

$$V_{\sigma_x} = \lambda \hbar \hat{S}_x [a + a^\dagger] = \frac{\lambda \hbar}{2} [a \hat{S}_+ + a^\dagger \hat{S}_-] + \frac{\lambda \hbar}{2} [a \hat{S}_- + a^\dagger \hat{S}_+] \equiv \frac{1}{\sqrt{2}} [V_{\sigma+} + V_{\sigma-}]. \qquad (4.13)$$

V is the sum of two terms, corresponding to right-hand and left-hand circular by polarized photons respectively.

4.3   Uniform magnetic field as a perturbation

In 1965, Polonsky and Cohen-Tannoudji[63] derived the analytical solution when y is close to 0, which means the holding field can be treated as a perturbation. We will summarize their derivation in this section.

If a spin-$\frac{1}{2}$ particle with the gyromagnetic ratio γ is located in a uniform magnetic field $B_0 \hat{z}$ and an RF field as Eq. 4.3, the Hamiltonian is written as

$$H = \omega_d \hbar a^\dagger a + \omega_0 \hbar \hat{S}_z + \lambda \hbar \hat{S}_x (a + a^\dagger), \qquad (4.14)$$

where the magnetic dipole moment coupling to the uniform field B_0 is $\vec{\mu} \cdot \vec{B}_0 = \gamma \hbar \hat{S}_z B_0 = \omega_0 \hbar \hat{S}_z$, the

photon energy from the RF field is $\omega_d \hbar a^\dagger a$ and the magnetic dipole moment coupling to the RF field is $V_{\sigma_x} = \lambda \hbar \hat{S}_x (a + a^\dagger)$ where λ is a coupling constant related to the strength of the RF field. If the quantum state is set as a coherent state α for the RF field [28], then

$$a \left| \alpha \right\rangle = \alpha \left| \alpha \right\rangle , \; and \; [a, a^\dagger] = 1, \tag{4.15}$$

The parameter α is simply related to the average number, $\bar{n} \gg 1$, of the RF photons,

$$\bar{n} = \left\langle \alpha \right| a^\dagger a \left| \alpha \right\rangle = \alpha^2. \tag{4.16}$$

The interaction term is related to the RF field such that

$$\lambda \left\langle \alpha \right| a^\dagger + a \left| \alpha \right\rangle = 2\lambda\alpha = 2\lambda\sqrt{\bar{n}} = \gamma B_d \tag{4.17}$$

Consequently, $\lambda = \gamma B_d / 2\sqrt{\bar{n}}$. The creation and the annihilation operators can be expressed in terms of the normalized position and momentum operators, $\hat{X}$ and $\hat{P}$, as

$$a \equiv \hat{X} + i\hat{P}/2, \; a^\dagger \equiv \hat{X} - i\hat{P}/2. \tag{4.18}$$

Then the Hamiltonian can be written as

$$H = \omega_d \hbar (\hat{X}^2 + \hat{P}^2/4) + \lambda \hbar \hat{S}_x (2\hat{X}) + \omega_0 \hbar \hat{S}_z = \omega_d \hbar \hat{P}^2/4 + \omega_d \hbar (\hat{X}^2 + \frac{2\lambda}{\omega_d} \hat{S}_x \hat{X}) + \omega_0 \hbar \hat{S}_z$$

$$= \omega_d \hbar \hat{P}^2/4 + \omega_d \hbar (\hat{X} + \frac{\lambda}{\omega_d} \hat{S}_x)^2 + \omega_0 \hbar \hat{S}_z - \frac{\hbar}{\omega_d} (\lambda \hat{S}_x)^2. \tag{4.19}$$

Two new operators are defined as

$$b \equiv \hat{X} + \frac{\lambda}{\omega_d} \hat{S}_x + i\hat{P}/2 = a + \frac{\lambda}{\omega_d} \hat{S}_x \tag{4.20}$$

$$b^\dagger \equiv \hat{X} + \frac{\lambda}{\omega_d} \hat{S}_x - i\hat{P}/2 = a^\dagger + \frac{\lambda}{\omega_d} \hat{S}_x \tag{4.21}$$

so that the Hamiltonian can be rewritten as

$$H = \omega_d \hbar b^\dagger b + \omega_0 \hbar \hat{S}_z - \frac{\hbar}{\omega_d} (\lambda \hat{S}_x)^2. \tag{4.22}$$

The last term only depends on $\hat{S}_x$ and a constant for eigenstates of b (or a). The eigenstates of the first term are $\left| n_b \right\rangle$; however, what we really want is the eigenstates of a. A unitary transformation of b to a is needed so that we can treat it as the translation from $\hat{X}$ to $\hat{X} + \frac{\lambda}{\omega_d} \hat{S}_x$. We assume a unitary operator

$U(\chi) = e^{\chi(a^\dagger - a)} = e^{-i\chi \cdot \hat{P}}$ so that

$$f(\chi) \equiv U^\dagger(\chi) a^\dagger U(\chi) = b^\dagger \tag{4.23}$$

The derivative of $f(\chi)$ with respect to χ is

$$\frac{df(\chi)}{d\chi} = U^\dagger(\chi)((i\hat{P})a^\dagger - a^\dagger(i\hat{P}))U(\chi) = U^\dagger(\chi)((a - a^\dagger)a^\dagger - a^\dagger(a - a^\dagger))U(\chi)$$

$$= U^\dagger(\chi)(aa^\dagger - a^\dagger a)U(\chi) = U^\dagger(\chi)([a, a^\dagger])U(\chi) = 1 \tag{4.24}$$

Thus $f(\chi) = \chi + constant$ and $f(0) = a^\dagger = constant$. Therefore χ can be solved by using

$$f(\chi) = \chi + a^\dagger = b^\dagger = a^\dagger + \frac{\lambda}{\omega_d}\hat{S}_x \Rightarrow \chi = \frac{\lambda}{\omega_d}\hat{S}_x \tag{4.25}$$

Consequently, the unitary transformation operator is $\exp[\frac{\lambda}{\omega_d}\hat{S}_x(a^\dagger - a)]$.

If we treat the $\omega_0 \hbar \hat{S}_z$ term as a perturbation ($B_0 \ll B_d$)[20], the unperturbed eigenstates are

$$\overline{|n, m_x\rangle} = |n_a\rangle |m_x\rangle = U^\dagger(\chi)|n_b\rangle |m_x\rangle$$

$$= \exp[-\frac{\lambda}{\omega_d}\hat{S}_x(a^\dagger - a)]|n_b\rangle |m_x\rangle = \exp[-\frac{\lambda m_x}{\omega_d}(a^\dagger - a)]|n_b\rangle |m_x\rangle$$

$$= \overline{|n_{m_x}\rangle} |m_x\rangle . \tag{4.26}$$

The eigenvalues of energy are

$$E = n\omega_d \hbar - \hbar(\lambda \hat{S}_x)^2/\omega_d = n\omega_d \hbar - \hbar(\lambda m_x)^2/\omega_d \tag{4.27}$$

so that the states $m_x = \pm\frac{1}{2}$ are degenerate. The eigenstates $\overline{|n_{m_x}\rangle}$ satisfy

$$f_q(2\chi, n) \equiv \overline{\left\langle n_{+\frac{\hbar}{2}}|(n-q)_{-\frac{\hbar}{2}}\right\rangle} = \left\langle n \left| \exp[2\chi(a^\dagger - a)]\right| n - q\right\rangle \tag{4.28}$$

$$\frac{df_q(2\chi, n)}{d(2\chi)} = \left\langle n \left| \exp[2\chi(a^\dagger - a)](a^\dagger - a)\right| n - q\right\rangle$$

$$= \left\langle n \left| \exp[2\chi(a^\dagger - a)]\sqrt{n - q + 1}\right| n - q + 1\right\rangle - \left\langle n \left| \exp[2\chi(a^\dagger - a)]\sqrt{n - q}\right| n - q - 1\right\rangle$$

$$= \sqrt{n - q + 1} f_{q-1}(2\chi, n) - \sqrt{n - q} f_{q+1}(2\chi, n) \tag{4.29}$$

where $2\chi \equiv \lambda/\omega_d$.

The solution is obtained by expanding the exponential operator in a series which is equivalent to the expansion of the Bessel function $J_q(2\lambda\sqrt{n}/\omega_d)$ in the case when $n, n - q \gg x$ where $\gamma B_d = 2\lambda\sqrt{n}$. The

36

definition of the Bessel function of the first kind is

$$J_q(x) = \sum_{s=0}^{\infty} \frac{(-1)^s}{s!(q+s)!} (\frac{x}{2})^{q+2s}, \tag{4.30}$$

$$J_0(x) = \sum_{s=0}^{\infty} \frac{(-1)^s}{s!(s)!} (\frac{x}{2})^{2s} = 1 - (\frac{x^2}{4}) + \frac{x^4}{32} + \cdots, \tag{4.31}$$

$$J_0(2x\sqrt{n}) = 1 - x^2 n + \frac{x^4 n^2}{2} + \cdots. \tag{4.32}$$

Since

$$e^A e^B = e^{A+B+\frac{1}{2}[A,B]} \tag{4.33}$$

$$\exp[\frac{\lambda}{\omega_d}(a^\dagger - a)] = \exp[\frac{\lambda}{\omega_d} a^\dagger] \exp[-\frac{\lambda}{\omega_d} a] \exp[-\frac{\lambda^2}{2\omega_d^2}], \tag{4.34}$$

we can get

$$\left\langle n \left| \exp[\frac{\lambda}{\omega_d}(a^\dagger - a)] \right| (n-q) \right\rangle = \left\langle n \left| \exp[\frac{\lambda}{\omega_d} a^\dagger] \exp[-\frac{\lambda}{\omega_d} a] \exp[-\frac{\lambda^2}{2\omega_d^2} \right| n-q \right\rangle$$

$$= \exp[-\frac{\lambda^2}{2\omega_d^2}] \left\langle n \left| [\sum_m (\frac{\lambda a^\dagger}{\omega_d})^m \frac{1}{m!}][\sum_s (-\frac{\lambda a}{\omega_d})^s \frac{1}{s!}] \right| n-q \right\rangle. \tag{4.35}$$

We need $\left\langle n \left| (a^\dagger)^m a^s \right| n-q \right\rangle \neq 0$ so that $n - m = n - q - s$ which implies $m = q + s$ so that

$$\exp[-\frac{\lambda^2}{2\omega_d^2}] \sum_s \left\langle n \left| (-1)^s (\frac{\lambda}{\omega_d})^{q+2s} \frac{(a^\dagger)^{q+s}(a)^s}{(q+s)!s!} \right| n-q \right\rangle$$

$$= \exp[-\frac{\lambda^2}{2\omega_d^2}] \sum_s (-1)^s \frac{\sqrt{n(n-1)\cdots(n-q-s)}\sqrt{(n-q)(n-q-1)\cdots(n-q-s)}}{(q+s)!s!} (\frac{\lambda}{\omega_d})^{q+2s}$$

$$\approx \sum_s (-1)^s (\frac{\lambda\sqrt{n}}{\omega_d})^{q+2s} \frac{1}{(q+s)!s!}$$

$$= J_q(2\lambda\sqrt{n}/\omega_d), \tag{4.36}$$

if $n \gg x \Rightarrow \exp[-\frac{\lambda^2}{2\omega_d^2}] \to 1$ where $\gamma B_d \equiv 2\lambda\sqrt{n}$ and $x \equiv \gamma B_d/\omega_d$.

Since the states are degenerate for a fixed n, we calculate the effect of the perturbation $\omega_0 \hbar \hat{S}_z$ by calculating its matrix elements

$$\overline{\langle n', m_x'|} \omega_0 \hbar \hat{S}_z \overline{|n, m_x\rangle} = \left\langle m_x' \left| \hat{S}_z \right| m_x \right\rangle \overline{\left\langle n_{m_x'}' | n_{m_x} \right\rangle} \omega_0$$

$$= \left\langle m_x' \left| \hat{S}_z \right| m_x \right\rangle \left\langle n' \left| \exp[(m_x' - m_x)(\lambda/\omega_d)(a^\dagger - a)] \right| n \right\rangle \omega_0$$

$$= \left\langle m_x' \left| \hat{S}_z \right| m_x \right\rangle J_{n'-n}((m_x' - m_x)(x))\omega_0. \tag{4.37}$$

37

Since

$$\left|m_x = +\frac{1}{2}\right\rangle = \begin{pmatrix} 1 \\ 0 \end{pmatrix}, \left|m_x = -\frac{1}{2}\right\rangle = \begin{pmatrix} 0 \\ 1 \end{pmatrix} \tag{4.38}$$

and

$$\hat{\sigma}_x = \begin{pmatrix} 1 & 0 \\ 0 & -1 \end{pmatrix}, \hat{\sigma}_y = \begin{pmatrix} 0 & 1 \\ 1 & 0 \end{pmatrix}, \hat{\sigma}_z = \begin{pmatrix} 0 & -i \\ i & 0 \end{pmatrix} \tag{4.39}$$

in our $|m_x\rangle$ representation, the off-diagonal terms are $\left\langle \pm|\hat{S}_z|\mp \right\rangle = \mp i\frac{1}{2}$.

Only $m'_x = m_x \pm 1$ is available because of the selection rules on $\hat{S}_z$. Since $J_0(x) = J_0(-x)$, for the first order perturbation, the correction term of the Hamiltonian can be written as

$$V_n^{(1)} = \begin{pmatrix} 0 & -i\frac{\omega_0\hbar}{2}J_0(x) \\ +i\frac{\omega_0\hbar}{2}J_0(-x) & 0 \end{pmatrix}, \tag{4.40}$$

which can be diagonalized by transforming the eigenstates of $\hat{S}_x$, $|m_x\rangle$, to the eigenstates of $\hat{S}_z$, $|m_z\rangle$. The first order energy shift will be

$$E_n^{(1)} = \omega_0\hbar J_0(x)m_z, \tag{4.41}$$

where $m_z = \pm\frac{1}{2}$ and the factor $J_0(x)$ represents the modification of the magnetic moment by the dressing field. In the presence of an EDM interaction, ω_0 will be replaced by $\omega_0 + 2dE/\hbar$. The eigenstates in $|m_z\rangle$ basis can be written as

$$\overline{|n, m_z\rangle} = \frac{1}{\sqrt{2}}(\overline{|n_+\rangle}\left|m_x = +\frac{1}{2}\right\rangle + im\overline{|n_-\rangle}\left|m_x = -\frac{1}{2}\right\rangle), \tag{4.42}$$

with energy given by $n\omega_d\hbar + m_z\omega_0\hbar J_0(x) - \hbar(\lambda m_x)^2/\omega_d$. For the second order perturbation, the second order energy shift is

$$E_n^{(2)} = \sum_{s\neq n, m'_x - m_x = \pm 1} \frac{\left|\left\langle m'_x, s\left|\omega_0\hbar\hat{S}_z\right|m_x, n\right\rangle\right|^2}{E_s^0 - E_n^0} = \sum_{s\neq n, m'_x - m_x = \pm 1} \frac{(\mp i\frac{1}{2}J_{s-n}(\pm x)\omega_0\hbar)^2}{(s-n)\omega_d\hbar}$$

$$= \frac{1}{2}\frac{(\omega_0\hbar)^2}{\omega_d\hbar}\sum_{s-n=q\neq 0} \frac{J_q^2(x)}{q} = \frac{1}{2}\frac{(\omega_0\hbar)^2}{\omega_d\hbar}\sum_{q>0} \frac{J_q^2(x)}{q} + \frac{J_{-q}^2(x)}{-q} = 0. \tag{4.43}$$

The energy shift in the third order is proportional to $\omega_0\hbar(\omega_0/\omega_d)^2$ which is extremely small if $\omega_0/\omega_d \ll 1$.

4.4   Matrix elements

Eq. 4.14 shows the Hamiltonian in the uniform magnetic field and the RF field is

$$H = \omega_d\hbar a^\dagger a + \omega_0\hbar\hat{S}_z + V_{\sigma_x} = H_0 + V_{\sigma_x}. \tag{4.44}$$

To find the eigenvalues of the Hamiltonian, the matrix elements will be calculated first. $|n, \pm\rangle$ are the set of eigenstates of H_0 where n signifies the oscillating quanta of the dressing field and $+/-$ denotes the spin up/down state. The eigenvalues of H_0 are given by:

$$\langle n, \pm | H_0 | n, \pm \rangle = \langle n, \pm | \omega_d \hbar a^\dagger a + \omega_0 \hbar \hat{S}_z | n, \pm \rangle = \omega_d \hbar n \pm \frac{\omega_0 \hbar}{2}. \tag{4.45}$$

The spin operators, the creation and the annihilation operators can be applied to eigenstates so that

$$\hat{S}_\pm | \mp \rangle = \sqrt{(\frac{1}{2})(\frac{3}{2}) - (\mp \frac{1}{2})(\pm \frac{1}{2})} | \pm \rangle = | \pm \rangle, \tag{4.46}$$

$$a^\dagger | n \rangle = \sqrt{n+1} | n+1 \rangle, \tag{4.47}$$

$$a | n \rangle = \sqrt{n} | n-1 \rangle. \tag{4.48}$$

For the linear oscillatory field perpendicular to B_0, using Eq. 4.13, the matrix elements will be

$$\langle n+1, \mp | V_{\sigma_x} | n, \pm \rangle = \frac{1}{\sqrt{2}} (\langle n+1, \mp | V_{\sigma+} | n, \pm \rangle + \langle n+1, \mp | V_{\sigma-} | n, \pm \rangle) = \frac{\lambda \hbar}{2} \sqrt{n+1}, \tag{4.49}$$

$$\langle n-1, \mp | V_{\sigma_x} | n, \pm \rangle = \frac{1}{\sqrt{2}} (\langle n-1, \mp | V_{\sigma+} | n, \pm \rangle + \langle n-1, \mp | V_{\sigma-} | n, \pm \rangle) = \frac{\lambda \hbar}{2} \sqrt{n} \tag{4.50}$$

in the basis of

$$\begin{pmatrix} \vdots \\ |n+1, +\rangle \\ |n+1, -\rangle \\ |n, +\rangle \\ |n, -\rangle \\ |n-1, +\rangle \\ |n-1, -\rangle \\ \vdots \end{pmatrix}. \tag{4.51}$$

Using

$$\lambda \equiv \frac{\gamma B_d}{2\sqrt{n}}, \tag{4.52}$$

two dressing parameters are defined as $x \equiv \frac{\gamma B_d}{\omega_d}$ and $y \equiv \frac{\gamma B_0}{\omega_d}$ as well as Eq. 3.2 and Eq. 3.3. The Hamiltonian can be written as matrices so that H_0 is

$$H_0 = \hbar\omega_d \begin{pmatrix} \cdot & \cdot & & \cdot & & \cdot & & \cdot & & \cdot & & \cdot & & \cdot \\ \cdot & (n+1)+\frac{y}{2} & 0 & 0 & 0 & 0 & 0 & \cdot \\ \cdot & 0 & (n+1)-\frac{y}{2} & 0 & 0 & 0 & 0 & \cdot \\ \cdot & 0 & 0 & (n)+\frac{y}{2} & 0 & 0 & 0 & \cdot \\ \cdot & 0 & 0 & 0 & (n)-\frac{y}{2} & 0 & 0 & \cdot \\ \cdot & 0 & 0 & 0 & 0 & (n-1)+\frac{y}{2} & 0 & \cdot \\ \cdot & 0 & 0 & 0 & 0 & 0 & (n-1)-\frac{y}{2} & \cdot \\ \cdot & \cdot & \cdot & \cdot & \cdot & \cdot & \cdot & \cdot \end{pmatrix} \tag{4.53}$$

and V_{σ_x} is

$$V_{\sigma_x} = \hbar\omega_d \begin{pmatrix} \cdot & \cdot & \cdot & \cdot & \cdot & \cdot & \cdot & \cdot & \cdot & \cdot \\ \cdot & 0 & \frac{x}{4} & 0 & 0 & 0 & 0 & 0 & 0 & \cdot \\ \cdot & \frac{x}{4} & 0 & 0 & 0 & \frac{x}{4} & 0 & 0 & 0 & \cdot \\ \cdot & 0 & 0 & 0 & \frac{x}{4} & 0 & 0 & 0 & 0 & \cdot \\ \cdot & 0 & 0 & \frac{x}{4} & 0 & 0 & 0 & \frac{x}{4} & 0 & \cdot \\ \cdot & 0 & \frac{x}{4} & 0 & 0 & 0 & \frac{x}{4} & 0 & 0 & \cdot \\ \cdot & 0 & 0 & 0 & 0 & \frac{x}{4} & 0 & 0 & 0 & \cdot \\ \cdot & 0 & 0 & 0 & \frac{x}{4} & 0 & 0 & 0 & \frac{x}{4} & \cdot \\ \cdot & 0 & 0 & 0 & 0 & 0 & 0 & \frac{x}{4} & 0 & \cdot \\ \cdot & \cdot & \cdot & \cdot & \cdot & \cdot & \cdot & \cdot & \cdot & \cdot \end{pmatrix} . \tag{4.54}$$

where $\sqrt{\frac{n+1}{n}} \to 1$ if $n \gg 1$. Therefore, eigenvalues can be obtained by diagonalizing the matrix of the Hamiltonian.

Using the perturbation theory, the first order of the energy shift is zero and the second order of the energy shift is

$$\begin{aligned} E_{n,m_z}^{(2)} &= \sum_{s\neq n, m_z'-m_z=\pm 1} \frac{|\langle s, m_z'| V |n, m_z\rangle|^2}{E_{n,m_z}-E_{s,m_z'}} = \frac{|\hbar\omega_d x/4|^2}{E_{n,m_z}-E_{n+1,-m_z}} + \frac{|\hbar\omega_d x/4|^2}{E_{n,m_z}-E_{n-1,-m_z}} \\ &= |\hbar\omega_d\frac{x}{4}|^2 \left(\frac{1}{2m_z\omega_0\hbar-\omega_d\hbar} + \frac{1}{2m_z\omega_0\hbar+\omega_d\hbar}\right) = \hbar\gamma B_d \frac{x}{16}\left(\frac{1}{2m_z y-1} + \frac{1}{2m_z y+1}\right). \end{aligned} \tag{4.55}$$

The precession frequency is proportional to the energy difference $\Delta E = E_+ - E_-$ between the spin up and spin down states. Therefore, the frequency shift becomes

$$\Delta\omega^{eff} = \frac{1}{\hbar}(E_{n,+}^{(2)} - \Delta E_{n,-}^{(2)}) = \gamma B_d\frac{x}{8}\left(\frac{1}{y-1} + \frac{1}{y+1}\right) \tag{4.56}$$
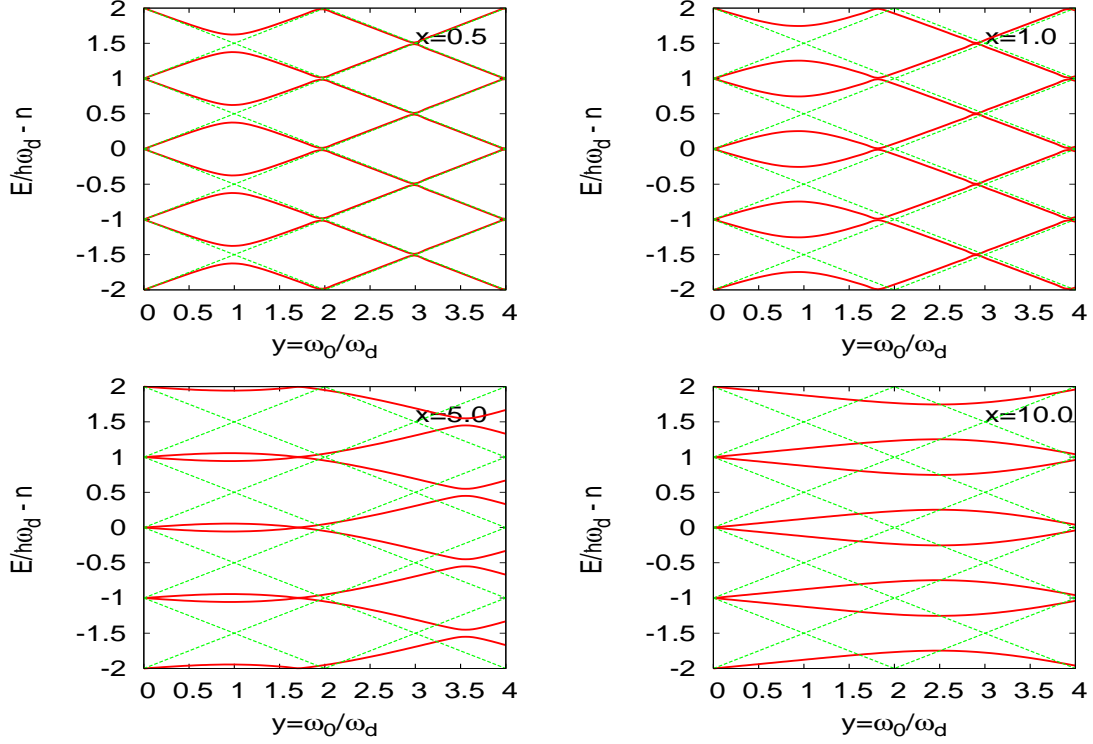
Figure 4.1: Energy diagrams for different x, i.e., different B_d.

which is compatible with Eq. 4.7.

4.5 Eigenvalues of the matrices

A $122-$by-122 matrix with maximum $\Delta n = 30$ was formed by inserting the elements of the matrices in Sec. 4.4. The matrix is then diagonalized to obtain the eigenvalues of different x and y. One example of the spectrum of eigenvalues is shown in Fig. 4.1. The red solid curves show the eigenvalues with the RF field B_d and the green dashed curves show the eigenvalues without the RF field, which is just the Zeeman splitting diagram.

4.6 Precession frequency calculation

How can one determine the precession frequency of particles in the dressing field? Fig. 4.2 shows an example of the spectrum of the energy eigenvalues E as a function of $y = \gamma B_0/\omega_d$ for $x = \gamma B_d/\omega_d = 1.57$. The energy difference $\Delta E = E_+ - E_-$ defines the effective precession frequency, $\omega^{eff} = \Delta E/\hbar$. It shows how the Zeeman splitting in the uniform field(green dashed lines) is modified by the presence of the dressing field (red solid lines). Without the dressing field, the gyromagnetic ratio for the Zeeman splitting is given by $\gamma = \Delta E/\hbar B_0$ which is just a constant independent of B_0, and the precession frequency is equal
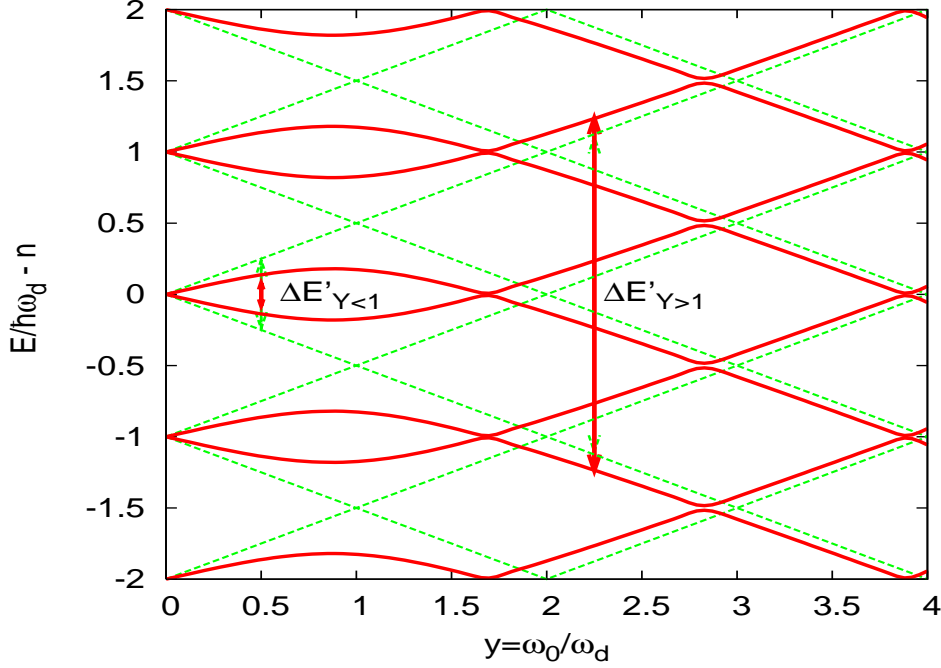
41

Figure 4.2: Sample energy diagram of the dressed spin system calculated as a function of y, for dressing parameter $x = 1.57$. Dashed lines indicate the Zeeman splittings in the undressed system ($E_0 = \pm\frac{1}{2}\omega_d\hbar$). The energy scale is given in units of the dressing field photon energy $\hbar\omega_d$.

to the Larmor frequency, $\omega_0 = \gamma B_0$. Adding the dressing field, Fig. 4.2 shows that E is changed to E' and γ now becomes $\gamma' = \Delta E'/\hbar B_0$; the new effective precession, ω^{eff}, is defined by the new energy slitting $\Delta E'$ such that $\Delta E'/\Delta E = \omega^{eff}/\omega_0$. It is interesting to note that for $y < 1$, $\Delta E' < \Delta E$ and γ' is smaller than γ. In contrast, for $y > 1$, $\Delta E' > \Delta E$ and γ' is now greater than γ. Fig. 4.3 shows ω^{eff}/ω_0 as a function of x for different y. If y is close to 0, the effective precession frequency is following the Bessel function as the result in Sec. 4.3. Now we can compare the precession frequency of the data with the prediction. The dashed curves in Fig. 3.6 are the calculations for $\omega^{eff}/\omega_0 = \gamma'/\gamma$ using the quantum mechanical method. The good agreement between the data and the calculation shows that the observed deviation can be quantitatively described in this quantum mechanical approach.

4.7 Critical dressing between UCN and ^{3}He

One motivation to study the dressed spin for the neutron EDM experiment is to determine the optimal setting for the dressing field. Using the quantum mechanical approach, we show some examples of the effective precession frequencies for UCN and ^{3}He in various regions (for $y < 1$ in Fig. 4.4 left and for $y > 1$ in Fig. 4.4 right). Fig. 4.4 shows that critical dressing, where ω^{eff} for ^{3}He and neutron are identical, can occur for various values of y and is not limited to the weak field ($y \ll 1$) condition. Fig. 4.5.a shows the first critical points, x_c, as a function of $y = \gamma B_0/\omega_d$. Fig. 4.5.b shows the corresponding values of ω^{eff}/ω_0
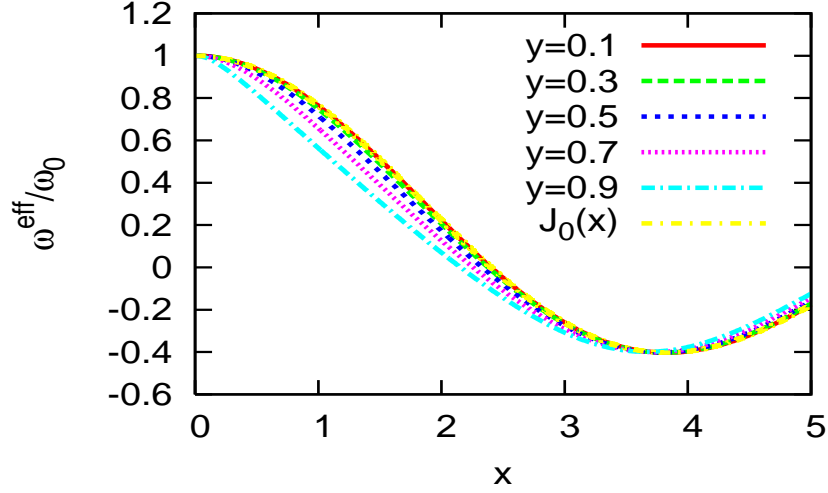
Figure 4.3: ω^{eff}/ω_0 vs. x for different y. The deviation from the Bessel function $J_0(x)$ can be observed when y is not close to 0.
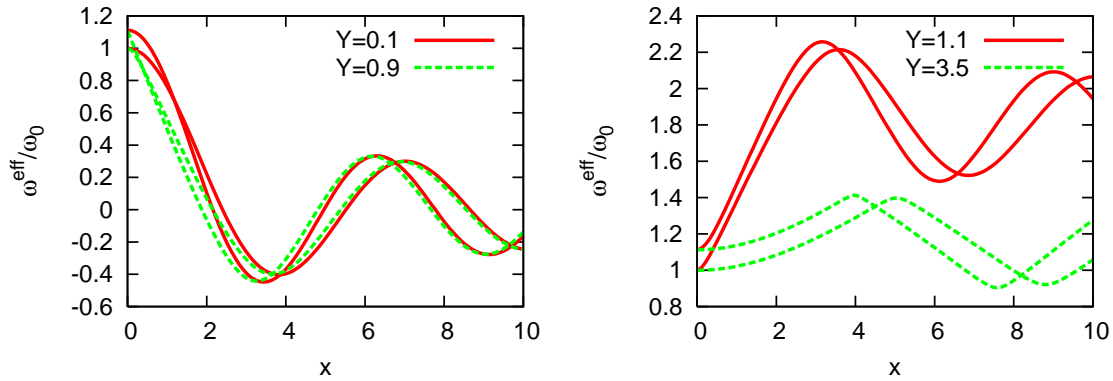

Figure 4.4: The effective precession frequency ratios vs. $x = \gamma B_d/\omega_d$. The curves with the initial value of $\omega^{eff}/\omega_0 = 1$ show neutron's effective precession frequency ratios and the curves with the initial value of $\omega^{eff}/\omega_0 \sim 1.112$ show ^{3}He's.

at the first critical point x_c. To determine the optimal setting for the dressing field, we need to consider various issues such as the power dissipation, spin relaxation, the stability of the critical point, and the implication on the systematic errors. Fixing $B_0 = 10$ mG, Fig. 4.6 shows the corresponding B_d and ω_d for the first critical point. Fixing $\omega_d = 3000$ mG, Fig. 4.7 shows the corresponding B_d and B_0 for the first critical point.
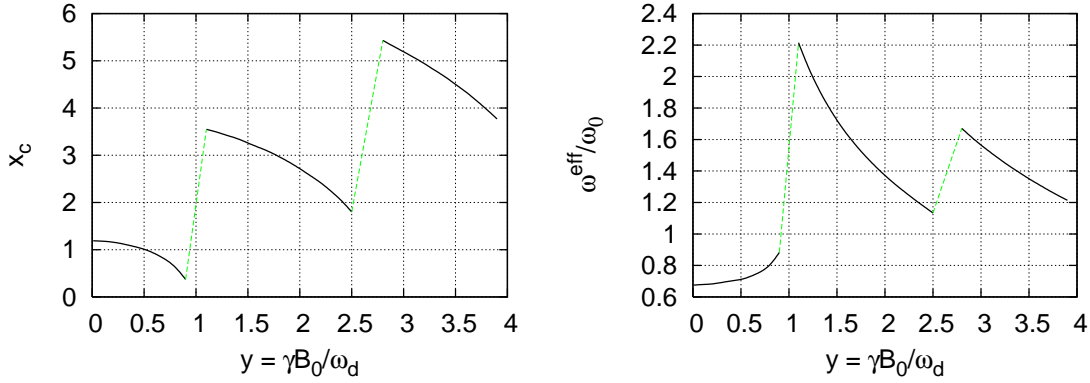
Figure 4.5: (a) The first critical points x_c vs. $y = \gamma B_0/\omega_d$ (b) The effective precession frequency ratio at the first critical point x_c vs. $y = \gamma B_0/\omega_d$.
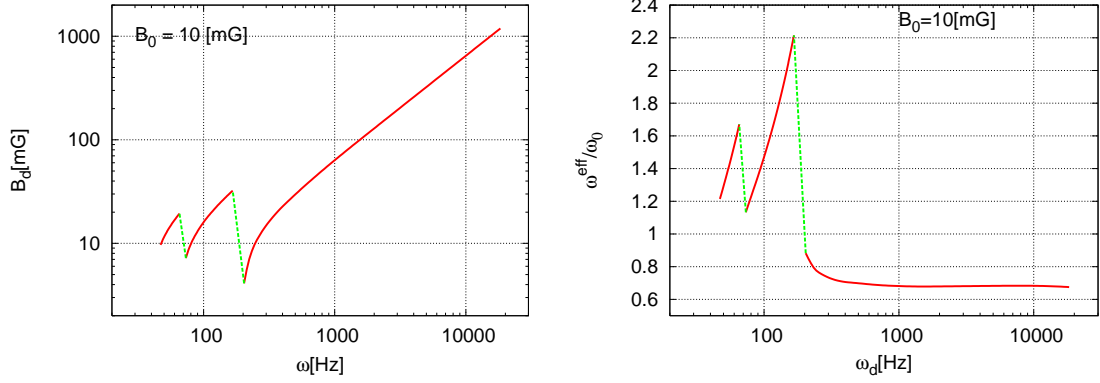

Figure 4.6: Fix $B_0 = 10$ mG. (a) The first critical points B_d vs. ω_d (b) The effective precession frequency ratio at the first critical point x_c vs. ω_d.
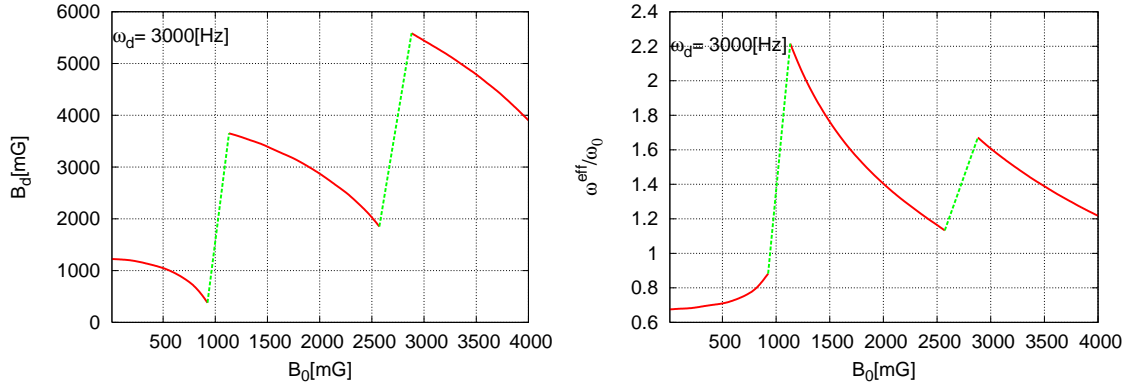

Figure 4.7: Fix $\omega_d = 3000$ Hz. (a) The first critical points B_d vs. B_0 (b) The effective precession frequency ratio at the first critical point x_c vs. B_0.

CHAPTER 5

SIMULATION OF THE DRESSED SPIN TECHNIQUE

The dressed spin technique for the nEDM experiment was first introduced by Golub and Lamoreaux in 1994 [29]. Precession frequencies of neutron and ^{3}He can be modified to become identical by applying an RF "dressing" field. In this chapter, we will discuss the simulation of the dressed spin technique. First, the EDM effective field and the pseudomagnetic field will be discussed. Second, some simulation tools will be described. Third, a simple review of the dressed spin technique in [29] will be given. The corresponding Monte Carlo will be generated using the parameters in the proposed neutron EDM experiment at the Spallation Neutron Source (SNS) at the Oak Ridge National Laboratory (ORNL) [12]. The difference between the idea in [29] and the proposed experiment [12] will be addressed. The statistic sensitivity will be estimated using the Monte Carlo. In the end, some possible systematic errors for the dressed spin technique will be discussed.

5.1 Electric dipole moment

In the presence of parallel (antiparallel) magnetic (B_0) and electric (E_0) fields, the Hamiltonian of a particle is defined as

$$H = -(\vec{\mu} \cdot \vec{B}_0 \pm \vec{d} \cdot \vec{E}_0) = -(\gamma \hbar \vec{S} \cdot \vec{B}_0 \pm d\frac{\vec{S}}{S} \cdot \vec{E}_0) = -\gamma \hbar \vec{S} \cdot (\vec{B}_0 \pm \frac{d}{\gamma \hbar S} \vec{E}_0) \tag{5.1}$$

where μ and d are the magnetic and electric dipole moments (EDM). An effective magnetic field due to EDM, called B_e, is defined as

$$\vec{B}_e = \frac{d}{\gamma \hbar S} \vec{E}_0 = \frac{2d}{\gamma \hbar} \vec{E}_0. \tag{5.2}$$

A shift in the precession frequency due to EDM will be

$$\omega_e = \gamma B_e = \frac{2dE_0}{\hbar}. \tag{5.3}$$

For a neutron EDM experiment with $E_0 = 50 \ KV/cm$ and $\gamma = \gamma_n = -2\pi \times 2.91647 \ Hz/mG$, the effective magnetic field for $d = d_n = 10^{-26} \ e \ cm$ is

$$\tilde{B}_e = \frac{2 \times 10^{-26} \ e \ cm \times 50 \ KV \ cm^{-1}}{-2.91656954 \times 2\pi \ s^{-1} \ mG^{-1} \times 6.58211915 \times 10^{-19} \ KeV \ s} = -8.29053 \times 10^{-8} \ mG, \tag{5.4}$$

and the frequency shift is

$$\omega_e = \gamma_n \tilde{B}_e = 1.51927 \ \mu Hz. \tag{5.5}$$

5.2 Pseudomagnetic field

The pseudomagnetic field could lead to some systematic errors for the neutron EDM experiment. This field will mimic a small but non-negligible magnetic field along the spin orientation of ^{3}He. We will first estimate the magnitude of the pseudomagnetic field in this section. The effect of the pseudomagnetic field will be included in the $n+^3$He simulation described later.

The pseudomagnetic field is originated from the real part of the spin-dependent scattering length. The scattering of a neutron by a single nucleus can be described by the Born approximation, and the Fermi pseudopotential is

$$V_F = \frac{2\pi\hbar^2}{m} b\delta(r), \tag{5.6}$$

where r is the position of the neutron relative to the nucleus, m is the neutron mass, and b is the bound scattering length [1] which is in general complex $b = b' - ib''$ [78]. The effective scattering length between a neutron and a nucleus includes various interactions [77].

The neutron has a spin $\vec{S}$ and the nucleus has a spin $\vec{I}$. The Fermi pseudopotential is generally spin-dependent so that the most general expression for b is

$$b = b_c + \frac{2b_i}{\sqrt{I(I+1)}} \vec{S} \cdot \vec{I}, \tag{5.7}$$

where b_c and b_i are called the bound coherent and incoherent scattering lengths [91]. Since the neutron spin is $S = \frac{1}{2}$, the total spin of neutron and nucleus is $J = I \pm \frac{1}{2}$. The corresponding scattering lengths are b_+ and b_-, given as [91]

$$b_- = b_c - \sqrt{\frac{I+1}{I}} b_i, \quad b_+ = b_c + \sqrt{\frac{I}{I+1}} b_i. \tag{5.8}$$

---

[1] The relation to the scattering length a of a nucleus free to recoil is $b = \frac{A+1}{A} a$, where A is the nucleus/neutron mass ratio [41].

If we consider the propagation of slow neutrons through a macroscopic sample, the non-absorptive part of V_F is given by

$$V_F = \frac{2\pi\hbar^2}{m}\rho b_c' + \frac{2\pi\hbar^2}{m}\rho\frac{2b_i'}{\sqrt{I(I+1)}}\vec{S}\cdot\vec{I} - \vec{\mu}\cdot\vec{B}. \tag{5.9}$$

where b_c' is the real part of b_c, b_i' is the real part of b_i, ρ is the number density of the nuclei and m is the neutron mass [91]. The first term is due to the spin-independent neutron-nucleus scattering. The third term is due to the neutron magnetic moment $\vec{\mu}$. The second term, the pseudomagnetic term, can be rewritten as

$$\begin{aligned}
V_{F,pm} &= \frac{2\pi\hbar^2}{m}\rho\frac{2b_i'}{\gamma}\sqrt{\frac{I}{I+1}}(\gamma\vec{S})\cdot\frac{\vec{I}}{I} = -(\gamma\hbar\vec{S})\cdot[-\frac{2\pi\hbar}{m\gamma}\rho b_i'\sqrt{\frac{I}{I+1}}\frac{\vec{I}}{I}] \\
&= -\vec{\mu}\cdot[-\frac{2\pi\hbar}{m\gamma}\rho b_i'\sqrt{\frac{I}{I+1}}\vec{P}] \\
&= -\vec{\mu}\cdot\vec{B}_a \tag{5.10}
\end{aligned}$$

where the neutron magnetic moment $\vec{\mu} = \gamma\hbar\vec{S}$ [2], the nuclear polarization $\vec{P} = \frac{\vec{I}}{I}$ and the pesudomagnetic field

$$\vec{B}_a = -\frac{2\pi\hbar}{m\gamma}\rho b_i'\sqrt{\frac{I}{I+1}}\vec{P}. \tag{5.11}$$

$I = \frac{1}{2}$ for the ^{3}He nucleus. Using data in [78], the bound scattering lengths in unit fm are

$$b_c = 5.74 - 1.483i, \quad b_i = -2.5 + 2.568i. \tag{5.12}$$

The pseudomagnetic field is

$$\vec{B}_a = -(2.15885\times 10^{22}\ fm^2\ mG)\rho(-2.5\ fm)\sqrt{\frac{1/2}{3/2}}\vec{P} = (3.11603\times 10^{22}\ fm^3)\rho\vec{P}. \tag{5.13}$$

For a ^{3}He density [3] of $\rho = \rho_3 = 1.653\times 10^{-27}\ fm^{-3}$ and $P = P_3 = 1$, the magnitude of $\vec{B}_a$ is $\tilde{B}_a = 5.15\times 10^{-5}\ mG$. The corresponding precession frequency is $\omega_a = \gamma_n\tilde{B}_a = 2\pi\times 0.1502\ mHz \sim 1mHz$.

5.3   Simulation tools

Detailed simulation has been performed to understand the roles of the dressing field for the nEDM experiment. We will describe how to simulate the spin dynamics in a time-dependent magnetic fields.

---

[2] $\gamma = \gamma_n = -2.91656954\times 2\pi\ Hz/mG$.

[3] Use the equation, $1/\tau_3 = \rho_3\sigma_0 v_n$, in Sec.3.3 of [29], where $\tau_3 = 500\ sec$, $\sigma_0 = 5.5\times 10^3$ barns is the average absorption cross section of neutron and ^{3}He when neutron velocity is $v_n = 2200$ m/s. The density of ^{3}He is $\rho_3 = 1/(\tau_3\sigma_0 v_n) = 1.653\times 10^{12}\ cm^{-3}$.

Several techniques are used in this study, including the numerical method for solving differential equation, and the Monte Carlo method.

5.3.1 Bloch equation

The Bloch equation,

$$\frac{d\vec{S}(t)}{dt} = \gamma \vec{S}(t) \times \vec{B}(t),$$ (5.14)

is used to simulate the spin dynamics in a time-dependent magnetic field. The Bloch equation can be solved numerically to obtain the time-dependences of the three spin components. In Eq. B.1, the gyromagnetic ratio, γ, of neutron (n) and ^{3}He (3) are

$$\gamma_n/2\pi = -2.91647 \; Hz/mG$$ (5.15)

$$\gamma_3/2\pi = -3.24341 \; Hz/mG$$ (5.16)

given by CODATA [4]. $\vec{B}(t)$ is a time-dependent magnetic field including:

- The constant holding field, $B_0 \hat{z}$,

- The dressing field, $B_d \cos \omega_d t \hat{x}$,

- The modulation field of the dressing field, $B_m Sign(\cos \omega_m t) \cos \omega_d t \hat{x}$,

- The time-dependent pseudomagnetic field, $\vec{B}_a(t) \parallel \vec{S}_3(t)$,

- The EDM effective field, $B_e \hat{z}$.

The modulation field may have other forms. Therefore, the expression for $\vec{B}(t)$ is

$$B_x = (B_d + B_m Sign(\cos \omega_m t)) \cos (\omega_d t) + B_{a,x}(t)$$
$$B_y = B_{a,y}(t)$$
$$B_z = B_0 \pm B_e + B_{a,z}(t).$$ (5.17)

The relative angle between neutron and ^{3}He is defined as

$$\cos \theta_{n3} = \left\langle \hat{S}_n \cdot \hat{S}_3 \right\rangle.$$ (5.18)

---

[4]`http://physics.nist.gov/cuu/Constants/index.html`

5.3.2 Runge-Kutta method

A popular method to solve a differential equation is the fourth-order Runge-Kutta method, which evolved from the simple Euler method. In the Euler method,

$$y_{n+1} = y_n + hf'(x_n, y_n) \tag{5.19}$$

which advances a solution from x_n to $x_{n+1} = x_n + h$. The fourth-order Runge-Kutta formula is

$$
\begin{aligned}
k_1 &= hf'(x_n, y_n) \\
k_2 &= hf'(x_n + \frac{h}{2}, y_n + \frac{k_1}{2}) \\
k_3 &= hf'(x_n + \frac{h}{2}, y_n + \frac{k_2}{2}) \\
k_4 &= hf'(x_n + h, y_n + k_3).
\end{aligned} \tag{5.20}
$$

and the value of y_{n+1} at x_{n+1} is

$$y_{n+1} = y_n + \frac{1}{6}(k_1 + 2k_2 + 2k_3 + k_4). \tag{5.21}$$

The Runge-Kutta method was applied to solve the Bloch's equation. The procedure is

$$
\begin{aligned}
\vec{k_1} &= \Delta t \ \gamma \ \vec{S}_n \times \vec{B}(t) \\
\vec{k_2} &= \Delta t \ \gamma \ (\vec{S}_n + \frac{\vec{k_1}}{2}) \times \vec{B}(t + \frac{\Delta t}{2}) \\
\vec{k_3} &= \Delta t \ \gamma \ (\vec{S}_n + \frac{\vec{k_2}}{2}) \times \vec{B}(t + \frac{\Delta t}{2}) \\
\vec{k_4} &= \Delta t \ \gamma \ (\vec{S}_n + \vec{k_3}) \times \vec{B}(t + \Delta t),
\end{aligned} \tag{5.22}
$$

and the value $\vec{S}_{n+1}$ is given as

$$\vec{S}_{n+1} = \vec{S}_n + \frac{1}{6}(\vec{k_1} + 2\vec{k_2} + 2\vec{k_3} + \vec{k_4}) \tag{5.23}$$

where we use a time step $\Delta t = 10^{-6} \ sec$.

5.3.3 Scintillation light rate

The interaction between neutrons and ^{3}He atoms will emit scintillation light in liquid ^{4}He, through the reaction in Eq. 2.23. The scintillation light signal depends on the relative angle between the polarizations of neutron and ^{3}He, $\vec{P}_n$ and $\vec{P}_3$. To obtain the distribution function of the scintillation light, the UCN loss

is written as

$$\frac{dN_{UCN}}{dt} = -(\frac{dN_{wall}}{dt} + \frac{dN_{sin,weak}}{dt} + \frac{dN_{sin,abs}}{dt}),$$ (5.24)

where N_{UCN} is the UCN number, N_{wall} is the number of neutrons absorbed by the wall, $N_{sin,weak}$ is the number of scintillation light signals due to the weak decay of neutrons (known as β decay) and $N_{sin,abs}$ is the number of the scintillation light signals due to the absorption of ^{3}He. Various terms in Eq. 5.24 are

$$\frac{dN_{wall}}{dt} = \frac{1}{\tau_{wall}} N_{UCN}(t),$$ (5.25)

$$\frac{dN_{sin,weak}}{dt} = \frac{1}{\tau_\beta} N_{UCN}(t),$$ (5.26)

$$\frac{dN_{sin,abs}}{dt} = \frac{1}{\tau_3} N_{UCN}(t)(1 - P(t)\cos\theta_{n3}(t)),$$ (5.27)

where τ's are decay constants for various effects, $P(t)$ is the product of the polarizations of neutron and ^{3}He as a function of time. The total loss of UCN becomes

$$\frac{dN_{UCN}}{dt} = -N_{UCN}(\frac{1}{\tau_{wall}} + \frac{1}{\tau_\beta} + \frac{1}{\tau_3}(1 - P(t)\cos\theta_{n3}(t)))$$ (5.28)

and the number of UCN is

$$N_{UCN} = N_0 \exp\left[-(\frac{1}{\tau_{wall}} + \frac{1}{\tau_\beta} + \frac{1}{\tau_3})t + \frac{1}{\tau_3}\int^t d\tau P(\tau)\cos\theta_{n3}(\tau)\right]$$ (5.29)

where N_0 is the initial number of UCN. The scintillation light rate is

$$\begin{aligned}
\frac{d\Phi}{dt} = \frac{dN_{sin}}{dt} &= \frac{dN_{sin,weak}}{dt} + \frac{dN_{sin,abs}}{dt} \\
&= N_0 \exp\left[-(\frac{1}{\tau_{wall}} + \frac{1}{\tau_\beta} + \frac{1}{\tau_3})t + \frac{1}{\tau_3}\int_0^t d\tau P(\tau)\cos\theta_{n3}(\tau)\right]\times \\
&\quad (\frac{1}{\tau_\beta} + \frac{1}{\tau_3}(1 - P(t)\cos\theta_{n3}(t))) \\
&= N_0 \exp\left[-\Gamma_{ave}t + \frac{1}{\tau_3}\int_0^t d\tau P(\tau)\cos\theta_{n3}(\tau)\right](\frac{1}{\tau_\beta} + \frac{1}{\tau_3}(1 - P(t)\cos\theta_{n3}(t))),
\end{aligned}$$ (5.30)

where Γ_{ave} is defined as

$$\Gamma_{ave} = \frac{1}{\tau_\beta} + \frac{1}{\tau_3} + \frac{1}{\tau_{wall}}.$$ (5.31)

Eq. 5.30 will be used as the distribution function to generate Monte Carlo. Besides, the corresponding $\cos\theta_{n3}$ will be calculated using the Bloch equation. The scintillation signal will be simulated for different magnetic field setups.

5.4 Free case (without the dressing field)

In a uniform magnetic field B_0, neutron and ^{3}He precess at their Larmor frequencies, $\omega_n = \gamma_n B_0$ and $\omega_3 = \gamma_3 B_0$. The relative precession frequency is

$$\omega_l \equiv 2\pi f_l \equiv \omega_n - \omega_3 = (\gamma_n - \gamma_3)B_0 = 2\pi \times 0.327(Hz/mG) \times B_0 \tag{5.32}$$

and the relative angle will be

$$\theta_{n3}(t) = \omega_l t + \theta_0, \tag{5.33}$$

where θ_0 is the initial phase difference between the polarizations of neutron and ^{3}He. To simplify the equation of the scintillation light rate in Eq. 5.30, the polarizations of both neutron and ^{3}He are set to one $(P(t) = 1)$. Then, the scintillation light rate becomes

$$\frac{d\Phi}{dt} = N_0 \exp\left[-\Gamma_{ave}t + \frac{1}{\tau_3 \omega_l}((\cos\omega_l t - 1)\sin\theta_0 + \sin\omega_l t \cos\theta_0)\right]\left(\frac{1}{\tau_\beta} + \frac{1}{\tau_3}(1 - \cos(\omega_l t + \theta_0)))\right). \tag{5.34}$$

If the initial relative angle is zero $(\theta_0 = 0)$, the scintillation light rate will be simplified as

$$\frac{d\Phi}{dt} = N_0 \exp\left[-\Gamma_{ave}t + \frac{\sin\omega_l t}{\tau_3 \omega_l}\right]\left(\frac{1}{\tau_\beta} + \frac{1}{\tau_3}(1 - \cos\omega_l t)\right). \tag{5.35}$$

For a fast precession ω_l, for example $B_0 = 10\ mG$ and $\omega_l \sim 20.7\ Hz$, the term

$$\left|\frac{\sin(\omega_l t)}{\omega_l \tau_3}\right| < 0.0001 \tag{5.36}$$

can be ignored. Therefore, the scintillation light rate becomes

$$\frac{d\Phi}{dt} \sim N_0 e^{-\Gamma_{ave}t}\left(\frac{1}{\tau_\beta} + \frac{1}{\tau_3}(1 - \cos\omega_l t)\right), \tag{5.37}$$

where $N_0 = 1.68 \times 10^6$, $\tau_\beta = 885\ sec$, $\tau_3 = 500\ sec$ and $\tau_{cell} = 1150\ sec$ for the Monte Carlo [9].

5.4.1 Monte Carlo simulation of the free case

Monte Carlo of 10 runs are respectively generated for two cells placed in opposite electric field directions. The result will be compared with the sensitivity estimated using the method in [15].

The generating function is Eq. 5.30 where the term $\frac{1}{\tau_3}\int_0^t d\tau P(\tau)\cos\theta_{n3}(\tau)$ is also integrated step by step. An EDM effective field $B_e\hat{z}$ was added so that the relative precession frequency in cell 1 (cell 2) becomes $\omega_l - \omega_e$ $(\omega_l + \omega_e)$ where $\omega_e = 100\ \mu Hz$. The Bloch equation simulation will be applied to obtain

$\cos\left((\omega_l \pm \omega_e)t\right)$. The generated Monte Carlo can be fitted by using the function

$$f(t) = e^{-p_0 t}[p_1 - p_2 \cos\left(2\pi(p_3 + p_4)t + p_5\right)] + p_6 \tag{5.38}$$

where p_0 is the total decay constant, p_1 and p_2 are related to the product of the total neutron number and the decay constants, p_3 is fixed as the relative precession frequency f_l, p_4 is the relative precession frequency shift, p_5 is the initial relative phase shift and p_6 is the constant background. The standard deviation of p_4 is related to the statistical sensitivity of EDM. One example of the fitting is shown in Fig. 5.1 and the fitted parameters are listed in Table. 5.1. Fig. 5.2 shows that the standard deviation of p_4 is around 2.7 μHz for $N_0 = 1.68 \times 10^6$ [5].
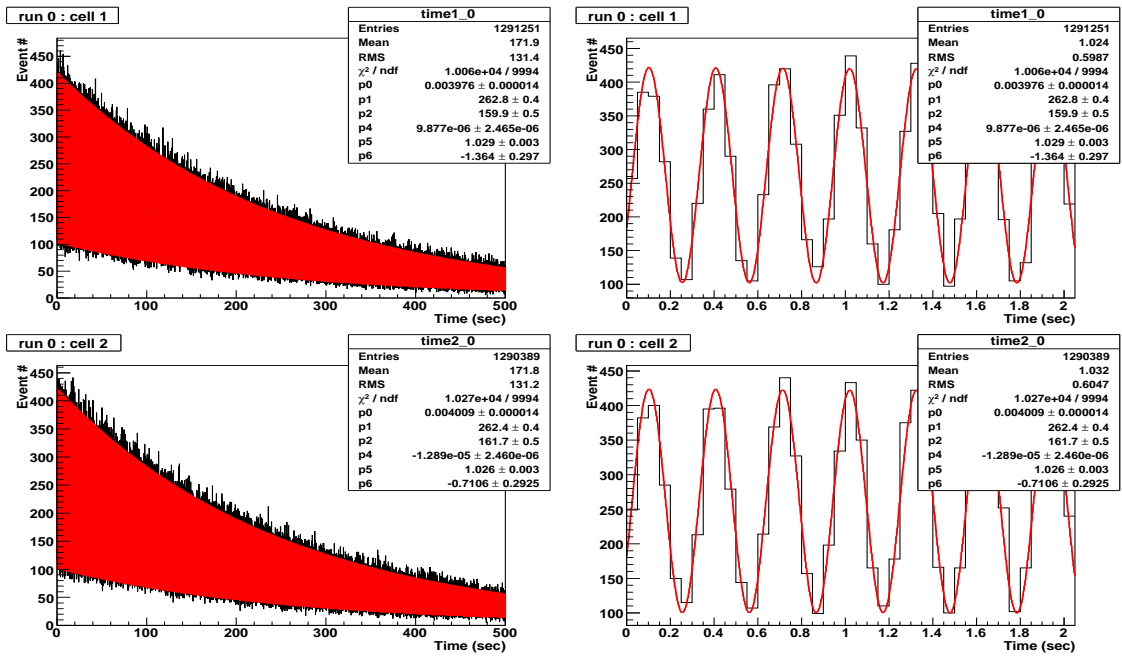
Figure 5.1: Fitting of the Monte Carlo. The fitted parameters of $f(t)$ are shown in Table 5.1. The right figures show the fits in a smaller time window.

---

[5]In fact, since only the time window $t = [0, 500]$ sec is used, the total neutron number is around 1.2×10^6.

Table 5.1: The fitted parameters of $f(t)$ for one Monte Carlo run.

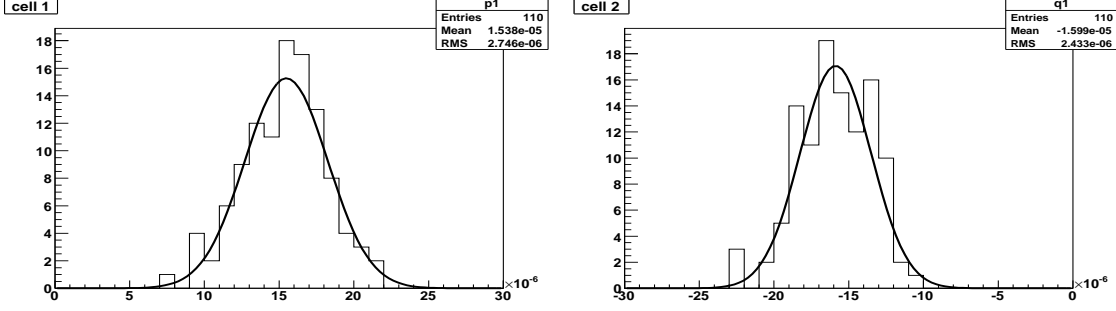|	Cell1			Cell 2	
	p_i	error		p_i	error
p_0	0.00397632	1.37748×10^{-5}	p_0	0.00400904	1.37388×10^{-5}
p_1	262.844	0.430667	p_1	262.432	0.430569
p_2	159.853	0.502974	p_2	161.682	0.504257
p_3	3.26941	fixed	p_3	3.26941	fixed
p_4	9.87702×10^{-6}	2.46506×10^{-6}	p_4	-1.28949×10^{-5}	2.45966×10^{-6}
p_5	1.02947	0.00337528	p_5	1.02576	0.00334389
p_6	-1.36403	0.297069	p_6	-0.710624	0.292453

Figure 5.2: The distribution of p_4. The total RMS of 20 runs is 2.594×10^{-6} Hz which is consistent with the estimation of Eq. 5.39. The mean difference is $\Delta \omega = 197.1$ μHz.

Using the analytical expression by Chibane et al. [15], the frequency variance can be estimated [9] as

$$\sigma_f^2 = \frac{6}{\pi^2}(\frac{\tau_3}{T})^2 \Gamma_{ave} \frac{1}{1-e^{-\Gamma_{ave}T}}(\frac{1}{\tau_3} + \frac{1}{\tau_\beta}) \tag{5.39}$$

where T is the period of the measurement for a single run. Using $\tau_\beta = 885$, $\tau_3 = 500$, $\tau_{wall} = 1150$ and $T = 500$, $\sigma_f = 2.97 \times 10^{-3}$ Hz which is consistent with the sensitivity obtained from our Monte Carlo study($N_0 \approx 1.2 \times 10^6$ so that $\sigma_f/\sqrt{N_0} = 2.7 \times 10^{-6}$ Hz).

Different pseudomagnetic fields are also examined in simulation. Fig. 5.3 shows pseudomagnetic fields at level of 10^{-4} mG will cause a frequency shift at order of 10^{-8} Hz, which is much smaller than the sensitivity at order of 10^{-6} Hz. Besides, the effect of the pseudomagnetic field is independent of the direction of electric fields. The effect will be further suppressed from a comparison between the two cells.
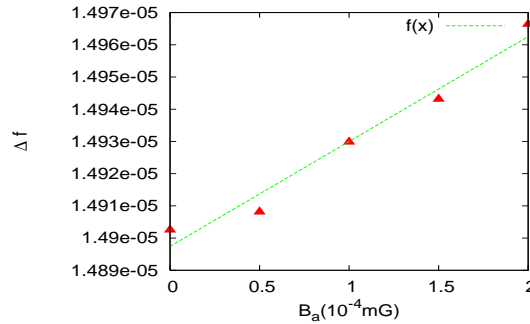

Figure 5.3: Pseudomagnetic field versus frequency shift. The slope is about 3.2×10^{-8} Hz.

5.5 Dressed spin

Here we briefly will review the dressed spin technique for the neutron EDM experiment. A particle with a spin $S = \frac{1}{2}$ in a constant magnetic field $B_0 \hat{z}$, called the holding field, will precess at the Larmor frequency $\omega_0 = \gamma B_0$. Then, an oscillatory RF field like $B_d(t) = B_d \cos \omega_d t \hat{x}$ in Eq. 4.3, called the dressing field, is

added to the system perpendicular to the holding field where B_d is the dressing field amplitude and ω_d is the dressing field frequency. Two dressing parameters are defined as $x \equiv \frac{\gamma_n B_d}{\omega_d}$ and $y \equiv \frac{\gamma_n B_0}{\omega_d}$ as well as Eq. 3.2 and Eq. 3.3 where γ_n is the gyromagnetic ratio of neutrons. The precession frequencies of neutron and ^{3}He can be modified by tuning these two parameters. If the dressing field frequency ω_d is high enough comparing with ω_n ($y = \omega_n/\omega_d << 1$), Fig. 5.4 shows the precession frequency is modified following the Bessel function [19]

$$\omega_n^d = \omega_n J_0(\frac{\gamma_n B_d}{\omega_d}), \ \omega_3^d = \omega_3 J_0(\frac{\gamma_3 B_d}{\omega_d}). \tag{5.40}$$

The relative precession frequency between neutron and ^{3}He will be

$$\omega_\gamma = \omega_n^d - \omega_3^d = \gamma_n B_0 J_0(\frac{\gamma_n B_d}{\omega_d}) - \gamma_3 B_0 J_0(\frac{\gamma_3 B_d}{\omega_d}). \tag{5.41}$$

There are critical points of x and y where neutron and ^{3}He precess at the same frequencies, called the critical dressing, i.e.,

$$\omega_\gamma = \omega_n^d - \omega_3^d = 0. \tag{5.42}$$

Solving $\gamma_n B_0 J_0(\frac{\gamma_n B_d}{\omega_d}) = \gamma_3 B_0 J_0(\frac{\gamma_3 B_d}{\omega_d})$, the solution of the lowest critical point is at $x_c = \frac{\gamma_n B_{d,c}}{\omega_d} \sim 1.189$, where $B_{d,c}$ is the critical dressing field. The advantage of applying the dressed spin technique is to eliminate the systematic error from a drift of B_0. If ω_γ is close to zero, the systematic error due to the drift of B_0 will be strongly suppressed [6].

The dressing parameters are set at $y = 0.01$ and $x = 1.189$ and $B_0 = 10$ mG for the neutron EDM experiment at the SNS. However, in reality, there is always a finite offset of the relative precession frequency. For example, for $x = 1.189$, ω_γ is

$$\omega_\gamma = \gamma_n B_0 J_0(1.189) - \gamma_3 B_0 J_0(\frac{\gamma_3}{\gamma_n}1.189) = 3.14547 \times 10^{-5} \ Hz \tag{5.43}$$

which is not zero. It is impossible to sit precisely at the critical dressing point in the real experiment. Nevertheless, the offset of the dressing field can be dealt with by applying a feedback scheme which can adjust the dressing field to correct for the offset.

5.5.1 Analytic solution of the dressed spin

Now we can consider the time dependence of $\langle \vec{\sigma} \rangle$. We take an initial state with $\langle \vec{\sigma} \rangle$ pointing along the $\hat{x}$ axis in the presence of the dressing field B_d. The matrix elements of $\hat{\sigma}_x, \hat{\sigma}_y, \hat{\sigma}_z$ in the basis of the

---

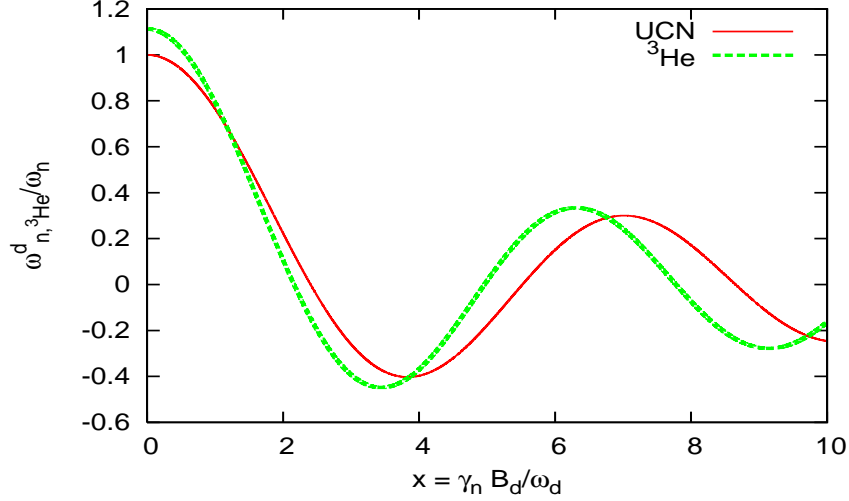[6]The necessary uniformity of the magnetic fields is described in Appendix F.

Figure 5.4: $\frac{\omega_n^d}{\omega_n} = J_0(x)$ and $\frac{\omega_3^d}{\omega_n} = \frac{\gamma_3}{\gamma_n}J_0(\frac{\gamma_3}{\gamma_n}x)$. ω_n is defined by $\omega_n = \gamma_n B_0$. It shows that the effective precession frequencies of neutron and ^{3}He can cross at several places. Usually we use the first point at $x_c \sim 1.189$ as the dressing point.

eigenstates Eq. 4.42 can be calculated. For $\hat{\sigma}_x$, we have

$$\exp\left[-i(n'\omega_d + \frac{1}{2}m\omega_0 J_0(x))t\right]\overline{\langle n',m'|\hat{\sigma}_x|n,m\rangle}\exp\left[i(n\omega_d + \frac{1}{2}m\omega_0 J_0(x))t\right]$$

$$= \frac{1}{2}[\overline{\langle n'_+|n_+\rangle} - (im')(im)(-1)\overline{\langle n'_-|n_-\rangle}]\exp\left[i((n-n')\omega_d + \frac{1}{2}(m-m')\omega_0 J_0(x))t\right]$$

$$= \delta_{n,n'}\frac{1}{2}(1-mm')\exp\left[\frac{1}{2}(m-m')\omega_0 J_0(x)t\right]$$

$$= \left\{ \begin{array}{ll} 0, & m=m' \\ \delta_{n,n'}\exp\left[\frac{i}{2}(m-m')\omega_0 J_0(x)t\right], & m \neq m' \end{array} \right\},$$

For $\hat{\sigma}_y$, we have

$$\exp\left[-i(n'\omega_d + \frac{1}{2}m'\omega_0 J_0(x))t\right]\overline{\langle n',m'|\hat{\sigma}_y|n,m\rangle}\exp\left[i(n\omega_d + \frac{1}{2}m\omega_0 J_0(x))t\right]$$

$$= \frac{1}{2}[\overline{\langle n'_+|n_-\rangle}im - \overline{\langle n'_-|n_+\rangle}im']\exp\left[i((n-n')\omega_d + \frac{1}{2}(m-m')\omega_0 J_0(x))t\right]$$

$$= \frac{1}{2}[J_{n'-n}(x)im - J_{n'-n}(-x)im']\exp\left[i((n-n')\omega_d + \frac{1}{2}(m-m')\omega_0 J_0(x))t\right]$$

$$= \frac{1}{2}[J_{-q}(x)im - J_{-q}(-x)im']\exp\left[i(q\omega_d + \frac{1}{2}(m-m')\omega_0 J_0(x))t\right]$$

$$= \frac{1}{2}[J_{-q}(x)im - (-1)^q J_{-q}(x)im']\exp\left[i(q\omega_d + \frac{1}{2}(m-m')\omega_0 J_0(x))t\right]$$

$$= \frac{1}{2}J_{-q}(x)i[m - m'(-1)^q]\exp\left[i(q\omega_d + \frac{1}{2}(m-m')\omega_0 J_0(x))t\right] \tag{5.44}$$

and finally, for $\hat{\sigma}_z$, we have

$$
\begin{aligned}
&\exp\left[-i(n^{'}\omega_d + \frac{1}{2}m^{'}\omega_0 J_0(x))t\right]\overline{\langle n^{'}, m^{'}|\hat{\sigma}_z\overline{|n, m\rangle}}\exp\left[i(n\omega_d + \frac{1}{2}m\omega_0 J_0(x))t\right] \\
=&\frac{1}{2}\overline{[\langle n^{'}_+|n_-\rangle}m + \overline{\langle n^{'}_-|n_+\rangle}m^{'}]\exp\left[i((n - n^{'})\omega_d + \frac{1}{2}(m - m^{'})\omega_0 J_0(x))t\right] \\
=&\frac{1}{2}[J_{n^{'}-n}(x)m + J_{n^{'}-n}(-x)m^{'}]\exp\left[i((n - n^{'})\omega_d + \frac{1}{2}(m - m^{'})\omega_0 J_0(x))t\right] \\
=&\frac{1}{2}[J_{-q}(x)m + (-1)^q J_{-q}(x)m^{'}]\exp\left[i(q\omega_d + \frac{1}{2}(m - m^{'})\omega_0 J_0(x))t\right] \\
=&\frac{1}{2}J_{-q}(x)[m + m^{'}(-1)^q]\exp\left[i(q\omega_d + \frac{1}{2}(m - m^{'})\omega_0 J_0(x))t\right]. \tag{5.45}
\end{aligned}
$$

If the initial state is set as a coherent state with spin along the $+x$ axis,

$$
\psi(t) = \sum_{n,m=\pm} a_n \frac{1}{\sqrt{2}}\overline{|n, m\rangle}\exp\left[i(n\omega_d + \frac{1}{2}m\omega_0 J_0(x))t\right], \tag{5.46}
$$

the time dependence of the expectation value of $\hat{\sigma}_x$ is

$$
\begin{aligned}
\langle\psi(t)|\,\hat{\sigma}_x\,|\psi(t)\rangle &= \langle\hat{\sigma}_x(t)\rangle \\
&= \sum_{n,n^{'}} a^*_{n^{'}}a_n\delta_{n,n^{'}}\cos(\omega_0 J_0(x)t) = \sum_n |a_n|^2\cos(\omega_0 J_0(x)t) = \cos(\omega_0 J_0(x)t), \tag{5.47}
\end{aligned}
$$

the expectation value of $\hat{\sigma}_y$ is

$$
\begin{aligned}
\langle\psi(t)|\,\hat{\sigma}_y\,|\psi(t)\rangle &= \langle\hat{\sigma}_y(t)\rangle \\
&= \sum_{n,n^{'},m,m^{'}} \frac{1}{2}a^*_{n^{'}}a_n\frac{1}{2}J_{-q}(x)i[m - m^{'}(-1)^q]\exp\left[i(q\omega_d + \frac{1}{2}(m - m^{'})\omega_0 J_0(x))t\right] \\
&= \sum_{n,q=even} a^*_{n-q}a_n\frac{1}{4}J_{-q}(x)i[2\exp[i(q\omega_d + \omega_0 J_0(x))t] - 2\exp[i(q\omega_d - \omega_0 J_0(x))t]] \\
&= \sum_{n,q=even} a^*_{n-q}a_n J_{-q}(x)i\exp[iq\omega_d t]i\sin(\omega_0 J_0(x)t) \\
&= -J_0(x)\sin(\omega_0 J_0(x)t) - \sum_{n,q>0,even} a^*_{n-q}a_n J_q(x)\cos(q\omega_d t)\sin(\omega_0 J_0(x)t), \tag{5.48}
\end{aligned}
$$

and the expectation value of $\hat{\sigma}_z$ is

$$\langle \psi(t) | \hat{\sigma}_z | \psi(t) \rangle = \langle \hat{\sigma}_z(t) \rangle$$

$$= \sum_{n,n',m,m'} \frac{1}{2} a_{n'}^* a_n \frac{1}{2} J_{-q}(x)[m + m'(-1)^q] \exp\left[i(q\omega_d + \frac{1}{2}(m - m')\omega_0 J_0(x))t\right]$$

$$= \sum_{n,q=odd} a_{n-q}^* a_n J_{-q}(x) \exp\left[i(q\omega_d)t\right] i \sin\left(\omega_0 J_0(x)t\right)$$

$$= \sum_{n,q>0,odd} a_{n-q}^* a_n J_q(x)(-i\sin\left(q\omega_d t\right)) i \sin\left(\omega_0 J_0(x)t\right)$$

$$= \sum_{n,q>0,odd} a_{n-q}^* a_n J_q(x) \sin\left(q\omega_d t\right) \sin\left(\omega_0 J_0(x)t\right) \tag{5.49}$$

For the SNS nEDM experiment, the absorption scintillation rate is related to the polarization of two particles, given by

$$\frac{1}{\tau_{abs}} = \frac{1}{\tau_3}(1 - \vec{P}_n \cdot \vec{P}_3), \tag{5.50}$$

where $1/\tau_3 = N_3 \sigma_0 v_n$, N_3 is ^{3}He number density (for $\tau_3 = \tau_\beta/10$, $N_3 \approx 10^{13}/cm^3$ is required), and τ_β is the effect of wall loss and β decay, v_n is the neutron velocity and σ_0 is the ^{3}He absorption cross section ($\sigma_0 = 5.5 \times 10^3$ b, $v_n = 2200 m/s$ and both the neutron and ^{3}He are unpolarized). Eq. 5.50 shows that the absorption rate depends on the expectation value of $\hat{\sigma}_n \cdot \hat{\sigma}_3$.

Using Eqs. 5.47—5.49, the time dependence of $\vec{\sigma}_n \cdot \vec{\sigma}_3$ can be calculated as

$$\langle \sigma_{nx} \sigma_{3x} \rangle = \cos\left(\omega_n t\right) \cos\left(\omega_3 t\right), \tag{5.51}$$

$$\langle \sigma_{ny} \sigma_{3y} \rangle = \sum_{n,q\geq 0,even} \sum_{n',q'\geq 0,even} (a_{n-q}^* a_n)_{UCN}(a_{n'-q'}^* a_{n'})_{He} J_q(x_n) J_{q'}(x_3)$$

$$\cos\left(q\omega_d t\right) \cos\left(q'\omega_d t\right) \sin\left(\omega_n t\right) \sin\left(\omega_3 t\right), \tag{5.52}$$

$$\langle \sigma_{nz} \sigma_{3z} \rangle = \sum_{n,q\geq 0,odd} \sum_{n',q'\geq 0,odd} (a_{n-q}^* a_n)_{UCN}(a_{n'-q'}^* a_{n'})_{He} J_q(x_n) J_{q'}(x_3)$$

$$\sin\left(q\omega_d t\right) \sin\left(q'\omega_d t\right) \sin\left(\omega_n t\right) \sin\left(\omega_3 t\right). \tag{5.53}$$

where $x_n = \gamma_n B_0/\omega_d$ and $x_3 = \gamma_3 B_0/\omega_d$. Using $q \ll n$, $\sum_n |a_n|^2 = 1$ where a_n is a slowly varying function of n, Eq. 5.52 and Eq. 5.53 can be simplified to

$$\langle \sigma_{ny} \sigma_{3y} \rangle = \sum_{q,q'\geq 0,even} J_q(x_n) J_{q'}(x_3) \cos\left(q\omega_d t\right) \cos\left(q'\omega_d t\right) \sin\left(\omega_n t\right) \sin\left(\omega_3 t\right) \tag{5.54}$$

$$\langle \sigma_{nz} \sigma_{3z} \rangle = \sum_{q,q'\geq 0,odd} J_q(x_n) J_{q'}(x_3) \sin\left(q\omega_d t\right) \sin\left(q'\omega_d t\right) \sin\left(\omega_n t\right) \sin\left(\omega_3 t\right). \tag{5.55}$$

Averaging over the fast frequency $q\omega_d(q \geq 1)$, then eventually

$$\langle \sigma_{ny}\sigma_{3y} \rangle \approx \sin(\omega_n t)\sin(\omega_3 t) \times \left(J_0(x_n)J_0(x_3) + 2\sum_{q\geq 0,even} J_q(x_n)J_q(x_3) \right) \tag{5.56}$$

$$\langle \sigma_{nz}\sigma_{3z} \rangle \approx \sin(\omega_n t)\sin(\omega_3 t) \times 2\sum_{q\geq 0,odd} J_q(x_n)J_q(x_3). \tag{5.57}$$

Therefore the dot product of the spin of two particles will be

$$\begin{aligned}
\langle \vec{\sigma}_n \cdot \vec{\sigma}_3 \rangle &= \langle \sigma_{nx} \cdot \sigma_{3x} \rangle + \langle \sigma_{ny} \cdot \sigma_{3y} \rangle + \langle \sigma_{nz} \cdot \sigma_{3z} \rangle \\
&= \cos(\omega_n t)\cos(\omega_3 t) + \sin(\omega_n t)\sin(\omega_3 t)J_0(x_n - x_3), \\
&= \frac{1}{2}[\cos(\omega_n + \omega_3)t + \cos(\omega_n - \omega_3)t] - \frac{1}{2}[\cos(\omega_n + \omega_3)t - \cos(\omega_n - \omega_3)t]J_0(x_n - x_3) \\
&= \frac{1}{2}[1 - J_0(x_n - x_3)]\cos(\omega_n + \omega_3)t + \frac{1}{2}[1 + J_0(x_n - x_3)]\cos(\omega_n - \omega_3)t. \tag{5.58}
\end{aligned}$$

where x_n At the critical dressing, $x_n \sim 1.189$, $x_3 \sim 1.32229$, $\omega_n = \omega_3 \sim 12.3985B_0$ and $J_0(x_n - x_3) = 0.995563$. $\langle \vec{\sigma}_n \cdot \vec{\sigma}_3 \rangle$ is very close to one since $J_0(x_n - x_3)$ is very close to 1.

5.5.2   Bloch equation simulation of the dressed spin

The Bloch equation simulation has been performed to calculate $\cos\theta_{n3}$. The result of the simulation is shown as the black curves in Fig. 5.5. The red curve corresponds to the calculation using Eq. 5.58. The oscillatory pattern of the red curve is from the first term of Eq. 5.58. It is interesting to note that neutron and ^{3}He do not precess exactly together even at the critical dressing; in fact, they precess forward and backward within a small angle. The angle is related to the amplitude of the oscillatory red curve, $1 - J_0(x_n - x_3)$, so that the small angle is equal to $Cos^{-1}(J_0(x_n - x_3)) = 5.4°$. Besides, the simulation also shows another oscillatory pattern at a high frequency equal to the dressing frequency, as shown in the bottom plot of Fig. 5.5. It requires extremely high timing resolution of the scintillation light signal to observe this effect. A film of the dressed spin dynamics of neutron and ^{3}He has been made and can be viewed at `http://www.youtube.com/watch?v=xBL_jDjtojc`. It shows that the spin is wobbling vertically such that the time average of the precession in the x-y plane becomes slower when the dressing field is applied.

5.5.3   Extraction of the neutron EDM in the dressed spin system

For an extremely small ω_γ, the initial phase θ_0, which is the angle between the UCN and ^{3}He spin, is a dominant factor affecting the sensitivity. This can be explained by considering the signal and background
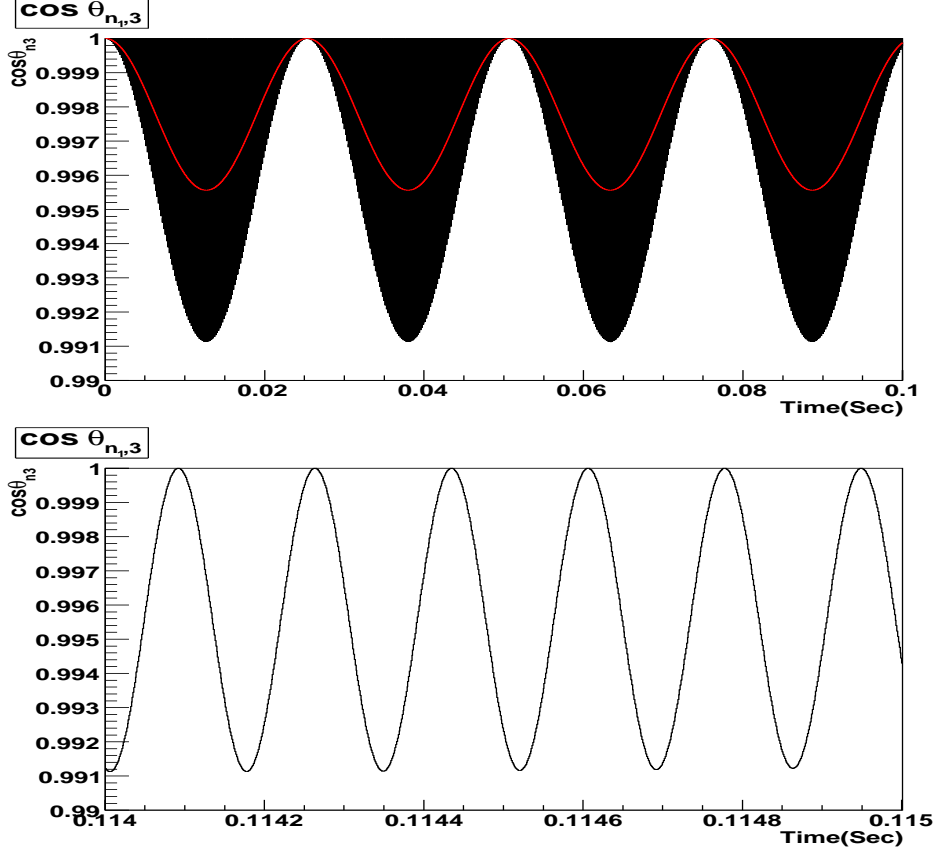
58

Figure 5.5: Simulation of $\cos\theta_{n3}(t)$. $B_0 = 10$ mG, $y = 0.01$ and $x = 1.189$. Black curve is Bloch equation simulation and red curve is Eq. 5.58. The simulation also shows another oscillatory pattern at a high frequency equal to the dressing frequency.

ratio when $\theta_0 = 0$, the background function $f_B(t)$ and the signal function $f_S(t, \omega_\gamma)$ can be defined as

$$f_B(t) = e^{-(\frac{1}{\tau_\beta} + \frac{1}{\tau_{wall}})t} \frac{1}{\tau_\beta}, \tag{5.59}$$

$$f_S(t, \omega_\gamma) = e^{-(\frac{1}{\tau_\beta} + \frac{1}{\tau_{wall}})t} \frac{1}{\tau_3}(1 - \cos(\omega_\gamma t)). \tag{5.60}$$

$f_B(t)$ and $f_S(t, \omega_\gamma)$ are plotted for different ω_γ's in Fig. 5.7. The integrations of the background and the signal over the measurement period $t = [0, 500]$ *sec* are defined as

$$B \equiv \int_0^{500} f_B(t)dt, \tag{5.61}$$

$$S(\omega_\gamma) \equiv \int_0^{500} f_S(t, \omega_\gamma)dt. \tag{5.62}$$

The ratio of $S(\omega_\gamma)/B$ is plotted in Fig. 5.8. We can see a turning point once f_γ is smaller than 1000μHz, which reflects the poor sensitivity at smaller frequencies.

How can one observe EDM signal if the dressing field is applied? Inspired by [24] and [44], the neutron

59
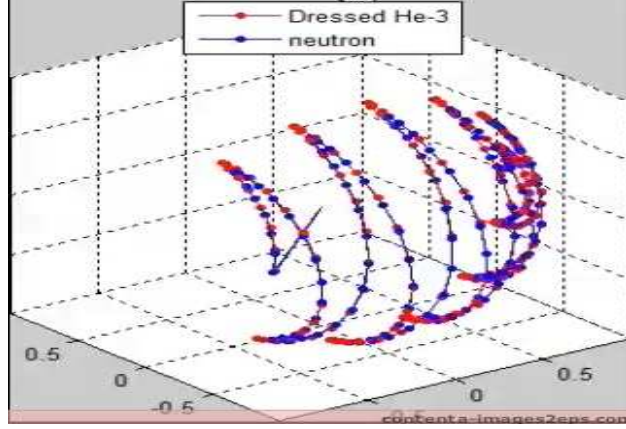
Figure 5.6: Simulation of dressed spin dynamics. The film is at
http://www.youtube.com/watch?v=xBL_jDjtojc.
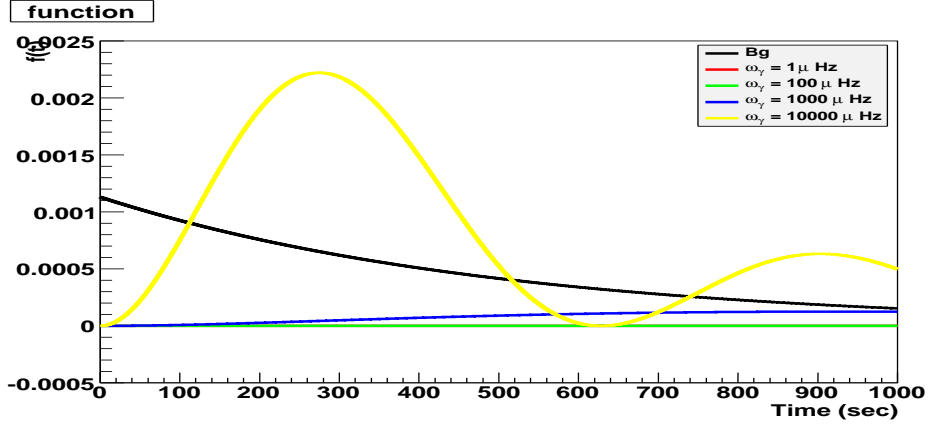
Figure 5.7: $f_B(t)$ and $f_S(t, \omega_\gamma)$ for ω_γ=1,100,1000, 10000μHz.

EDM signal can be derived from the number of scintillation signals integrated over the measurement period T [18]. The initial phase θ_0 is considered for a small ω_γ so that Eq. 5.34 becomes

$$\frac{d\Phi}{dt} \approx N_0 \exp\left[-\Gamma_{ave}t + \frac{t}{\tau_3}\cos\theta_0\right]\left(\frac{1}{\tau_\beta} + \frac{1}{\tau_3}(1 - \cos\theta_0 + \omega_\gamma t\sin\theta_0)\right)$$

$$\equiv N_0 \exp\left[-At\right](B + C\omega_\gamma t), \tag{5.63}$$

where $A = \Gamma_{ave} - \frac{\cos\theta_0}{\tau_3}$, $B = \frac{1}{\tau_\beta} + \frac{1}{\tau_3}(1 - \cos\theta_0)$ and $C = \frac{\sin\theta_0}{\tau_3}$. The number of scintillator signals integrated over the measurement period T is

$$\Phi(T, \omega_\gamma) = \int_0^T \frac{d\Phi}{dt}dt = N_0[\frac{B}{A}(1 - e^{-AT}) + \omega_\gamma\frac{C}{A^2}(1 - (1 + AT)e^{-AT})]. \tag{5.64}$$

If an EDM effective field is added, cell 1 (cell 2) has the relative precession frequency: $\omega_\gamma + \omega_e^d$ ($\omega_\gamma - \omega_e^d$) so

60
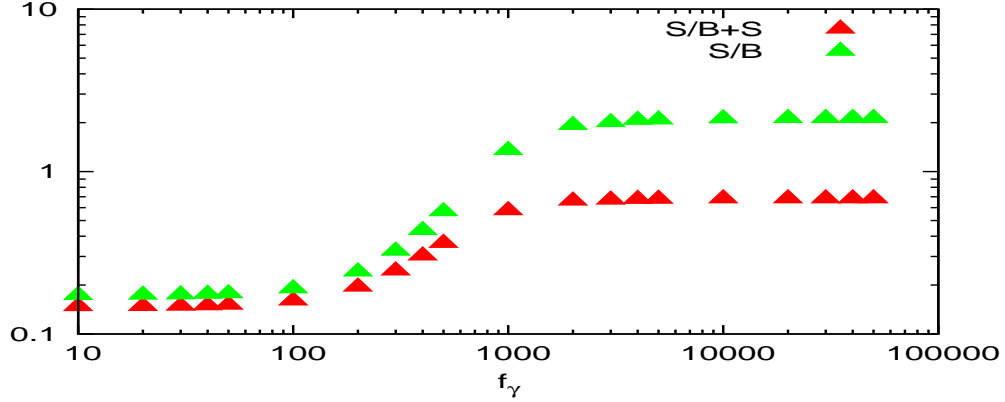
Figure 5.8: $S(f_\gamma)/B$ and $S(f_\gamma)/S(f_\gamma) + B$ vs. f_γ

that the total event number difference between two cells is proportional to ω_e^d:

$$\Delta\Phi = \omega_e^d \cdot 2N_0\frac{C}{A^2}(1 - (1 + AT)e^{-AT}). \tag{5.65}$$

A parameter is defined as $S = \frac{\Phi}{N_0}$ which is independent of the initial neutron number N_0. The frequency variance can be calculated as

$$\sigma_f^2 = \frac{\sigma_\omega^2}{(2\pi)^2} = \frac{\sigma_S^2}{(2\pi)^2}[\frac{dS}{d\omega_e^d}]^{-2} = \frac{S}{(2\pi)^2}[\frac{dS}{d\omega_e^d}]^{-2} = \frac{1}{(2\pi)^2}\frac{B}{A}(1 - e^{-AT})/(\frac{C}{A^2}(1 - (1 + AT)e^{-AT}))^2. \tag{5.66}$$

Using $\tau_\beta = 885\ sec$, $\tau_3 = 500\ sec$, $\tau_{wall} = 1150\ sec$ and $T = 500\ sec$, Fig. 5.9 shows $\frac{dS}{d\omega_e^d}$ and σ_f as a function of θ_0. Comparing with Eq. 5.39, the dressed spin technique can compete with the free case if the initial angle is tuned. Here we do not consider other parameters, like the continuous background, the polarization of neutron and ^{3}He, the efficiency of the PMTs, etc. Those parameters should be optimized to achieve the maximum sensitivity.

5.5.4 Monte Carlo simulation of the dressed spin system with an initial relative angle $\theta_0 = 90°$

In order to check the validity of Eq. 5.66, we have carried out Monte Carlo simulation. Monte Carlo are generated for the parameters of $\theta_0 = 90°$, $\tau_\beta = 885\ sec$, $\tau_3 = 500\ sec$, $\tau_{wall} = 1150\ sec$, $T = 500\ sec$, $N_0 = 1.68 \times 10^6$ and $x = 1.189$, $y = 0.01$. The Bloch equation is applied to calculate $\cos\theta_{n3}$ in the cell 1 (cell 2) with the frequency $\omega_\gamma + \omega_e^d$ ($\omega_\gamma - \omega_e^d$), where $\omega_e^d = 10^{-6} \times J_0(1.189)\ Hz$. The integration of the function Eq. 5.30 over the measurement period is

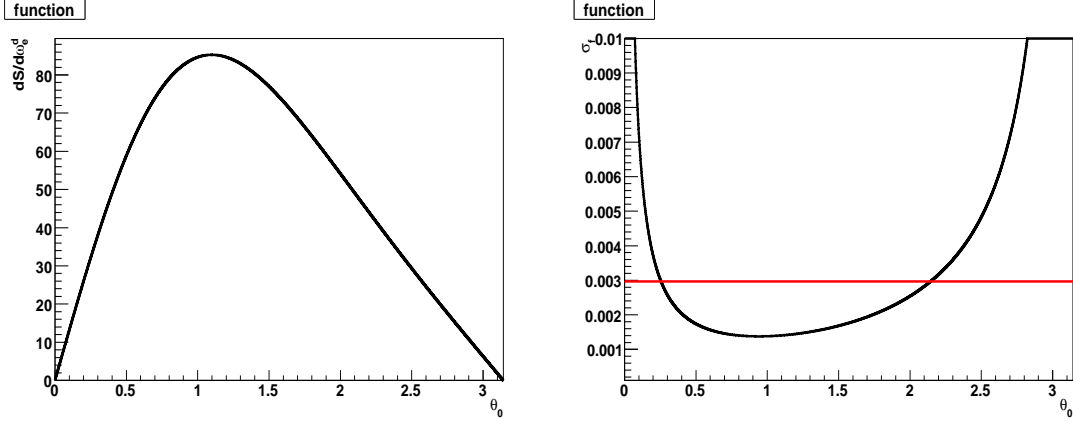$$N_\pm = \int_0^{500} \frac{d\Phi(\omega_\gamma \pm \omega_e^d)}{dt}dt. \tag{5.67}$$

Figure 5.9: Left) $\frac{dS}{d\omega_e^d}$ and Right) σ_f versus θ_0 which is in radian. The black curve is Eq. 5.66 and the red curve is Eq. 5.39.

For each run, the number of event will be randomly given by using the Poisson distribution. Fig. 5.10 shows the distribution of the total event number of 10 runs for cell 1 and cell 2 within $t = [0, 500]$ sec and the standard deviation is $\sigma_\Phi \approx 1146$. From Eq. 5.64, the standard deviation of Φ is

$$\sigma_\Phi = \sigma_{\omega_e^d} \frac{\partial \Phi}{\partial \omega_e^d} = (\sigma_{\omega_e} \times J_0(1.189)) \cdot 2.22 \times 10^8 \approx 1146 \tag{5.68}$$

and the value of σ_{ω_e} is around 7.63 μHz for the initial neutron number $N_0 = 1.68 \times 10^6$. The calculation using Eq. 5.66 is $\sigma_{\omega_e} = 5.2$ μHz. The discrepancy is due to the offset of the dressing field shown in Eq. 5.43. The offset would cause a significant variation for the total event number.
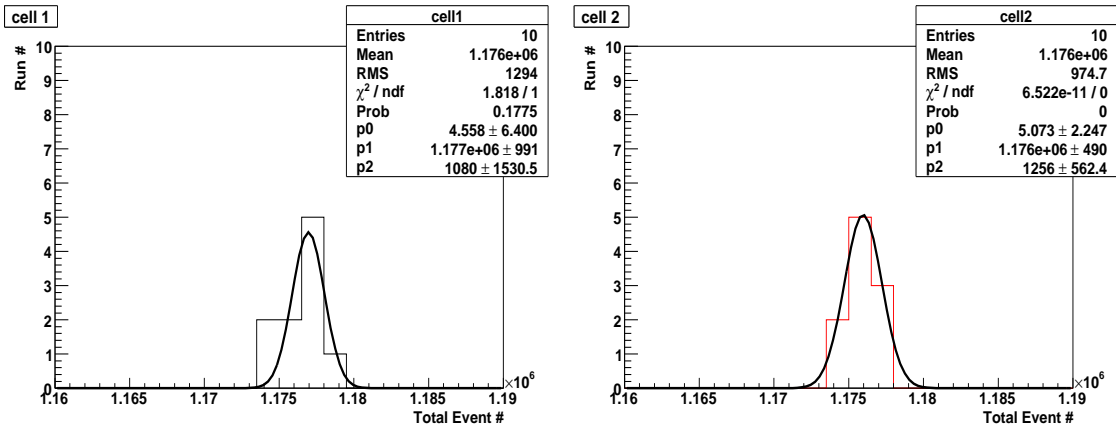
Figure 5.10: Event number for cell 1 and cell 2. The mean difference is 495 so that the frequency difference is $\Delta\omega_e \sim 3.3$ μHz.

The sensitivity of the dressed spin technique is comparable to the free case if the initial angle θ_0 is not close to zero. However, for the method utilizing the total event number described above, it will not be easy to determine ω_e directly from the data without knowing precisely the distribution function of the data and

62

other parameters, like neutron density, etc. In the next sections other methods will be introduced to overcome the difficulty.

5.6   Modulated dressing field

It is clear that when the system is at the critical dressing where neutron and ^{3}He have the same precession frequency with $\theta_0 = 0°$, there is no absorption signal. This problem can be solved by modulating the dressing field so that x can deviate from the critical point x_c and the relative angle θ_{n3} between neutron and ^{3}He is varied periodically. The variation of θ_{n3} will affect the rate of the scintillation light. The difference of the scintillation light signal between the first and the second half cycles will reveal a non-zero EDM plus an offset from the critical point x_c.

Upon the application of a square-wave modulation field, the dressing field becomes

$$B_d(t) = [B_{d,c} + B_m Sign(\cos(\omega_m t))] \cos \omega_d t, \tag{5.69}$$

where $B_{d,c}$ is the critical dressing field, B_m is the modulation field and $\omega_m = 2\pi f_m = 2\pi/\tau_m$ is the modulation frequency. A modulation parameter is defined as

$$x_m \equiv \frac{\gamma_n B_m}{\omega_d}. \tag{5.70}$$

The relative precession frequency at the positive modulation field is

$$\omega_{z,0}^+ = \omega_n[J_0(x_c + x_m) - aJ_0(a(x_c + x_m))], \tag{5.71}$$

and at the negative modulation field is

$$\omega_{z,0}^- = \omega_n[J_0(x_c - x_m) - aJ_0(a(x_c - x_m))]. \tag{5.72}$$

Fig. 5.11 shows an example of the relative precession frequency and the relative angle as a function of time. The sequence of a single cycle of the modulation is as follow: first, the B_m is applied for a duration $\frac{1}{4}\tau_m$, then $-B_m$ is applied for a duration $\frac{1}{2}\tau_m$ and finally, B_m is applied for another $\frac{1}{4}\tau_m$. The cycle is then repeated. The corresponding angle θ_m between neutron and ^{3}He is shown in Fig. 5.11. We can see the modulated angle increasing and decreasing as a function of t. For a small modulation ($\theta_m \ll 1$), the scintillation rate $d\Phi/dt \propto 1 - \cos\theta_{n3} \approx 1 - (1 - \frac{\theta_{n3}^2}{2}) \approx \frac{1}{2}\theta_{n3}^2$.

The relative precession frequency for a small modulation x_m is around

$$|\omega_{z,0}^+| \approx |\omega_{z,0}^-| \approx |\omega_n|[J_0(x) - aJ_0(ax)]| = |\omega_n[J_0(x_c + x_m) - aJ_0(a(x_c + x_m))]|$$

$$\approx |\omega_n|[J_0'(x_c)x_m - aJ_0'(ax_c)x_m]| = |\omega_n[-J_1(x_c) + a^2J_1(ax_c)]x_m|$$

$$= |\omega_n \times 0.156077 \times x_m|, \qquad (5.73)$$

where $a \equiv \gamma_3/\gamma_n$. If the system is at the critical dressing point, the relative angle between neutron and ^{3}He varies equally in the positive and negative modulation. However, if there is an offset Δx from the critical point, then $|\omega_{z,0}^+|$ is not equal to $|\omega_{z,0}^-|$. For example, the relative precession frequency ω_γ as a function of Δx is

$$\omega_\gamma(\Delta x) = \omega_n[J_0(x + \Delta x) - aJ_0(a(x + \Delta x))] \qquad (5.74)$$

and then adding a modulation $x_m = 0.05$, the frequency is

$$\omega_{z,0}^\pm(\Delta x) = \omega_n[J_0(x + \Delta x \pm x_m) - aJ_0(a(x + \Delta x \pm x_m))]; \qquad (5.75)$$

At $\Delta x = 0$, $\Delta\omega_\gamma \equiv |\omega_{z,0}^+| - |\omega_{z,0}^-| \approx 0$ which means x is still close to the critical dressing. However, if $\Delta x = 0.05$, then $\Delta\omega_\gamma/2\pi \approx 0.45$ which means there is a phase difference $\Delta\omega_\gamma\tau_m/2$ after a cycle of the modulation. This difference is related to an EDM effective field or an offset of the dressing field. Both ω_γ and $\Delta\omega_\gamma$ are shown in Fig. 5.12 as a function of Δx.
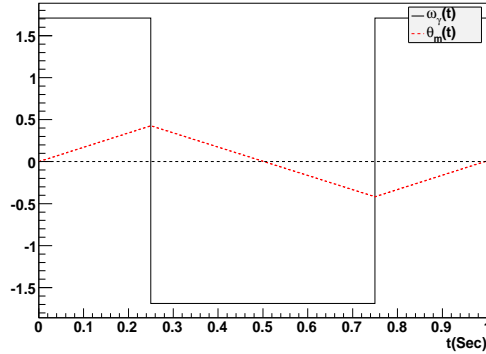

Figure 5.11: ω_γ and θ_m for the modulation field of the cosine square wave. $B_m = 0.05B_{d,c} = 59.45mG$, $f_m = 1\ Hz$, $B_0 = 10\ mG$, $y = 0.01$ and $x = 1.189$.

5.6.1   Effect of the neutron EDM with the modulated dressing field

An alternative idea to derive a neutron EDM is to use the modulation signal. The modulation signal with an offset is a linearly increasing first harmonic signal. If there is an offset of ω_e, the relative precession
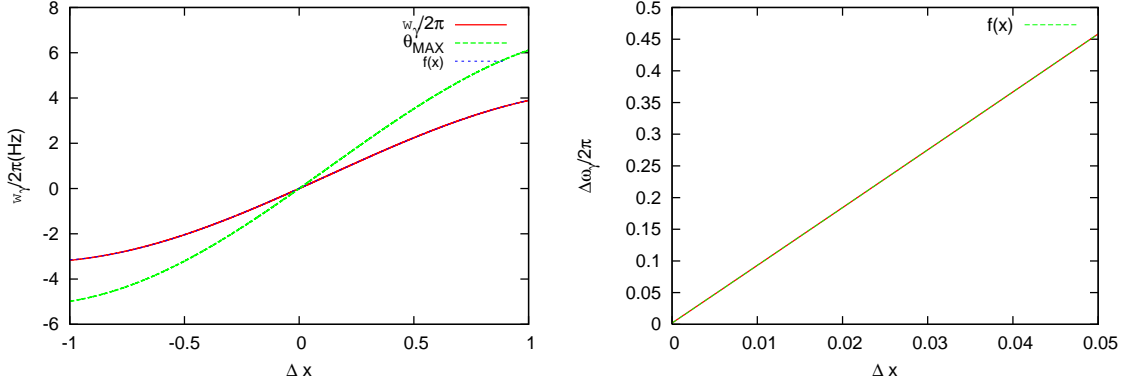
Figure 5.12: Left)The red curve is ω_γ versus Δx and the green curve is $\theta_{Max} \equiv \omega_\gamma \times \tau_m/4$ where $\tau_m = 1\ sec$. It can be roughly described by the function:$f(\Delta x) = -1.012\Delta x^3 + 0.368412\Delta x^2 + 4.53535\Delta x + 0.00524344$ where $x = 1.189$. Right) $\Delta\omega_\gamma$ versus Δx. ω_γ can be roughly described by the function:$f(\Delta x) = 9.1247\Delta x + 0.0017485$. The constant term 0.0017485 is from the offset for $x = 1.189$.

frequency for cell 1 becomes

$$\omega_{z,0}^\pm(\Delta x) = \omega_n[J_0(x \pm x_m) - aJ_0(a(x \pm x_m))] + \omega_e \tag{5.76}$$

and for cell 2 it becomes

$$\omega_{z,0}^\pm(\Delta x) = \omega_n[J_0(x \pm x_m) - aJ_0(a(x \pm x_m))] - \omega_e \tag{5.77}$$

as shown in Fig. 5.13. The offset of the ω_e will accumulate a phase difference between two cells. Since the scintillation light is proportional to $\cos\theta_{n3}$, the difference of $\cos\theta_{n3}$ between two cells is shown in Fig. 5.14 where the oscillation frequency depends on the modulation frequency. It shows that the scintillation signal is a linearly increasing first harmonic wave with the slope proportional to EDM $(\omega_e\tau_m)$. Fig. 5.15 shows the difference of $\cos\theta_{n3}$ between two cells for different modulation frequencies. Therefore, the slope of signal is related to the value of EDM. However, the real scintillation signal is not linearly increasing because of the neutron decays. We will apply the time evolution operator to describe the modulation signal in Sec. 5.6.2.

5.6.2   Time evolution of the UCN spin with the modulated dressing

One approach to treat the dressed spin is to use a density matrix formulation. Here we summarize the calculation in [29]. The pseudomagnetic field of ^{3}He will also be addressed [7]. Since the number of ^{3}He in the system is always much greater than UCN, the polarization of ^{3}He can be taken along the $\hat{x}$ axis in the ^{3}He rotating frame. In addition, the modulation field in the $\pm\hat{z}$ direction is $\pm\omega_{z,0}$ as mentioned in Eq. 5.73.

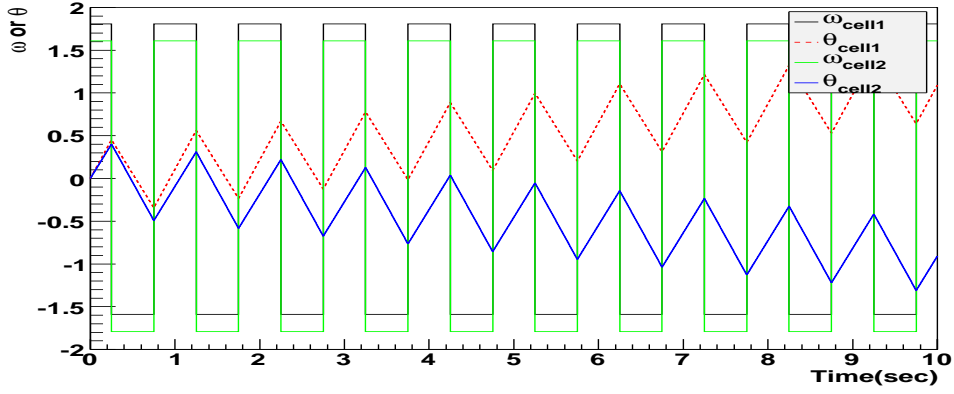[7]The calculation without considering the neutron EDM is described in Appendix G.

Figure 5.13: ω_γ and θ_{n3} for cell 1 and cell 2 with $\omega_e = 0.1\ Hz$.
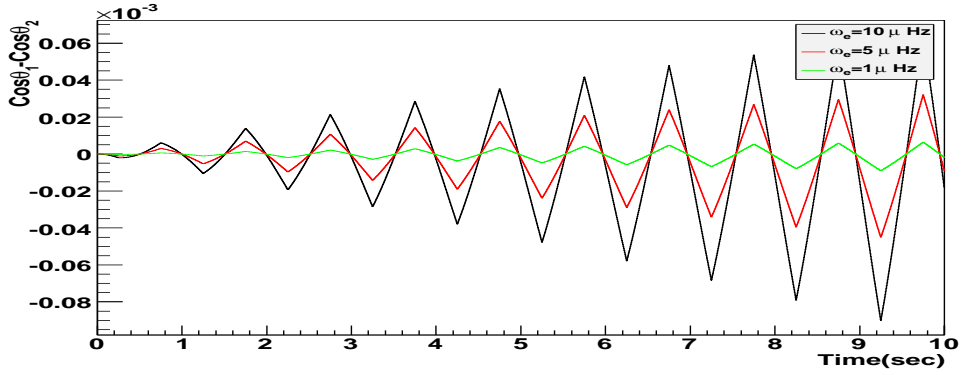

Figure 5.14: $\cos\theta_{n3,cell1} - \cos\theta_{n3,cell2}$ for different ω_e with $\tau_m = 1\ sec$.

The Hamiltonian for the interaction of neutron and ^{3}He in the ^{3}He rotating frame [29] can be written as

$$H_\pm = -i\hbar\frac{\Gamma}{2} + V_{F,pm} \pm \omega_{z,0}\hbar\hat{S}_z + \omega_e^d\hbar\hat{S}_z = -i\frac{\hbar}{2}[\frac{1}{\tau_0} - \frac{P_3}{\tau_3}\hat{\sigma}_x] + \omega_a\hbar\hat{S}_x \pm \omega_{z,0}\hbar\hat{S}_z + \omega_e^d\hbar\hat{S}_z, \qquad (5.78)$$

where $\frac{1}{\tau_0} = \frac{1}{\tau_\beta} + \frac{1}{\tau_3}$, $\omega_e^d = \omega_e J_0(x_c)$ and $\omega_a = \gamma B_a P_3$. The Pauli matrices $\hat{\sigma}_i$ are

$$\hat{\sigma}_x = \begin{bmatrix} 0 & 1 \\ 1 & 0 \end{bmatrix}, \hat{\sigma}_y = \begin{bmatrix} 0 & -i \\ i & 0 \end{bmatrix}, \hat{\sigma}_z = \begin{bmatrix} 1 & 0 \\ 0 & -1 \end{bmatrix} \qquad (5.79)$$

and $\hat{S}_i = \frac{1}{2}\hat{\sigma}_i$. The matrix representation of the interaction Hamiltonian is written as

$$H_\pm = -i\frac{\hbar}{2}\frac{1}{\tau_0}\begin{bmatrix} 1 & 0 \\ 0 & 1 \end{bmatrix} + \frac{\hbar}{2}\begin{bmatrix} \pm(\omega_{z,0} \pm \omega_e^d) & \omega_a' \\ \omega_a' & \mp(\omega_{z,0} \pm \omega_e^d) \end{bmatrix}, \qquad (5.80)$$

$$\omega_a' \equiv \omega_a + i\frac{P_3}{\tau_3} = \gamma B_a P_3 + i\frac{P_3}{\tau_3}, \qquad (5.81)$$
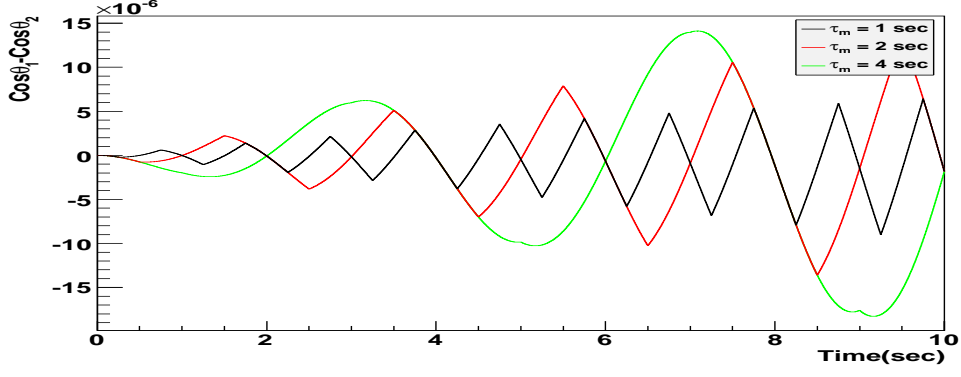
Figure 5.15: $\cos\theta_{n3,cell1} - \cos\theta_{n3,cell2}$ for different τ_m with $\omega_e = 1\ \mu\ Hz$.

where τ_3 is roughly $500\ sec$ and $2\pi/\gamma B_a \sim 2\pi/\gamma\tilde{B}_a = 1/(0.3 \times 10^{-3}) = 3333\ sec$. Then, using

$$\exp\left(-i\phi\vec{\sigma}\cdot\hat{n}\right) = \hat{I}\cos\phi - i\vec{\sigma}\cdot\hat{n}\sin\phi, \tag{5.82}$$

the time-evolution operator is

$$U_{\pm}(t) = \exp\left(-i\frac{H_{\pm}}{\hbar}t\right) = \exp\left(-\frac{1}{2}\frac{t}{\tau_0}\right)[\hat{I}\cos V_{\pm}t - i\vec{\sigma}\cdot\frac{\vec{V_{\pm}}}{V_{\pm}}\sin V_{\pm}t],$$

$$= \exp\left(-\frac{1}{2}\frac{t}{\tau_0}\right)\begin{bmatrix} \cos Vt \mp i\frac{1}{2}\frac{\omega_{z,0}\pm\omega_e^d}{V_{\pm}}\sin V_{\pm}t & -i\frac{1}{2}\frac{\omega_a'}{V_{\pm}}\sin V_{\pm}t \\ -i\frac{1}{2}\frac{\omega_a'}{V_{\pm}}\sin V_{\pm}t & \cos V_{\pm}t \pm i\frac{1}{2}\frac{\omega_{z,0}\pm\omega_e^d}{V_{\pm}}\sin V_{\pm}t \end{bmatrix}, \tag{5.83}$$

$$\vec{V}_{\pm} = \pm\frac{1}{2}(\omega_{z,0}\pm\omega_e^d)\hat{z} + \frac{1}{2}\omega_a'\hat{x}, \tag{5.84}$$

$$V_{\pm} = \frac{1}{2}\sqrt{(\omega_{z,0}\pm\omega_e^d)^2 + (\omega_a')^2} \approx \frac{1}{2}\sqrt{\omega_{z,0}^2 + (\omega_a')^2 \pm 2\omega_{z,0}\omega_e^d}. \tag{5.85}$$

Using $S_{\pm} \equiv \frac{\sin V_{\pm}t}{V_{\pm}}$, Eq. 5.83 becomes

$$U_{\pm} = \exp\left(-i\frac{H_{\pm}}{\hbar}t\right) \approx \exp\left(-\frac{1}{2}\frac{t}{\tau_0}\right)\begin{bmatrix} \exp\left(\mp i\frac{1}{2}(\omega_{z,0}\pm\omega_e^d)t\right) & -i\frac{1}{2}\omega_a'S_{\pm} \\ -i\frac{1}{2}\omega_a'S_{\pm} & \exp\left(\pm i\frac{1}{2}(\omega_{z,0}\pm\omega_e^d)t\right) \end{bmatrix}. \tag{5.86}$$

67

Thus $U_{-+}(2\tau) = U_-U_+$ is

$$U_{-+}(2\tau) = \exp\left(-\frac{\tau}{\tau_0}\right)\begin{bmatrix} e^{-i\omega_e^d\tau} - {\omega_a'}^2 S_-S_+ & -i\frac{1}{2}\omega_a' e^{i\frac{1}{2}\omega_{z,0}\tau}(S_+e^{-i\frac{1}{2}\omega_e^d\tau} + S_-e^{i\frac{1}{2}\omega_e^d\tau}) \\ -i\frac{1}{2}\omega_a' e^{-i\frac{1}{2}\omega_{z,0}\tau}(S_-e^{-i\frac{1}{2}\omega_e^d\tau} + S_+e^{i\frac{1}{2}\omega_e^d\tau}) & e^{i\omega_e^d\tau} - {\omega_a'}^2 S_-S_+ \end{bmatrix}$$

$$\approx \exp\left(-\frac{\tau}{\tau_0}\right)\begin{bmatrix} e^{-i\omega_e^d\tau} & be^{i\frac{1}{2}\omega_{z,0}\tau} \\ be^{-i\frac{1}{2}\omega_{z,0}\tau} & e^{i\omega_e^d\tau} \end{bmatrix} \approx \exp\left(-\frac{\tau}{\tau_0}\right)\begin{bmatrix} 1 - i\omega_e^d\tau & be^{i\frac{1}{2}\omega_{z,0}\tau} \\ be^{-i\frac{1}{2}\omega_{z,0}\tau} & 1 + i\omega_e^d\tau \end{bmatrix}$$

$$= \exp\left(-\frac{\tau}{\tau_0}\right)\left(\begin{bmatrix} 1 & 0 \\ 0 & 1 \end{bmatrix} + \begin{bmatrix} -i\omega_e^d\tau & be^{i\frac{1}{2}\omega_{z,0}\tau} \\ be^{-i\frac{1}{2}\omega_{z,0}\tau} & i\omega_e^d\tau \end{bmatrix}\right)$$

$$= \exp\left(-\frac{\tau}{\tau_0}\right)[\hat{I} + \vec{B}\cdot\vec{\sigma}], \tag{5.87}$$

where

$$b \equiv -i2\frac{\omega_a'}{\omega_{z,0}}\sin(\frac{1}{2}\omega_{z,0}\tau), \tag{5.88}$$

$$\vec{B}\cdot\vec{\sigma} = b\cos\frac{1}{2}\omega_{z,0}\tau\hat{\sigma}_x - b\sin\frac{1}{2}\omega_{z,0}\tau\hat{\sigma}_y - i\omega_e^d\tau\hat{\sigma}_z \tag{5.89}$$

$$B = \sqrt{b^2 + (\omega_e^d\tau)^2} \approx b \text{ and } \hat{\sigma}_B = \frac{\vec{\sigma}\cdot\vec{B}}{B} \approx \frac{\vec{\sigma}\cdot\vec{B}}{b} = \begin{bmatrix} -i\omega_e^d\tau/b & e^{i\frac{1}{2}\omega_{z,0}\tau} \\ e^{-i\frac{1}{2}\omega_{z,0}\tau} & i\omega_e^d\tau/b \end{bmatrix}. \tag{5.90}$$

Now

$$U_n = \exp\left(-\frac{n\tau}{\tau_0}\right)[\hat{I} + B\hat{\sigma}_B]^n \approx \exp\left(-\frac{n\tau}{\tau_0}\right)[\hat{I} + b\hat{\sigma}_B]^n$$

$$= \exp\left(-\frac{n\tau}{\tau_0}\right)(\hat{I}\frac{1}{2}[(1+b)^n + (1-b)^n] + \hat{\sigma}_B\frac{1}{2}[(1+b)^n - (1-b)^n])$$

$$= \frac{1}{2}\exp\left(-\frac{T}{2\tau_0}\right)\begin{bmatrix} F_+ - F_-i\omega_e^d\tau/b & F_-\exp\left(i\frac{1}{2}\omega_{z,0}\tau\right) \\ F_-\exp\left(-i\frac{1}{2}\omega_{z,0}\tau\right) & F_+ + F_-i\omega_e^d\tau/b \end{bmatrix}, \tag{5.91}$$

where

$$F_\pm \equiv \exp\left(-i\alpha\right) \pm \exp\left(i\alpha\right). \tag{5.92}$$

The cosine square-wave modulation is applied so that the total time-evolution operator becomes

$$U_{tot}(T) = U_n\exp\left(-i\frac{H_-}{\hbar}\frac{\tau}{2}\right)$$

$$\approx \frac{1}{2}\exp\left(-\frac{T}{2\tau_0}\right)\begin{bmatrix} F_+e^{(i\frac{1}{4}\omega_{z,0}\tau)} + F_-\frac{\omega_e^d e^{(i\frac{1}{4}\omega_{z,0}\tau)}}{\omega_a'\delta} & F_-e^{(i\frac{1}{4}\omega_{z,0}\tau)} \\ F_-e^{(-i\frac{1}{4}\omega_{z,0}\tau)} & F_+e^{(-i\frac{1}{4}\omega_{z,0}\tau)} - F_-\frac{\omega_e^d e^{(-i\frac{1}{4}\omega_{z,0}\tau)}}{\omega_a'\delta} \end{bmatrix}. \tag{5.93}$$

68

The final state is

$$\psi_\pm(T) = U_{tot}(T)\psi_\pm(0) = \frac{1}{2\sqrt{2}} \exp\left(-\frac{T}{2\tau_0}\right)((F_+ \pm F_-) \begin{bmatrix} \exp\left(i\frac{1}{4}\omega_{z,0}\tau\right) \\ \pm \exp\left(-i\frac{1}{4}\omega_{z,0}\tau\right) \end{bmatrix}$$

$$+ F_- \frac{\omega_e^d}{\omega_a'\delta} \begin{bmatrix} \exp\left(i\frac{1}{4}\omega_{z,0}\tau\right) \\ \mp \exp\left(-i\frac{1}{4}\omega_{z,0}\tau\right) \end{bmatrix}). \tag{5.94}$$

The expected value of σ_x is

$$\langle\sigma_x\rangle_\pm = \psi_\pm^\dagger \sigma_x \psi_\pm$$

$$= \frac{1}{8}\exp\left(-\frac{T}{\tau_0}\right)[(F_+ \pm F_-)^2(\pm 2\cos\frac{1}{2}\omega_{z,0}\tau)$$

$$+ (F_+ \pm F_-)^\star(F_- \frac{\omega_e^d}{\omega_a'\delta})(\pm 2i\sin\frac{1}{2}\omega_{z,0}\tau) + (F_+ \pm F_-)(F_- \frac{\omega_e^d}{\omega_a'\delta})^\star(\pm 2i\sin\frac{1}{2}\omega_{z,0}\tau)^\star]$$

$$= \pm e^{-\frac{T}{\tau_0}}[\cos(\frac{1}{2}\omega_{z,0}\tau)e^{\pm\gamma T} \pm \omega_e^d T\eta_\pm \sin\frac{1}{2}\omega_{z,0}\tau] \tag{5.95}$$

where

$$\eta_\pm \equiv \frac{\gamma(e^{\pm\gamma T} - \cos\Omega T) \pm \Omega\sin\Omega T}{(\Omega^2 + \gamma^2)T}. \tag{5.96}$$

Fig. 5.16 shows how $\eta_\pm$ and the coefficient of ω_e^d are affected by the pseudomagnetic field. The EDM signal will be diluted by the strong pseudomagnetic field. If the pseudomagnetic field becomes zero, i.e., $\Omega = 0$,

$$\eta_\pm = \frac{e^{\pm\gamma T} - 1}{\gamma T}. \tag{5.97}$$

The coefficient of ω_e^d becomes $e^{-\frac{T}{\tau_0}}\frac{(e^{\pm\gamma T}-1)}{\gamma}\sin\frac{1}{2}\omega_{z,0}\tau$ and the signal will linearly increase. The absorption rate for UCN in the state with $\sigma_x = \pm$ is

$$R_\pm = \frac{N_0(t)}{\tau_{abs}} = \frac{N_0(t)}{\tau_3}[1 - \vec{P}_n \cdot \vec{P}_3]$$

$$= \frac{N_0}{\tau_3}e^{-\frac{T}{\tau_0}}[e^{\pm\gamma T}(1 \mp P_3\cos\frac{1}{2}\omega_{z,0}\tau) + P_3\omega_e^d T\eta_\pm \sin\frac{1}{2}\omega_{z,0}\tau]. \tag{5.98}$$

The scintillation rate S for an initial UCN polarization P_n is

$$S = \frac{1}{2}(1 + P_n)R_+ + \frac{1}{2}(1 - P_n)R_-$$

$$= \frac{1}{2}\frac{N_0}{\tau_3}e^{-\frac{T}{\tau_0}}[(1 - P_3P_n\cos\frac{1}{2}\omega_{z,0}\tau)(e^{\gamma T} + e^{-\gamma T}) + (P_n - P_3\cos\frac{1}{2}\omega_{z,0}\tau)(e^{\gamma T} - e^{-\gamma T})$$

$$+ P_3\omega_e^d T\sin\frac{1}{2}\omega_{z,0}\tau(\eta_+ + \eta_- + P_n(\eta_+ - \eta_-))], \tag{5.99}$$

where

$$\eta_+ + \eta_- = \frac{\gamma(e^{\gamma T} + e^{-\gamma T} - 2\cos\Omega T)}{(\Omega^2 + \gamma^2)T} \approx \gamma T \tag{5.100}$$

$$\eta_+ - \eta_- = \frac{\gamma(e^{\gamma T} - e^{-\gamma T}) + 2\Omega\sin\Omega T}{(\Omega^2 + \gamma^2)T} \approx 2 \tag{5.101}$$

if $T \to 0$. It shows that the EDM signal will appear even if the polarization is zero, i.e., $P_n = 0$, because the spin-dependent neutron capture makes the neutron polarized during the measurement. The ω_e^d term is proportional to $\gamma T^2 + 2P_n T$. Ignoring T^2 term, the EDM signal, the ω_e^d term of the scintillation light rate, becomes

$$S_{edm} = \frac{N_0}{\tau_3} e^{-\frac{T}{\tau_0}} P_3 P_n \sin\frac{1}{2}\omega_{z,0}\tau \cdot \omega_e^d T. \tag{5.102}$$

In the next section, we will show how to use it as the input for the feedback loop and as the monitor of the linearly increasing signal in the other cell.
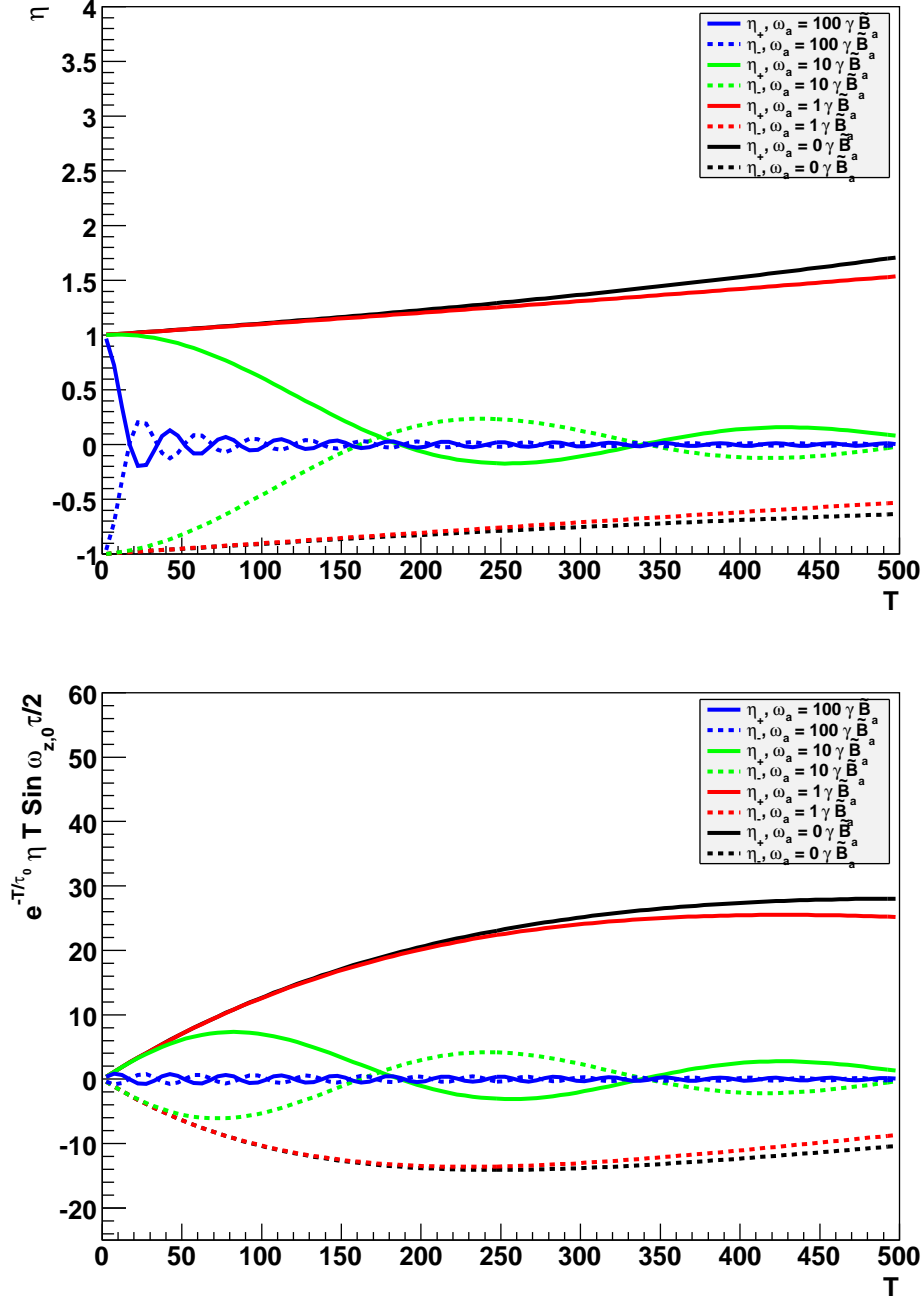
Figure 5.16: $\eta_{\pm}$ and $e^{-\frac{T}{\tau_0}} \eta_{\pm} T \sin \frac{1}{2} \omega_{z,0} \tau$. $P_3 = 1$, $\omega_a = a\gamma\tilde{B}_a$, where $a = 0, 1, 10, 100$ and $\tau_3 = 500 \; sec$ and $\omega_{z,0} = 2\pi \times 0.1 \; Hz$, $\tau_m = 1 \; sec$ so that $\frac{\sin(\frac{1}{2}\omega_{z,0}\tau)}{\frac{1}{2}\omega_{z,0}\tau} = 0.996$.

5.7 Feedback method

The idea of the feedback loop is to keep the linearly increasing term in Eq. 5.99, i.e., Eq. 5.102, zero by adjusting the dressing parameters. If a system is at the critical dressing, the relative angle between neutron and ^{3}He will be varied equally by the modulation, i.e., $|\omega_{z,0}^+| = |\omega_{z,0}^-|$. However, if $|\omega_{z,0}^+| \neq |\omega_{z,0}^-|$, the variation won't be the same in different modulation directions. The difference will be used as the input to the feedback loop. The modulation cycle will be repeated with the modified dressing field. After one more cycle, the new angular difference will be used as a new input. The cycle will be repeated until the system becomes stable. For a real experiment, it is not easy to measure the relative angle directly. What we can measure is the number of events (scintillation lights) detected in each half cycle. The details will be simulated in Sec. 5.7.3.

By measuring the dressing parameters as a function of the electric field, the neutron EDM can be determined. Since the applied field $\vec{E}$ determines the relative angle, the UCN-^{3}He system is mathematically equivalent to a voltage-controlled oscillator of a phase-locked-loop(PLL), which can be referred in [27], with the first harmonic signal equivalent to the voltage output of the PLL phase detector. The PLL technique can be applied to the neutron EDM search [29].

One point should be emphasized for the two-cell system. Since the two cells share the same dressing coils but have different electric field directions, the dressing field for both cells will be modified at the same time so that only one cell will be kept at the critical dressing. The signal in another cell will have the increasing term as Eq. 5.102, which is proportional to $2\omega_e^d$. Here we apply the feedback to cell 1 and use cell 2 as a monitor.

5.7.1 Systematic uncertainties in the feedback system

The linearly increasing term in Eq. 5.99 and Eq. 5.102 is proportional to the EDM effective field, ω_e^d. Theoretically, the measurement of the linearly increasing signal, like Fig. 5.16, should be enough to determine the EDM value. However, there are two dominant systematic errors affecting the final result. First, the pseudomagnetic field will change the slope of the increasing signal or even dilute the signal as shown in Fig. 5.16. The angle between neutron and ^{3}He cannot be controlled better than 10^{-3} rad. If the pseudomagnetic field has a component along $\hat{z}$ at an order of 0.1%, the frequency shift will be at the level of 10^{-6} Hz which is at the level of $10^{-26}e$ cm [8]. Second, the offset of the dressing field will create a frequency shift between two particles which is described in Eq. 5.43 and Sec. 5.5. However, it is independent of the electric field direction and should be able to be cured by the feedback. Here we focus on the discussion of the pseudomagnetic field.

In the ideal situation, the applied correcting field ω_c should be able to cancel ω_e^d so that $\omega_z \equiv \omega_e^d - \omega_c$

---

[8]In Sec. 5.2, the pseudomagnetic field is around $B_a \sim 5 \times 10^{-5}$ mG so that the possible frequency shift due to the vertical component of B_a is $\Delta\omega = \gamma B_a \times 10^{-3} \sim 1$ μHz.

becomes zero and $\omega_c = \omega_e^d$ is the EDM signal. However, the pseudomagnetic field and the offset of dressing field will bias the measurement. How can one estimate the systematic error? First, let us consider a system of the critical dressing in the ^{3}He rotating frame (the frame rotates at $\omega_3^d = \gamma_3 B_0 J_0(ax_c)$ around $\hat{z}$). The pseudomagnetic field B_a is along $\hat{x}$ and initially the residual field along the $\hat{z}$-axis is the EDM effective field B_e. The corresponding frequency is $\omega_a = \gamma_n B_a$ and $\omega_e^d = \gamma_n B_e J_0(x_c)$. ω_n' is the effective frequency of the neutron in the rotating frame and ψ_n is the angle between the direction of the total B field, $\vec{B}_{tot} = B_a \hat{x} + B_e J_0(x_c)\hat{z}$, and $\hat{x}$-axis so that

$$\omega_n' = \sqrt{\omega_a^2 + (\omega_e^d)^2} \approx \omega_a \quad \text{and} \quad \tan \psi_n = \frac{\omega_e^d}{\omega_a}. \tag{5.103}$$

A new coordinate can be defined such that

$$
\begin{bmatrix} \hat{x}' \\ \hat{y}' \\ \hat{z}' \end{bmatrix} =
\begin{bmatrix} \cos \psi_n & 0 & \sin \psi_n \\ 0 & 1 & 0 \\ -\sin \psi_n & 0 & \cos \psi_n \end{bmatrix}
\begin{bmatrix} \hat{x} \\ \hat{y} \\ \hat{z} \end{bmatrix}. \tag{5.104}
$$

The spin orientation of the neutron is initially along the $\hat{x}$-axis and

$$\vec{S}(t=0) = \vec{S}_\parallel(t=0) + \vec{S}_\perp(t=0), \tag{5.105}$$

where $\vec{S}_\parallel(t)$ is along $\vec{B}_{tot}$ and independent of time,

$$\vec{S}_\parallel(t=0) = |\vec{S}|\cos \psi_n \hat{x}' \quad \text{and} \quad \vec{S}_\perp(t=0) = -|\vec{S}|\sin \psi_n \hat{z}' \tag{5.106}$$

where we set $|\vec{S}| = 1$ for convenience. $\vec{S}_\perp$ will rotate along $\vec{B}_{tot}$ so that

$$\vec{S}_\perp(t) = (-|\vec{S}|\sin \psi_n)(\cos (\omega_n' t)\hat{z}' - \sin (\omega_n' t)\hat{y}') \tag{5.107}$$

The total spin is

$$
\begin{aligned}
\vec{S}(t) = \vec{S}_\parallel(t) + \vec{S}_\perp(t) &= |\vec{S}|\cos \psi_n \hat{x}' - (|\vec{S}|\sin \psi_n)(\cos (\omega_n' t)\hat{z}' - \sin (\omega_n' t)\hat{y}') \\
&= |\vec{S}|\cos \psi_n(\cos \psi_n \hat{x} + \sin \psi_n \hat{z}) - (|\vec{S}|\sin \psi_n)(\cos (\omega_n' t)(-\sin \psi_n \hat{x} + \cos \psi_n \hat{z}) - \sin (\omega_n' t)\hat{y}) \\
&= |\vec{S}|[(\cos^2 \psi_n + \sin^2 \psi_n \cos \omega_n' t)\hat{x} + \sin \psi_n \sin \omega_n' t\hat{y} + (\sin \psi_n \cos \psi_n(1 - \cos \omega_n' t)\hat{z}].
\end{aligned} \tag{5.108}
$$

For a duration τ_L (the loop response time), the spin projection along the $\hat{z}$-axis is

$$S_z = \vec{S}(\tau_L) \cdot \hat{z} = |\vec{S}|(\sin \psi_n \cos \psi_n(1 - \cos \omega_n' \tau_L)) \approx 1 \cdot \frac{\omega_e^d}{\omega_n'}\frac{\omega_a}{\omega_n'}(1 - (1 - \frac{(\omega_n' \tau_L)^2}{2})) = \frac{1}{2}\omega_e^d \omega_a \tau_L^2, \tag{5.109}$$

which is Eq. 5.37 in [29]. The $\hat{y}$ projection of $\vec{S}(\tau_L)$ is

$$S_y = \vec{S}(\tau_L) \cdot \hat{y} = |\vec{S}|(\sin\psi_n \sin\omega'_n\tau_L) \approx 1 \cdot \frac{\omega_e^d}{\omega'_n}(\omega'_n\tau_L) = \omega_e^d\tau_L. \tag{5.110}$$

For the feedback loop system in an equilibrium state, the initial situation $\omega_z = \omega_e^d$ would become $\omega_z = \omega_e^d - \omega_c$ where ω_z is the residual field, i.e., the EDM effective field minus the correction field, along $\hat{z}$ The final spin will lie along the net field

$$\vec{S} \parallel \omega_a\hat{x} + \omega_z\hat{z} \tag{5.111}$$

so that

$$S_z \approx |\vec{S}|\frac{\omega_z}{\omega_a} = \frac{1}{2}\omega_e^d\omega_a\tau_L^2, \quad \text{and} \quad \omega_z = \frac{1}{2}\omega_e^d\omega_a^2\tau_L^2. \tag{5.112}$$

The EDM signal $\omega_c = \omega_e^d(1 - \frac{1}{2}\omega_a^2\tau_L^2)$ will have an error $\delta\omega_c = \frac{1}{2}\omega_e^d\omega_a^2\tau_L^2$. It represents an error in the feedback signal due to the pseudomagnetic field. However, it is very small. If $\omega_e^d \sim 10^{-6}$ Hz, $\omega_a \sim 10^{-3}$ Hz and $\tau_L \sim 10$ sec, then $\delta\omega_c \approx 10^{-10}$ Hz which can be ignored in the measurement. On the other hand, if the pseudomagnetic field has a vertical component at order of 10^{-3} rad, it will directly make a frequency shift $10^{-3}\omega_a$. Fortunately, it is independent of the electric field direction. A possible solution is to compare signals between two runs with different electric field directions.

5.7.2 Density matrix simulation of the feedback system

It won't be easy to analytically solve the feedback loop. A better method is to simulate the feedback loop. One quick method is to apply the time-evolution operator discussed in Sec. 5.6.2. Instead of using the calculation in Sec. 5.6.2, however, the simulation can be simplified by using the secular approximation method which is mentioned in Sec.5.3 of [29]. The density matrix $\rho(t)$ can be numerically calculated by using the time-evolution operator $U(t) = \exp(-i\frac{\langle H \rangle}{\hbar}t)$, where $\langle H \rangle$ is the time average of the Hamiltonian(the secular approximation). The density matrix at $t = 0$ is

$$\rho(0) = \begin{bmatrix} \frac{1}{2}(1 + P_n) & 0 \\ 0 & \frac{1}{2}(1 - P_n) \end{bmatrix}. \tag{5.113}$$

The time dependence of the density matrix is

$$\rho(t) = U^\dagger(t)\rho(0)U(t). \tag{5.114}$$

The "secular approximation" will be applied to get [9]

$$\left\langle \vec{S}_n \cdot \vec{S}_3 \right\rangle = \langle \cos \theta_{n3} \rangle \tag{5.115}$$

and then Eq. 5.78 becomes

$$\langle H \rangle_{\pm} = -\frac{\hbar}{2} i [\frac{1}{\tau_0} - \frac{P_3}{\tau_3} \langle \cos \theta_{n3} \rangle \hat{\sigma}_x] + \frac{1}{2}\omega_a \hbar \langle \cos \theta_{n3} \rangle \hat{\sigma}_x \pm \frac{1}{2}\omega_{z,0}\hbar\hat{\sigma}_z + \frac{1}{2}\omega_z\hbar\hat{\sigma}_z, \tag{5.116}$$

where $\omega_{z,0}$ is defined in Eq. 5.73 , $\omega_z \equiv \omega_e^d - \omega_c$ and ω_c is the correction field. Using the secular approximation, the only important factor is the average value of $\cos \theta_{n3}$. Thus we can use any type of modulation, like sinusoidal, square wave, etc.

A feedback loop is designed as follow:

- Initially, $\omega_c = \omega_c^0 = 0$.

- $\omega_z = \omega_e^d - \omega_c$. The ω_z is equal to the difference between ω_e^d and ω_c.

- $\rho(t+\tau) = U_+^\dagger(\tau)\rho(t)U_+(\tau)$. Use the new ω_z to rotate spin of neutron in positive modulation direction.

- $\langle s_x \rangle_+ = Tr[\rho(t+\tau)\sigma_x]$. Get the spin projection in $\hat{x}$-axis.

- $\rho(t+2\tau) = U_-^\dagger(\tau)\rho(t+\tau)U_-(\tau)$. Use the new ω_z to rotate spin of neutron in negative modulation direction.

- $\langle s_x \rangle_- = Tr[\rho(t+2\tau)\sigma_x]$. Get the spin projection in $\hat{x}$-axis.

- $\theta(t) = \langle s_x \rangle_+ - \langle s_x \rangle_-$. The difference between these two spin projections will be used as the feedback input.

- $\omega_c^\alpha = \omega_c^0 + \alpha(\langle s_x \rangle_+ - \langle s_x \rangle_-)$. The α term is the integrated feedback for the whole measurement.

- $\omega_c^\beta = \beta(\langle s_x \rangle_+ - \langle s_x \rangle_-)$. The β term is the instantaneous feedback based on a single cycle.

- $\omega_c = \omega_c^\alpha + \omega_c^\beta$. Two terms should be considered together. The optimal values of α and β should be determined by simulation.

- $\omega_c^0 = \omega_c^\alpha$. Reset the value of ω_c^0, the integrated value of ω_c.

- $\omega_z = \omega_e^d - \omega_c$. The new value of ω_z.

- Continue the loop.

---

[9] $\vec{S}$ means the polarization direction of particle, not spin operator.

To calculate the time-evolution operator $U(t)$, we define four terms corresponding to the various terms in Eq. 5.116

$$U_1(t) = \exp\left[-i(-i\frac{1}{2\tau_0})t\right] = \hat{I}\exp\left[-\frac{t}{2\tau_0}\right],$$

$$U_2(t) = \exp\left[-i(i\frac{P_3}{2\tau_3}\langle\cos\theta_{n3}\rangle)\hat{\sigma}_x t\right] = \hat{I}\cosh\left[\frac{P_3}{2\tau_3}\langle\cos\theta_{n3}\rangle t\right] + \hat{\sigma}_x\sinh\left[\frac{P_3}{2\tau_3}\langle\cos\theta_{n3}\rangle t\right],$$

$$U_3(t) = \exp\left[-i(\frac{1}{2}\omega_a\langle\cos\theta_{n3}\rangle)\hat{\sigma}_x t\right] = \hat{I}\cos\left[\frac{1}{2}\omega_a\langle\cos\theta_{n3}\rangle t\right] - i\hat{\sigma}_x\sin\left[\frac{1}{2}\omega_a\langle\cos\theta_{n3}\rangle t\right],$$

$$U_{4\pm}(t) = \exp\left[-i\frac{1}{2}(\pm\omega_{z,0}+\omega_z)\hat{\sigma}_z t\right] = \hat{I}\cos\left[\frac{1}{2}(\omega_{z,0}\pm\omega_z)t\right] \mp i\hat{\sigma}_z\sin\left[\frac{1}{2}(\omega_{z,0}\pm\omega_z)t\right] \tag{5.117}$$

$$U_\pm(t) = U_1(t)U_2(t)U_3(t)U_{4\pm}(t) \tag{5.118}$$

where the σ_i are

$$\sigma_x = \begin{bmatrix} 1 & 0 \\ 0 & -1 \end{bmatrix}, \sigma_y = \begin{bmatrix} 0 & 1 \\ 1 & 0 \end{bmatrix}, \sigma_z = \begin{bmatrix} 0 & -i \\ i & 0 \end{bmatrix}. \tag{5.119}$$

following the definition of Eq. 5.113.

The practical value of parameters are

- $\omega_{z,0} = 0.5\pi$ Hz, corresponding to the modulation amplitude.

- $\tau = \frac{1}{2}\tau_m = 0.5$ sec, one-half of the modulation period.

- $\langle\cos\theta_{n3}\rangle = \frac{\sin\frac{1}{2}\omega_{z,0}\tau}{\frac{1}{2}\omega_{z,0}\tau} \approx 0.974495$.

- $\omega_e^d = \gamma_n\tilde{B}_e J_0(x_c) \approx 1$ μHz, the EDM effective precession frequency.

- $\omega_a = \gamma\tilde{B}_a \approx 2$ mHz, corresponding to the pseudomagnetic field.

- $\tau_3 = 500$ sec, the absorption decay time.

- $P_3 = P_n = 1$, the polarization of ^{3}He and neutron.

The following study will depend on those parameters. The method is efficient for studying the effect of each parameter.

One should pay attention to those parameters, like ω_a, which are difficult to control. First, we consider the system without decay, i.e., $U_1 = U_2 = 1$. Fig. 5.17 shows one example of the feedback loop. Several points should be emphasized. First, ω_z will be eventually close to zero as expected. The nonzero final $\omega_z \sim 2.02 \times 10^{-7}$ reflects the effect of pseudomagnetic field discussed earlier. Second, S_x approaches a different constant from one. The polarization $\vec{S}$ is rotating about an axis having $\hat{x}$ and $\hat{z}$ components.

Using Eq. 5.111, the ratio of two spin components and two effective fields are

$$\frac{S_z}{S_x} = \frac{0.000135025}{0.923866689} = 1.46152 \times 10^{-4} \tag{5.120}$$

$$\frac{\omega_z}{\omega_a} = \frac{2.0229345 \times 10^{-7}}{0.002} = 10^{-4} \tag{5.121}$$

showing the polarization is (roughly) along the axis $\omega_a \hat{x} + \omega_z \hat{z}$. For the pseudomagnetic field, Fig. 5.18 shows the effect is at the level of $3 \times 10^{-7} \ Hz$. Using Eq. 5.112 we have $S_z = \frac{1}{2}\omega_e^d \omega_a \tau_L^2 = 0.000135025$, $\tau_L \sim 367 \ sec$. Therefore, $\omega_z = \frac{1}{2}\omega_e^d \omega_a^2 \tau_L^2 = 2.7 \times 10^{-7}$ which is consistent with the simulation result of ω_z. The analytical expression is just an approximation. This would explain the small difference between the expression and simulation. When the decay is considered, i.e., $U_1 \neq 1, U_2 \neq 1$, Fig. 5.19 shows the feedback loop can still work.
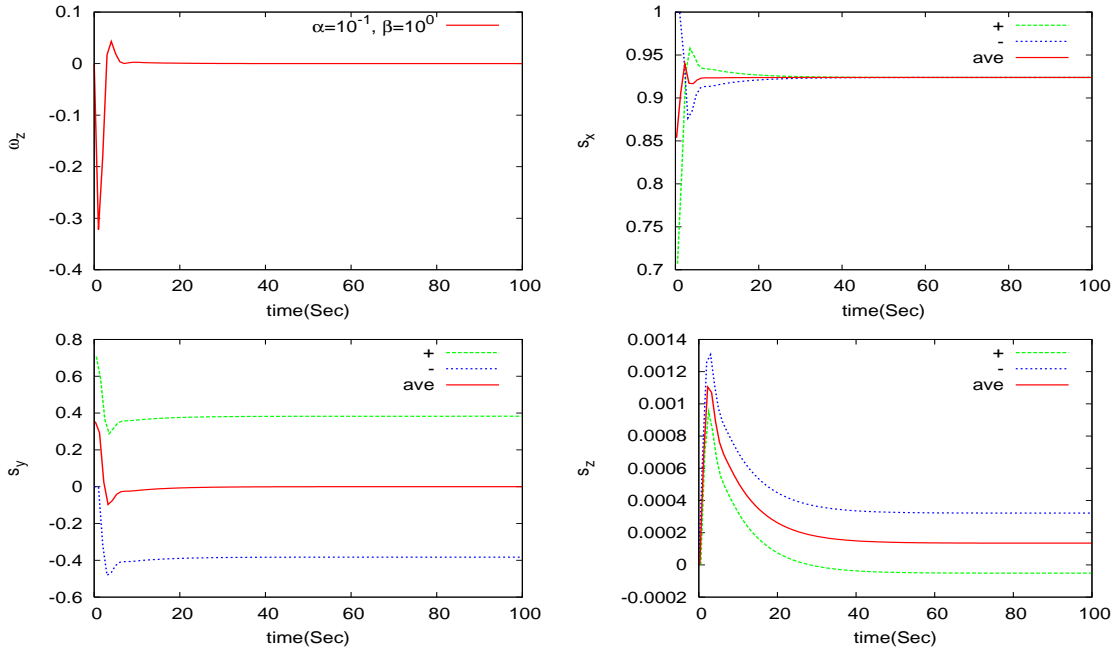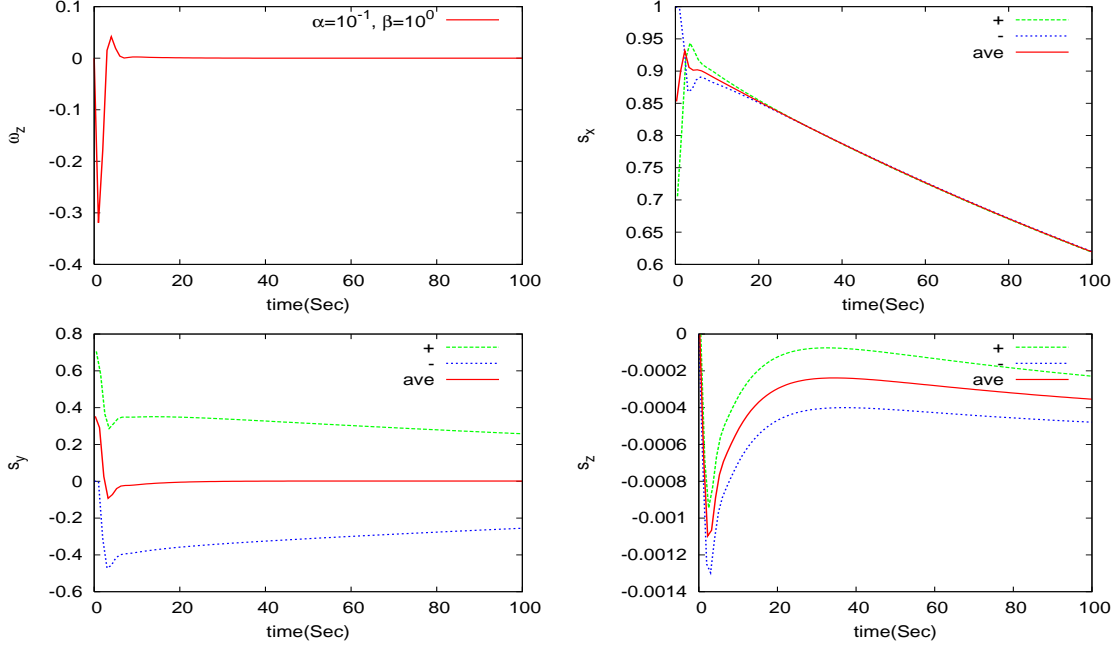

Figure 5.17: $\vec{S}$ and ω_z. $U_1 = U_2 = 1$. $\omega_e^d = 1 \ \mu Hz$ and $\omega_a = 2 \ mHz$, $\alpha = 0.1$, and $\beta = 1$. $\tau_m = 1 \ sec$ and $\omega_{z,0} = 0.5\pi \ Hz$.

In [29], the dressed spin technique with the feedback method is demonstrated to be comparable with the free case(the SQUID method) [10]. However, the model assumes neutron and ^{3}He both precessing at the horizontal plane, and also assumes the symmetry between the two sides of the critical point. In reality, Bloch equation simulation shows the precession is not at the horizontal plane. Even at the critical dressing, neutron and ^{3}He cannot precess exactly together. The pseudomagnetic field could affect the final result. Besides, the decay and the absorption of the neutron will change the input signal of the feedback loop. All of these issues will be discussed in the next two sections.

[10]The details of the sensitivity calculation can be referred in Appendix H.
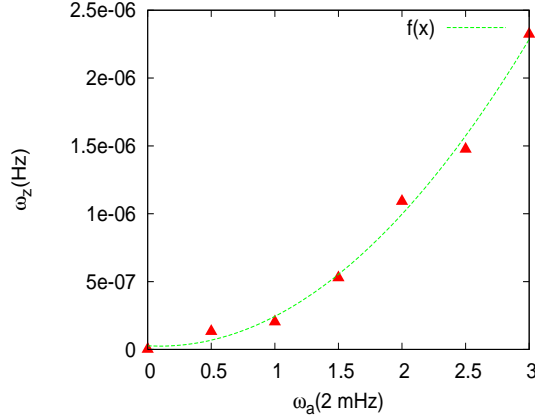
Figure 5.18: ω_z versus ω_a. $f(x) = 2.6792 \times 10^{-7} x^2 - 5.08636 \times 10^{-8} x - 2.68027 \times 10^{-8}$. The pseudomagnetic field effect is at level of $10^{-7} \, Hz$ which is smaller than $\omega_e^d = 10^{-6} \, Hz$.

5.7.3 Monte Carlo simulation of the feedback system

The Monte Carlo of the scintillation light signals were generated, called Φ, to simulate the real experiment. The collection of the scintillation light in the first half and the second half of a modulation cycle are $\Phi_{+,i}$ and $\Phi_{-,i}$. The difference, $\Delta\Phi_i = \Phi_{+,i} - \Phi_{-,i}$, will be used as an input to the feedback loop for a real experiment. The feedback loop will enable $\Delta\Phi_i \to 0$ by modifying the dressing field. The detailed procedure for the simulation is the following:

1. The initial value of B_d is $B_{d,0}$.

2. For a given $B_{d,i}$, the Bloch equation is used to calculate $\cos\theta_{n3}$ within a modulation cycle, $t = [t_i, t_i + \tau_m]$.

3. $\cos\theta_{n3}$ is inserted into Eq. 5.30, $\frac{d\Phi}{dt}$.

4. The collection of the scintillation light is calculated:

$$\Phi_{+,i} = \int_{t_i}^{t_i+\tau_m/2} \frac{d\Phi}{dt} dt,$$
$$\Phi_{-,i} = \int_{t_i+\tau_m/2}^{t_i+\tau_m} \frac{d\Phi}{dt} dt, \tag{5.122}$$

5. Monte Carlo is generated with a randomization using Poisson statistics [11], i.e., $N_{+,i} = Poisson(\Phi_{+,i})$ and $N_{-,i} = Poisson(\Phi_{-,i})$

---

[11] If the expected number of occurrences in this interval is λ, then the probability that there are exactly κ occurrences (κ being a non-negative integer, $\kappa = 0, 1, 2, ...$) is equal to

$$f(\kappa, \lambda) = \frac{\lambda^\kappa e^\lambda}{\kappa!}. \tag{5.123}$$

Figure 5.19: $\vec{S}$ and ω_z. $U_1 \neq 1$ and $U_2 \neq 1$. $\omega_e^d = 1 \ \mu Hz$ and $\omega_a = 2 \ mHz$, $\alpha = 0.1$, and $\beta = 1$. $\tau_m = 1 \ sec$ and $\omega_{z,0} = 0.5\pi \ Hz$.

6. The difference is calculated: $\Delta N_i = N_{+,i} - N_{-,i}$.

7. The feedback loop process is run and a modified dressing field is obtained.

   - Low Pass Integrator: $B_{c,0,\alpha} = B_{d,0}$, $B_{c,i,\alpha} = B_{c,i-1,\alpha} - \alpha \Delta N_i$.

   - Amplifier: $B_{c,i,\beta} = -\beta \times \Delta N_i$.

   - Modified field: $B_{d,i+1} = B_{c,i,\alpha} + B_{c,i,\beta}$.

8. Go to 2 and repeat the loop.

The Bloch equation simulation uses the following parameters. The time step is $\Delta t = 10^{-6} \ sec$. The dressing parameters are $y = 0.01$ and $x = 1.189$. The holding field is $B_0 = 10 \ mG$. The modulation field is set at $B_m = \epsilon B_{d,0}$, where $\epsilon = 0.05$ is the modulation ratio. The modulation period is $\tau_m = 1 \ sec$ like Fig. 5.11, where $\theta_{MAX} \approx 0.5 \ rad$. The feedback loop parameters are named α and β. α is for the integrated effect of the whole measurement period, while β is for a single modulation cycle. It is necessary to have both terms. They can balance the fast and slow response of the feedback loop.

It is difficult to analytically optimize the feedback loop parameters. We have empirically tried several conditions of different modulation field magnitude B_m and frequency f_m. $\tau_m = 1/f_m$ should be kept much smaller than the decay constant in order to reduce the decay effect. Larger B_m may cause a larger offset. Ref. [29] assumes a slow decay constant for the loop. If the modulation period is too long, then the decay would bias the feedback loop final values. However, if it is too short, the loop may not work either due to

small statistics. It is not easy to balance these two situations. The proper α and β are also chosen so that they can give the most stable $\cos\theta_{n3}$. The average value of $\cos\theta_{n3}$ is $\frac{\sin\frac{1}{2}\omega_{z,0}\tau}{\frac{1}{2}\omega_{z,0}\tau}$ where $\omega_{z,0}$ is given in Eq. 5.73 and $\tau = \frac{1}{2}\tau_m$. Thus, the value of $\cos\theta_{n3}$ also depends on B_m and f_m.

As an example, we show the results are otained with parameters $B_m/B_{d,0} = 0.05$, $f_m = 0.5\ Hz$, $\alpha = 5 \times 10^{-6}$, and $\beta = 5 \times 10^{-4}$. Fig. 5.20 shows the modified dressing field with (black curves) and without (red curves) fluctuation, i.e., the randomization using Poisson distribution in Step (5). The left figure of Fig. 5.20 shows the pattern if the initial B_d is set at 1189 mG for run 0 and the right figure is the pattern of run 1 if its initial B_d is the final value of run 1. Fig. 5.21 shows $\cos\theta_{n3}$ of cell 1 and cell 2 for run 1. $\cos\theta_{n3}$ of cell 1 can be largely kept at a constant while $\cos\theta_{n3}$ of cell 2 will linearly increase. Fig. 5.22 shows the time spectrum of scintillation light signals for cell 1 and cell 2. The signal for cell 1 is kept at the critical dressing and for cell 2, the linearly increasing first harmonic signal is observed. Fig. 5.23 shows the signal difference between two cells, which should be compared with Fig. 5.16. Fig. 5.24 shows another example of the signal difference between two cells.
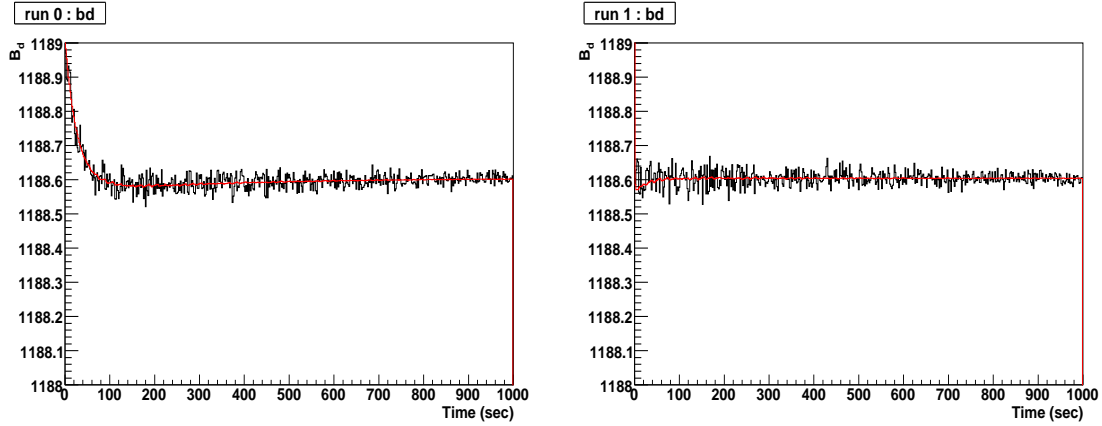
Figure 5.20: B_d as a function of time for the first run (run 1) and the successive run (run2).
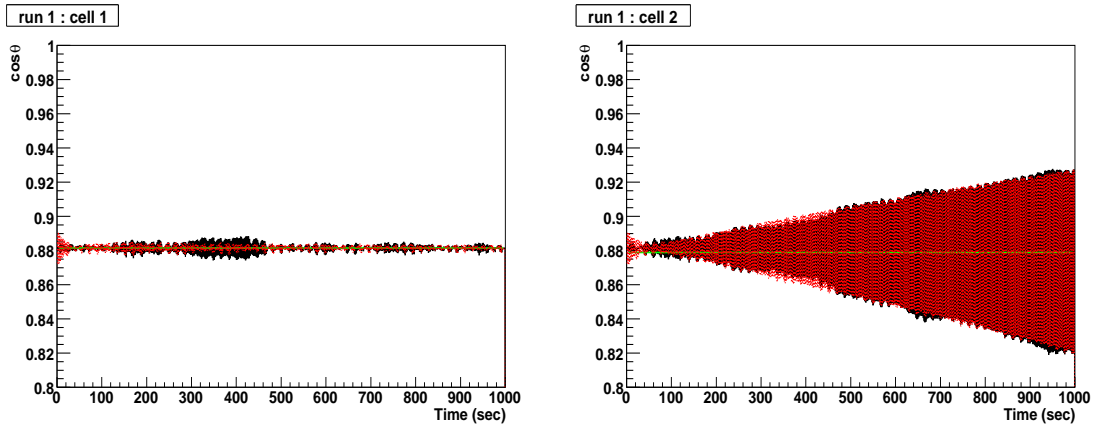
Figure 5.21: $\cos\theta_{n3}$ as a function of time for cell 1 and cell 2. $\cos\theta_{n3}$ for cell 1 can be kept at a constant by the feedback. $\cos\theta_{n3}$ for cell 2 is linearly increasing.
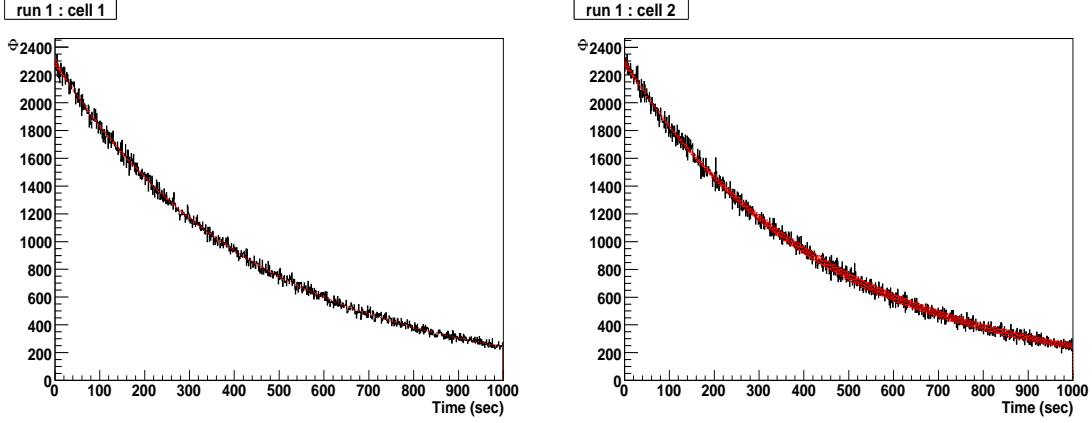
Figure 5.22: The time spectrum of scintillation light signals for cell 1 and cell 2.
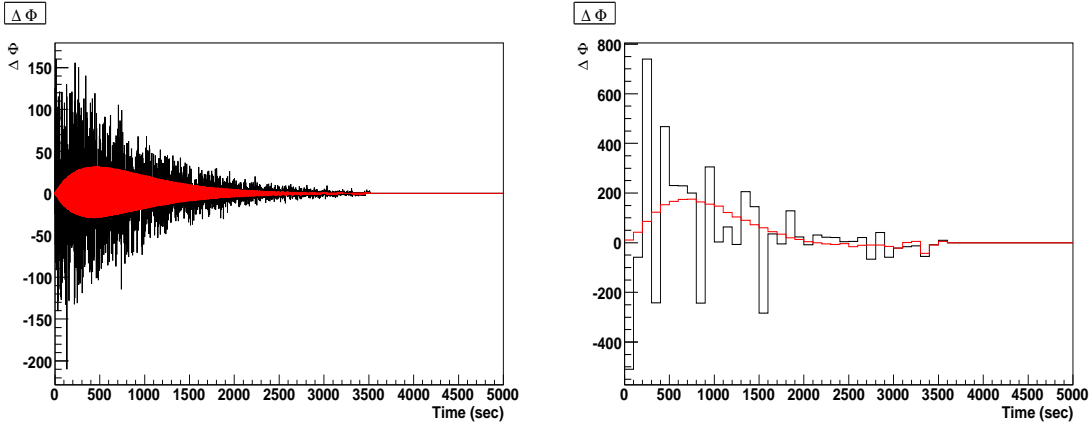

Figure 5.23: The time spectrum difference between cell 1 and cell 2. The right plot is the rebinned histogram of the left plot (100 bins), showing linearly increasing pattern is not clear.

5.7.4   Extraction of the neutron EDM in the feedback system

If the feedback loop works, the modified dressing field should be able to keep the system at the critical dressing so that the correction field can compensate the frequency shift due to a nonzero neutron EDM. Therefore, by measuring the change of the modified dressing field, the neutron EDM can be determined. We consider a frequency shift $\Delta\omega_\gamma$ due to the correction field which causes a shift $\Delta x = \gamma_n B_c/\omega_d$:

$$\Delta\omega_\gamma = \omega_0[J_0(x_c + \Delta x) - \gamma_3/\gamma_n J_0(\gamma_3/\gamma_n(x_c + \Delta x))]$$

$$\approx \omega_0\Delta x[-J_1(x_c) + (\gamma_3/\gamma_n)^2 J_1(\gamma_3/\gamma_n x_c)] = 0.156077\omega_n\Delta x. \tag{5.124}$$

81
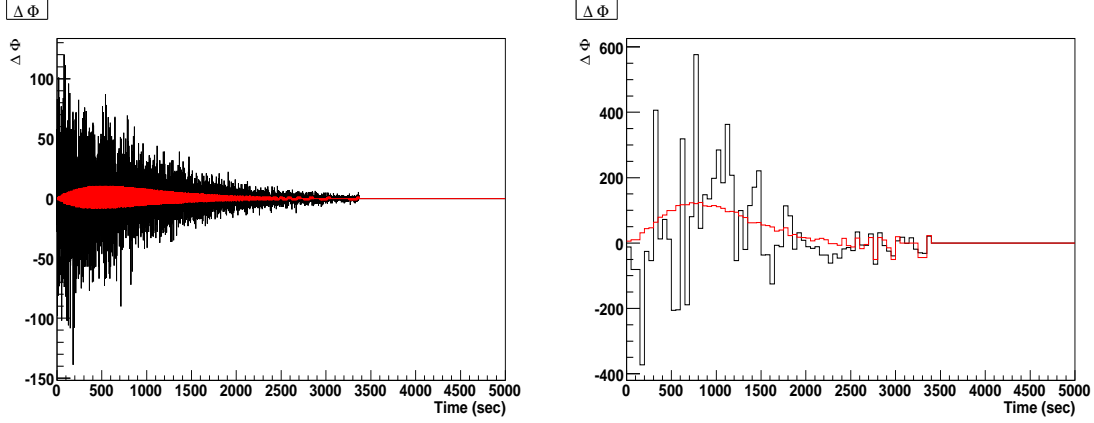
Figure 5.24: $B_m/B_{d,0} = 0.05$, $f_m = 1\ Hz$ and $\alpha = 10^{-5}$, $\beta = 10^{-3}$. The time spectrum difference between cell 1 and cell 2. The right plot is the rebinned histogram of the left plot (100 bins), showing linearly increasing pattern.

When the correction field cancels out the EDM effective frequency shift ω_e^d,

$$\Delta\omega_\gamma \sim \omega_e^d = 0.156077\omega_n \frac{\gamma_n B_c}{\omega_d} = -0.0286007 B_c \qquad (5.125)$$

so that we can get the relation

$$B_c = -34.9642\omega_e^d \qquad (5.126)$$

where the unit of B_c is mG and the unit of ω_e^d is Hz.

Except for the first run, the final stable $B_{d,f}$ can be obtained by fitting the $B_d(t)$ time spectrum within $t = [0 - 1000]\ sec$. To study the sensitivity, 90 runs for each cells were generated. The fitted $B_c = B_{d,f} - B_{d,0}$ is shown in Fig. 5.25. The mean of 90 runs for $\omega_e = 100\mu Hz$ is $-0.396\ mG$ and for $\omega_e = -100\mu Hz$ is $-0.401\ mG$ and the standard deviation is around $\sigma_{B_c} \approx 2.49 \times 10^{-4}\ mG$. The difference $\Delta\bar{B}_c = 5.0 \times 10^{-3}\ mG$ corresponds to $\Delta\omega_e = 5.0 \times 10^{-3}/(34.9642 \times J_0(1.189)) = 211.4\ \mu Hz$ which is consistent with the input. The standard deviation of f_d, which is related to ω_e^d, is

$$\sigma_{f_d} = \frac{\sigma_{\omega_e^d}}{2\pi J_0(1.189)} = \frac{1}{34.9642 \times 2\pi J_0(1.189)}\sigma_{B_c} = 1.68 \times 10^{-6}\ Hz. \qquad (5.127)$$

For $t = [0, 500]\ sec$, $\sigma_{f_d} = 2.77 \times 10^{-6}\ Hz$.

5.7.5   Systematic uncertainties in the feedback system using Monte Carlo simulation

We have shown that the statistical accuracy for the feedback method is comparable to that of the SQUID method. The systematic uncertainties should also be carefully studied. Several initial parameters have been varied for different studies. The fluctuation of holding field is one of the dominant errors the dressed
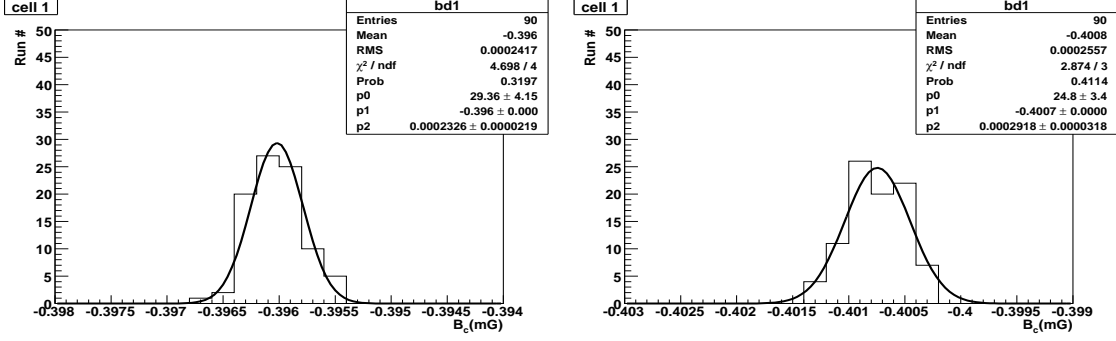
82

Figure 5.25: The correction field $B_c = B_{d,f} - B_{d,0}$ for $\omega_e = 100\mu Hz$ (left) and $\omega_e = -100\mu Hz$ (right). The mean difference is $\Delta B_c = 4.74 \times 10^{-3}$ mG. The standard deviation σ_{B_c} is 2.49×10^{-4} mG.

spin technique is designed to suppress. We assume that the holding field B_0 has a Gaussian distribution and the mean value is mG with a width of ΔB_0. B_0 value is randomized for each run. To see the effect from the fluctuation of the holding field, the same random seed is applied to each run. Correction field versus ΔB_0 is shown in Fig. 5.26. It shows that the dressed spin technique is not sensitive to the holding field drift as well as the analytic prediction in Appendix F, showing the deviation in the correction field is about 1 % due to the drift of the holding field. Correction field versus the variation of neutron density is shown in Fig. 5.27 without and with the fluctuation. The simulation shows that the effect is about 1×10^{-5}, 10% of the statistical sensitivity. Correction fields versus the magnitude of pseudomagnetic field is shown in Fig. 5.28 without and with the statistical fluctuation. The simulation shows that the effect is proportional to B_a^2 in agreement with the exepctation [29]. If there is a nonzero initially relative angle between neutron and ^{3}He in the $\hat{x} - \hat{y}$ plane, called ϕ, Fig. 5.29 shows the effect for different pseudomagnetic fields. If there is an initially relative angle between neutron and ^{3}He along $\hat{z}$ axis, called θ, Fig. 5.30 shows the effect for different pseudomagnetic fields. The systematic error caused by nonzero θ is larger than that of nonzero ϕ. It is clear that additional study of systematic uncertainties is required before the final design of the nEDM dressed-spin system.
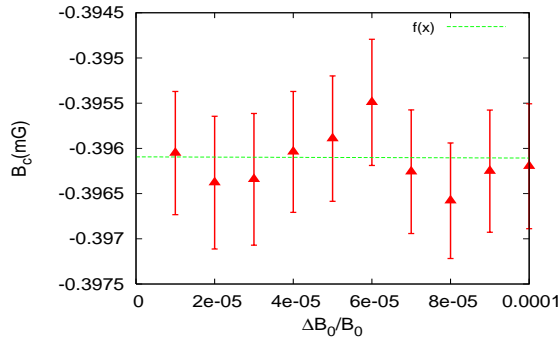

Figure 5.26: The correction field $B_c = B_{d,f} - B_{d,0}$ versus fluctuation of B_0.
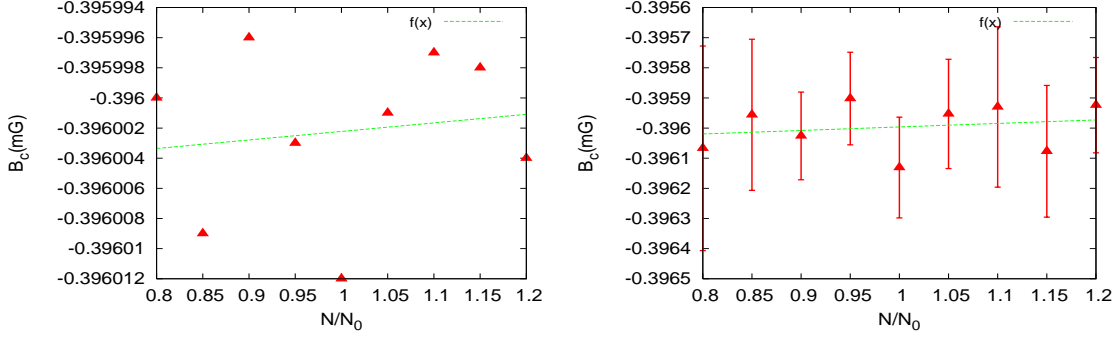
Figure 5.27: The correction field $B_c = B_{d,f} - B_{d,0}$ versus initial densities of neutron without(left) and with(right) statistical fluctuation. The error bars in the left plot show the statistical uncertainty.
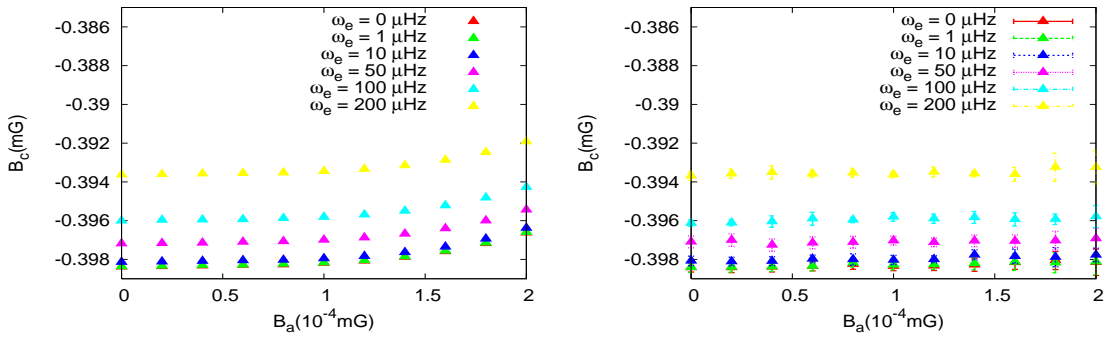

Figure 5.28: The correction field $B_c = B_{d,f} - B_{d,0}$ versus pseudomagnetic fields without(left) and with(right) statistical fluctuation.

5.8   Summary of simulation studies

In Sec. 5.4, we have seen the analysis of the free situation is straightforward. The sensitivity of the relative precession frequency is at the level of 10^{-6} Hz. The dressed spin technique is more complicated. The idea is to apply the dressing field to modify the precession frequency of neutron and ^{3}He so that they can precess together. The modulation field varies the relative angle between the two particles and enough input signals are collected for operating the feedback loop. The feedback loop corrects the dressing field amplitude so that two particles can eventually precess at the critical dressing. The correction field is related to the neutron EDM plus the offset from the dressing field. The neutron EDM can be derived from the difference in the modified dressing field between two runs with different electric field directions. The linearly increasing signal in the other cell will be used as a monitor. The statistical sensitivity of the dressed spin method is shown to be comparable to the SQUID method. The systematic sensitivity for some parameters is also studied. The drift of the holding field and the initial neutron density variation are shown not to be an important issue. The effect of the pseudomagnetic field depends on the ^{3}He density, the polarization and the initially relative angle which should be studied experimentally.
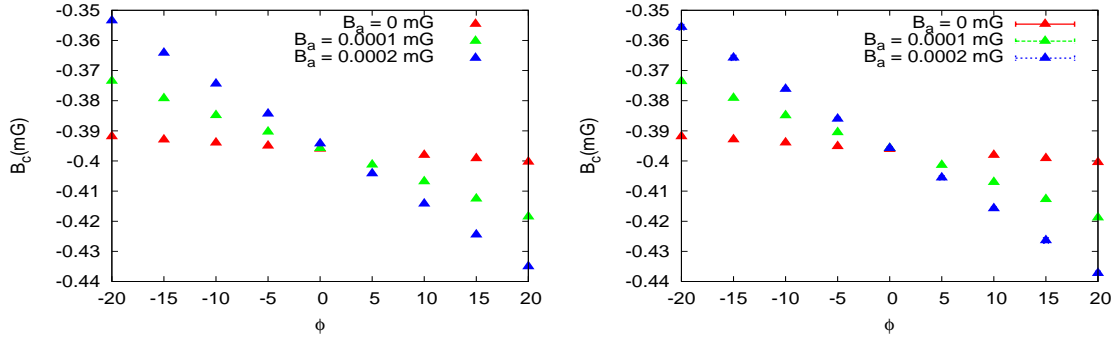
Figure 5.29: The correction field $B_c = B_{d,f} - B_{d,0}$ versus initially horizontal relative angles without(left) and with(right) statistical fluctuation.
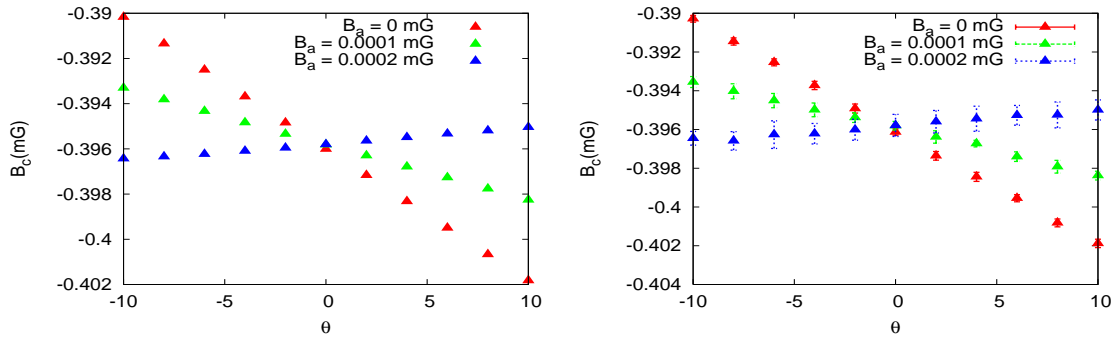

Figure 5.30: The correction field $B_c = B_{d,f} - B_{d,0}$ versus initially vertical relative angles without(left) and with(right) statistical fluctuation.

CHAPTER 6

SUMMARY

The observation of the neutron EDM remains a major challenge in physics. The potential of the neutron EDM for revealing new physics has attracted physicists into this field from generation to generation. The journey started sixty years ago with Norman F. Ramsey's first neutron EDM experiment. The size of the neutron EDM is still a puzzle waiting for people to solve, even though the experimental sensitivity has been improved by six orders of magnitude. Many novel ideas have been proposed and applied to improve the sensitivity. The goal of the next generation of experiments aims at a two orders of magnitude improvement. An original idea using the UCN production in superfluid helium together with the dressed spin technique was developed by Golub and Lamoreaux in 1994 [29]. Based on this idea, a neutron EDM experiment was proposed at the Spallation Neutron Source (SNS) at the Oak Ridge National Laboratory (ORNL) [12]. Ultracold neutrons are produced in the superfluid ^{4}He, and ^{3}He will be used as a spin analyzer and a comagnetometer. The spin-dependent absorption of neutrons by ^{3}He atoms emits scintillation light, which can be used to measure the relative precession frequency between neutron and ^{3}He. The shift of the relative precession frequency in electric field will be a signal of the neutron EDM. One of the dominant systematic errors is from the drift of the holding magnetic field, which affects the relative precession frequency. The method of the dressed spin can change the precession frequencies of neutron and ^{3}He. At the critical dressing condition, neutrons and ^{3}He can have identical effective magnetic moments. Therefore, the dressed spin technique, in principle, can strongly suppress the effect from the fluctuation of the holding magnetic field.

The goal of this research is to understand various aspects of the dressed spin technique in the proposed neutron EDM experiment. We first demonstrated the phenomenon of the dressed spin using a room temperature cell filled with polarized ^{3}He. ^{3}He nuclei were polarized through the metastability spin exchange process with optical pumping. Modification of the ^{3}He precession in the presence of dressing field was obtained for a broad range of the magnitude and frequency of the dressing magnetic field. The data have been compared with calculation using the quantum mechanical approach. The positive agreement between the theory and the experiment gives us confidence that the optimal configuration for the dressing field can be selected based on the existing theoretical formula.

In order to apply the dressed spin technique to the neutron EDM experiment, detailed simulation is necessary. When the system is at critical dressing condition with no relative initial angle, there are no

absorption signals. The authors in [29] suggested applying a modulation field with the feedback loop to measure the neutron EDM. The modulation field can cause the relative spin between neutrons and ^{3}He to move forward and backward. The difference in the scintillation light signals in different modulation half cycles can be used as an input to the feedback loop. The final correction in the dressing field is related to the neutron EDM. The idea of the modulation and the feedback loop has not been checked with detailed simulation, especially for the two-cell design of the proposed nEDM experiment. The two cells share the same dressing coils so that the dressed spin technique can only correct for one cell. The dressed spin technique needs significant modification from what we presented in [29]. Based on extensive Monte Carlo simulation, we demonstrated that the dressed spin technique can have a competitive statistical sensitivity compared with the case without the dressing field. The systematic error from the drift of the holding field is suppressed with the dressed spin method. Studies of systematic errors from other sources, such as the pseudomagnetic field, the non-zero initial angles between UCN and ^{3}He spins, and the fluctuation of the UCN intensity have also been carried out with detailed simulation. We believe this study has contributed to our understanding of various aspects associated with the application of the dressed spin technique, which may affect future neutron EDM experiments.

APPENDIX A

SENSITIVITY LIMIT DUE TO THE UNCERTAINTY PRINCIPLE

From the uncertainty principle, the sensitivity limit for energy determination, δE, is given as

$$\delta E \times T = h\delta f \times T = \hbar \tag{A.1}$$

$$\delta f = \frac{1}{2\pi T} \tag{A.2}$$

$$hf_e = 2edE \tag{A.3}$$

$$\delta f_e = 2(e\delta d)E/h = \frac{1}{2\pi T} = \frac{1}{2\pi \times 500s} = 3.183 \times 10^{-4}Hz \tag{A.4}$$

$$e\delta d = \frac{\hbar}{2ET} = \frac{6.582 \times 10^{-22}MeVs}{2 \times 50KVcm^{-1} \times 500s} = 1.3164 \times 10^{-23}e \cdot cm \tag{A.5}$$

where we use measurement time of 500 sec and 50 KV/cm E field. Repeating the measurement N times will allow determination of the frequency with and uncertainty of $\delta f/\sqrt{N}$. Instead of repeating the measurement N separate times, we can consider an ensemble of N uncorrelated systems measured simultaneously, and the same $\sqrt{N}$ reduction in frequency uncertainty results. This demonstrates the advantage of working with the highest possible number of systems. The relation in Eq. A.5 becomes

$$(e\delta d) = \frac{\hbar}{2ET}\frac{1}{\sqrt{mN}}, \tag{A.6}$$

where m represents the number of separate complete measurements of the N uncorrelated systems. Using $m = 1000$ and $N = 10^6$,

$$\delta f_e = 3.183 \times 10^{-4}\frac{1}{\sqrt{10^3 \times 10^6}} = 10^{-8}Hz = 10^{-2}\mu Hz \tag{A.7}$$

$$(e\delta d) = 1.3164 \times 10^{-23}\frac{1}{\sqrt{10^3 \times 10^6}} = 4.1628 \times 10^{-28}e \cdot cm \tag{A.8}$$

We may consider the realistic particle N and the effective T to use here. Comparing the integral of

$$\Phi(t) - \Phi_B(t),$$

$$N_{500} = \int_0^{500} N_0 e^{-\Gamma_{ave}t}(\frac{1}{\tau_\beta} + \frac{1}{\tau_3})dt = 10^6 \tag{A.9}$$

$$= N_0 \frac{1}{\Gamma_{ave}}(\frac{1}{\tau_\beta} + \frac{1}{\tau_3})(1 - e^{-500\Gamma_{ave}}) \tag{A.10}$$

$$= N_0 \times 0.758983 = 10^6 \tag{A.11}$$

$$N_0 = 1.31755 \times 10^6 \tag{A.12}$$

$$N_\infty = N_0 \times \int_0^\infty e^{-\Gamma_{ave}t}(\frac{1}{\tau_\beta} + \frac{1}{\tau_3})dt \tag{A.13}$$

$$= 1.31755 \times 10^6 \times 0.87587 = 1.154 \times 10^6 \tag{A.14}$$

where N_0 is the initial UCN number, N_∞ is the total number of UCN absorbed by ^{3}He or decay and N_{500} is the number of observed UCN in 500 seconds. The particle number for $n + {}^3$He capture should be

$$N_3 = N_{500} \times \frac{\frac{1}{\tau_3}}{\frac{1}{\tau_\beta} + \frac{1}{\tau_3}} = 10^6 \times \frac{295}{434} = 679724. \tag{A.15}$$

Taking the particle decay into account, the effective T we put in Eq. A.2 is

$$T_{ave} = \frac{\int_0^{500} t e^{-\Gamma_{ave}t}\frac{1}{\tau_3}dt}{\int_0^{500} e^{-\Gamma_{ave}t}\frac{1}{\tau_3}dt} = \frac{\frac{1}{\Gamma_{ave}^2}(1 - e^{-500\Gamma_{ave}}(1 + 500\Gamma_{ave}))}{\frac{1}{\Gamma_{ave}}(1 - e^{-500\Gamma_{ave}})} \tag{A.16}$$

$$= \frac{36842.8}{215.13} = 171.258 \tag{A.17}$$

The estimation based on uncertainty principle becomes

$$\delta f_e = \frac{1}{2\pi T}\frac{1}{\sqrt{mN}} = \frac{1}{2\pi \times 171.258}\frac{1}{\sqrt{10^3 \times 679724}} \tag{A.18}$$

$$= 3.56453 \times 10^{-8} Hz = 3.56543 \times 10^{-2} \mu Hz \tag{A.19}$$

The calculation here shows the sensitivity $3.6 \times 10^{-2} \mu\ Hz$, in qualitative agreement with the Monte Carlo result of $8.5 \times 10^{-2} \mu\ Hz$.

APPENDIX B

$\pi/2$ PULSE STUDY

A $\pi/2$ pulse is to rotate atoms polarized vertically into the horizontal plane. An rf field perpendicular to the holding field is applied at the resonance frequency, the Larmor frequency, of the atoms. The mechanism can be described using the Bloch equation [11],

$$\frac{d\vec{S}}{dt} = \vec{S} \times (\gamma \vec{B}(t)) \tag{B.1}$$

where $\vec{S}$ is the spin of the atoms, γ is the gyromagnetic ratio and $\vec{B}(t)$ is the time-dependent magnetic field. However, the resonance frequency of the rf field is not the only solution to rotate the atoms from the vertical axis to the horizontal plane. The solution can be generalized to off-resonance frequencies using the Bloch equation. Inspired by the neutron EDM experiment at the Spallation Neutron Source in the Oak Ridge National Laboratory [29], a $\pi/2$ pulse can also be applied simultaneously to two atomic species with different gyromagnetic ratios. We will generalize the idea of the $\pi/2$ pulse to two atomic species in this paper, providing a numerical method to solve the corresponding problems.

We consider a system with a static uniform magnetic field, B_0, keeping the spin orientation of polarized atoms along the $\hat{z}$-axis. If the atoms are not along the $\hat{z}$-axis, the atoms precess about the $\hat{z}$-axis at the Larmor frequency, $\omega_0 = \gamma B_0$. To apply the $\pi/2$ pulse, an oscillatory rf field perpendicular to the holding field, $B_{(}t) = 2B_1 \cos(\omega t)\hat{x}$, is applied as shown in Fig. B.1. For a typical $\pi/2$ pulse, the rf frequency ω is set at Larmor frequency of the atoms. The linear oscillatory magnetic field can be expressed in terms of two rotating components:

$$B_{rf}(t) = 2B_1 \cos(\omega t)\hat{x} = B_1(\cos(\omega t)\hat{x} + \sin(\omega t)\hat{y}) + B_1(\cos(\omega t)\hat{x} - \sin(\omega t)\hat{y}) \tag{B.2}$$

In a frame rotating counterclockwise at ω along $\hat{z}$, the first component is a static field while the second component rotates at 2ω. It will be convenient to use the "rotating field approximation" to ignore the high frequency term. In this rotating frame, the atoms will precess about the total magnetic field

$$\vec{B}_{tot} = (B_0 - \frac{\omega}{\gamma})\hat{z} + B_1\hat{x} = B_1\hat{x}. \tag{B.3}$$

To rotate exactly 90° from the $\hat{z}$-axis to the $\hat{x} - \hat{y}$ plane, a duration $\tau = (\pi/2)/\gamma B_1$ of the rf field will be
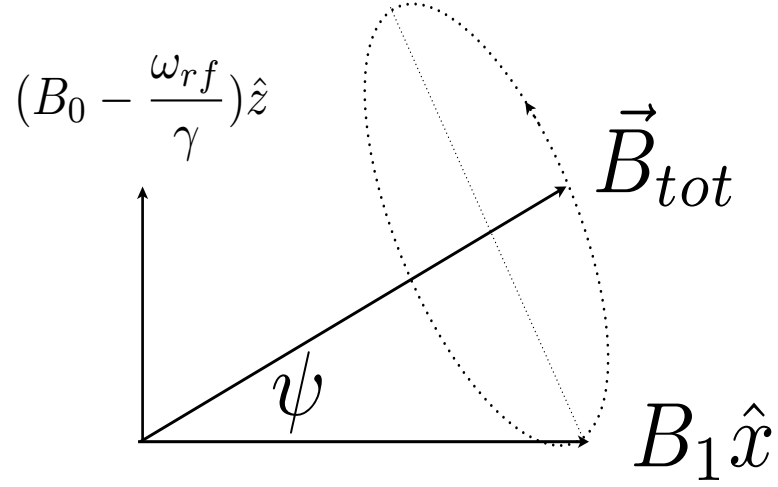
Figure B.1: Schematic plot. It shows the total magnetic field in the rotating frame at frequency ω_{rf}.

applied.

If the rf field is not at the resonance, i.e., $\omega \neq \omega_0$, the total magnetic field in the frame rotating at ω is

$$\vec{B}_{tot} = (B_0 - \frac{\omega}{\gamma})\hat{z} + B_1\hat{x}, \tag{B.4}$$

and the effective Larmor frequency is

$$\omega_0' = \gamma\sqrt{(B_0 - \frac{\omega}{\gamma})^2 + B_1^2}$$
$$= \gamma B_0\sqrt{(1 - \frac{\omega}{\gamma B_0})^2 + (\frac{B_1}{B_0})^2}. \tag{B.5}$$

We also define ψ as the angle between the direction of the $\vec{B}_{tot}$ and $\hat{x}$ so that

$$\tan\psi = \frac{B_0 - \omega/\gamma}{B_1} = \frac{B_0}{B_1}(1 - \frac{\omega}{\gamma B_0}). \tag{B.6}$$

A new coordinates is defined as

$$
\begin{bmatrix} \hat{x}' \\ \hat{y}' \\ \hat{z}' \end{bmatrix} = \begin{bmatrix} \cos\psi & 0 & \sin\psi \\ 0 & 1 & 0 \\ -\sin\psi & 0 & \cos\psi \end{bmatrix} \begin{bmatrix} \hat{x} \\ \hat{y} \\ \hat{z} \end{bmatrix}.
$$

(B.7)

The polarization of the atoms is initially along the $\hat{z}$-axis and

$$
\vec{S}(t=0) = \vec{S}_\parallel(t=0) + \vec{S}_\perp(t=0),
$$

(B.8)

where $\vec{S}_\parallel(t)$ is along the $\vec{B}_{tot}$ and independent of time,

$$
\vec{S}_\parallel(t=0) = |\vec{S}|\sin\psi\hat{x}',
$$
$$
\vec{S}_\perp(t=0) = |\vec{S}|\cos\psi\hat{z}'.
$$

(B.9)

$\vec{S}_\perp$ will be rotating about $\vec{B}_{tot}$ so that

$$
\vec{S}_\perp(t) = (|\vec{S}|\cos\psi)(\cos(\omega_0't)\hat{z}' - \sin(\omega_0't)\hat{y}')
$$

(B.10)

The total polarization is

$$
\begin{aligned}
\vec{S}(t) &= \vec{S}_\parallel(t) + \vec{S}_\perp(t) \\
&= |\vec{S}|\sin\psi\hat{x}' + (|\vec{S}|\cos\psi)(\cos(\omega_0't)\hat{z}' - \sin(\omega_0't)\hat{y}') \\
&= |\vec{S}|\sin\psi(\cos\psi\hat{x} + \sin\psi\hat{z}) + (|\vec{S}|\cos\psi)(\cos(\omega_0't)(-\sin\psi\hat{x} + \cos\psi\hat{z}) - \sin(\omega_0't)\hat{y}) \\
&= |\vec{S}|(\sin\psi\cos\psi(1 - \cos\omega_0't)\hat{x} - \cos\psi\sin\omega_0't\hat{y} + (\sin^2\psi + \cos^2\psi\cos\omega_0't)\hat{z})
\end{aligned}
$$

(B.11)

For a duration τ, the rf pulse can rotate the atoms from the vertical axis to the horizontal plane such that

$$
\vec{S}(\tau) \cdot \hat{z} = \sin^2\psi + \cos^2\psi\cos\omega_0'\tau = 0
$$
$$
\cos\omega_0'\tau = -\tan^2\psi.
$$

(B.12)

For any given ω_0 and τ, we can find out solutions of B_1 and ω satisfying this relation. In addition, if we consider a $(n + \frac{1}{2})\pi$ pulse, Eq. B.12 can be generalized to

$$
\cos(\omega_0'\tau + n\pi) = -\tan^2\psi.
$$

(B.13)

We will discuss a $(n + \frac{1}{2})\pi$ pulse for two atomic species later.

A neutron EDM experiment [29] was proposed to use ^{3}He as a spin analyzer and a comagnetometer.

The $\pi/2$ pulse is needed to rotate simultaneously the spin orientation of polarized ^{3}He and neutrons from $\hat{z}$-axis to $\hat{x}$-$\hat{y}$ plane together. The gyromagnetic ratios of neutron and ^{3}He are $\gamma_n/2\pi = -2.91647~Hz/mG$ and $\gamma_3/2\pi = -3.24341~Hz/mG$. The analytic calculation was first studied in [12] for a rotating rf field. Inspired by this experiment, we will derive more general solutions for two atomic species with different gyromagnetic ratios. The condition to have the $\pi/2$ pulse is to have simultaneous duration of ratating for two atomic species. Assuming two atomic species have gyromagnetic ratios γ_1 and γ_2, and their Larmor frequencies are $\omega_{0,1} = \gamma_1 B_0$ and $\omega_{0,2} = \gamma_2 B_0$, the duration τ will be

$$\tau = \frac{\cos^{-1}(-\tan^2(\psi_1))}{\omega'_{0,1}} = \frac{\cos^{-1}(-\tan^2(\psi_2))}{\omega'_{0,2}} \tag{B.14}$$

We define the parameters: $R = \frac{\gamma_1}{\gamma_2}$, $x = \frac{B_0}{B_1}$ and $y = \frac{2\omega}{\omega_{0,1}+\omega_{0,2}}$. Eq. B.14 becomes

$$\tau = \frac{\cos^{-1}(-(x(1-\frac{y}{2}(1+\frac{1}{R})))^2)}{\omega_{0,1}\sqrt{(1-\frac{y}{2}(1+\frac{1}{R}))^2 + x^2}} = \frac{\cos^{-1}(-(x(1-\frac{y}{2}(1+R)))^2)}{\omega_{0,2}\sqrt{(1-\frac{y}{2}(1+R))^2 + x^2}}. \tag{B.15}$$

The solutions exist when

$$\cos^{-1}\left(-x^2(1-\frac{y}{2}(1+\frac{1}{R}))^2\right) = R\frac{\sqrt{1+x^2(1-\frac{y}{2}(1+\frac{1}{R}))^2}}{\sqrt{1+x^2(1-\frac{y}{2}(R+1))^2}} \cos^{-1}\left(-x^2(1-\frac{y}{2}(1+R))^2\right). \tag{B.16}$$

To find out solutions, x, y and R are varied step by step. The difference between the left side and the right side of Eq. B.16 is defined as Δ. First x and R are fixed and then y is varied step by step. If the sign of Δ is changed, the corresponding x, y and R are recorded. Fig. B.2 shows solutions of the rf frequency verse the rf amplitude for different R. The time duration τ for $R = \gamma_3/\gamma_n$ is also shown in Fig. B.2. To generalize the $\pi/2$ pulse to two arbitrary atomic species having different gyromagnetic ratios, we vary R step by step to calculate possible solutions. Fig. B.3 shows the range of R verse x and y while solutions can only exist between $0.707 < R < 1.415$. When $R \to 1$, the $\pi/2$ pulse can work for all $x > 1$ and $y < 1$. We can conclude that the amplitude of the rf field cannot be larger than the holding field and the frequency has be smaller than the average of two Larmor frequencies. Next we consider the cases if $n = 1$ which can be called a $\frac{3}{2}\pi$ pulse and $n = 2$, called a $\frac{5}{2}\pi$ pulse, shown in Fig. B.3. The $\frac{3}{2}\pi$ pulse has a small range of R, $0.94 < R < 1.06$ while the $\frac{5}{2}\pi$ pulse has a much smaller range of R, $0.97 < R < 1.03$.

To confirm the solutions, the Bloch equation is applied to simulation the spin dynamics of two atomic species, for example, neutrons and ^{3}He, for both the rotating rf field and the linear rf field. The Runge-Kutta method is applied and the time step of the simulation is $\Delta t = 10^{-6}~sec$. In order to find out solutions, we scan all possible values of the rf field amplitude, B_1, and frequency, ω. First B_1 is fixed and then ω is varied. When the spin of neutrons is rotated into the horizontal plane first time, i.e., the vertical component of spin, $S_{z,n}$ becomes negative from positive, the vertical spin component of ^{3}He, $S_{z,3}$, is recorded. The difference between spin of two species is defined as $\Delta S_z = S_{z,3} - S_{z,n}$. We record the
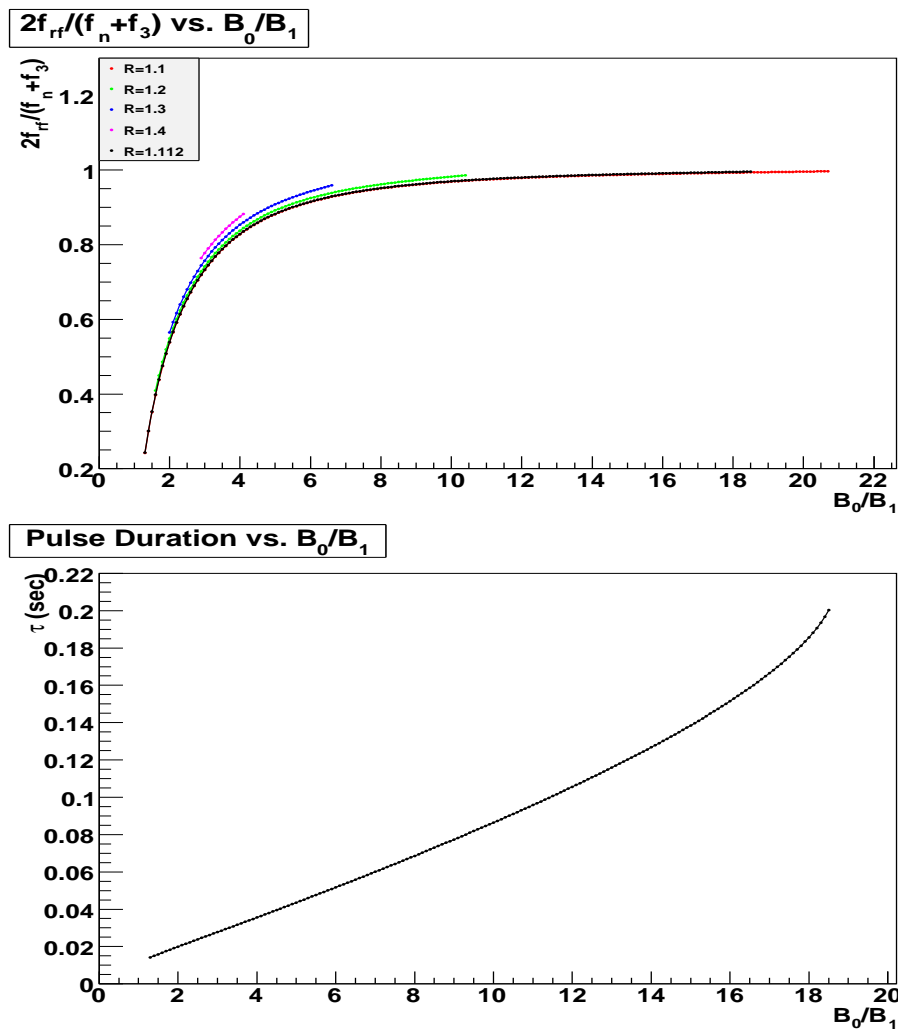
93

Figure B.2: The available value for $\pi/2$ pulse. Top) $f_{RF}/0.5(f_3 + f_n)$ vs. B_0/B_1 for different R where black dots are for $R = \gamma_3/\gamma_n$. Bottom) $\pi/2$ pulse time duration vs. B_0/B_1 for $R = \gamma_3/\gamma_n$.
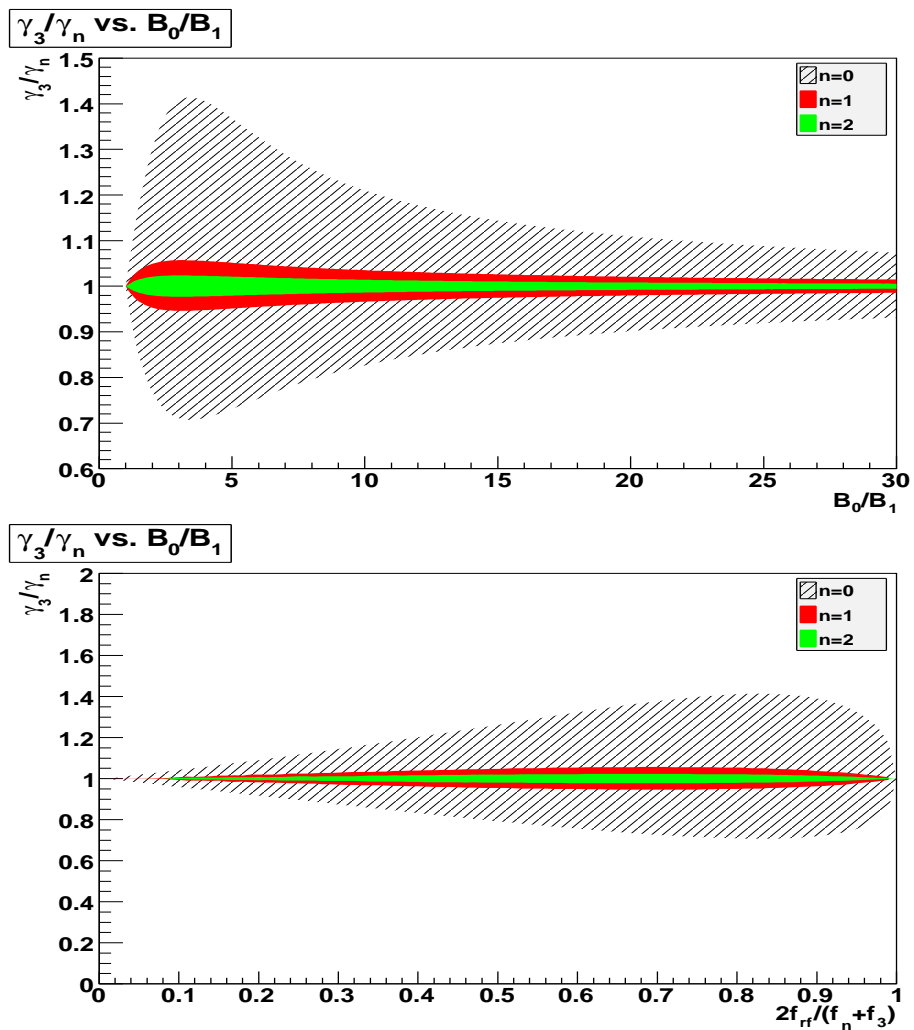
Figure B.3: The available values for $(n + \frac{1}{2})\pi$ pulse where $n = 0, 1, 2$. Top) R vs. B_0/B_1. Bottom) R vs. $f_{RF}/0.5(f_3 + f_n)$.
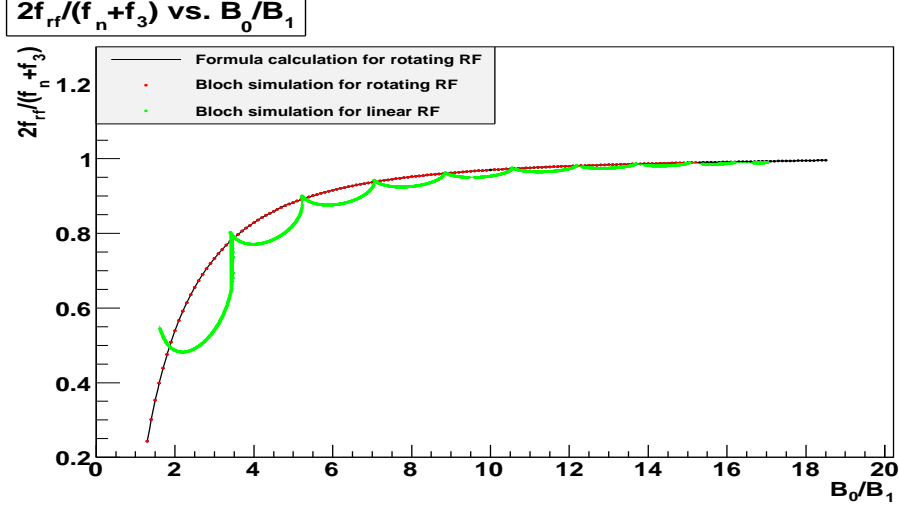
Figure B.4: The solution of B_1 and ω for neutron and ^{3}He. The Bloch equation simulation is applied for both the rotating rf field and the linear rf field.

corresponding ω if the sign of ΔS_z is changed. Next we vary B_1 a small step and repeat the scan of ω until no solution.

The rotating rf field is

$$B_x = B_1 \sin(\omega t), \ B_y = B_1 \cos(\omega t), \ B_z = B_0, \tag{B.17}$$

and the linear rf field is

$$B_x = 2B_1 \cos(\omega t), \ B_y = 0, \ B_z = B_0, \tag{B.18}$$

where $B_0 = 10$ mG. The spin is counterclockwise rotating around $\hat{z}$-axis and ^{3}He is running faster than neutron. In Fig. B.4, the solutions of the rotating rf field using the Bloch equation are consistent with the numerical solution in Eq. B.16 and Fig. B.2. However, the linear rf field will be used in the experiment, not the rotating rf field. The solutions of the linear rf field, shown in Fig. B.2, are different from the solutions of the rotating rf field, containg an interesting pattern. After a $\pi/2$ pulse, the corresponding vertical components of spins of neutrons and ^{3}He for different x and the corresponding y are shown in Fig. B.5. ΔS_z can be improved if we use finer time step for the Bloch equation simulation and finer small step of ω to search for solutions. The relative angle between neutron and ^{3}He after a $\pi/2$ pulse, $\Delta\phi_{n3}$, is shown in Fig. B.6. One advantage is we can choose the proper $\Delta\phi_{n3}$ if we need different initial angle for the neutron EDM measurement.

The simulation shows we can find out solutions of the $\pi/2$ pulse for different setups of B_1 and ω. The potential of using the $(n + \frac{1}{2})\pi$ pulse needs further study. If we consider different number of cycles for two atomic species, we may rotate simultaneously two atomic species with very different gyromagnetic ratios to
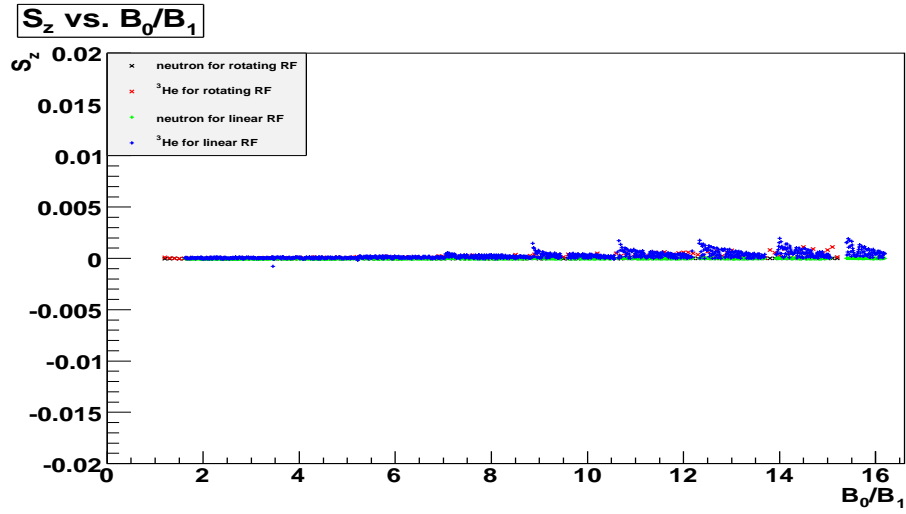
96

Figure B.5: The vertical component of spin, S_z, of neutron and ^{3}He verse x using the rotating rf field and the linear rf field.
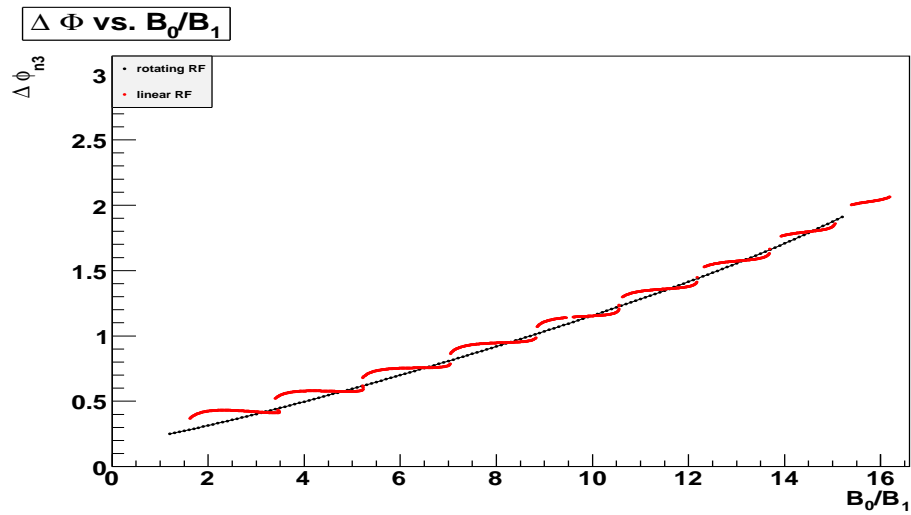

Figure B.6: The relative angle difference between neutron and ^{3}He after a $\pi/2$ pulse, $\Delta\phi_{n3}$, verse x.

the horizontal plane. It may provide a broader range for choosing the angle $\Delta\phi_{n3}$.

APPENDIX C

T_2 STUDY

C.1 Data

One interesting question is how the T_2 relaxation time is affected by the uniformity of dressing field. The left plot of Fig. C.1 shows a measurement of the T_2 relaxation for various values of x and y. It is interesting that T_2 deteriorates rapidly when y approaches 1, shown in the right plot of Fig. C.1. Future simulation work as well as laboratory tests are expected.

C.2 McGregor's study

McGregor [50] shows how a magnetic field gradient affects transverse relaxation rate of spin-polarized ^{3}He. The T_2 is

$$\frac{1}{T_2} = \frac{1}{2T_1} + \frac{\gamma^2 L^4}{120D}(\frac{\partial H_z}{\partial x})^2 + \frac{7\gamma^2 a^4}{96D}(\frac{\partial H_z}{\partial y})^2 \tag{C.1}$$

for a cylindrical cell whose axis is parallel to $\hat{x}$ and perpendicular to the $H_0\hat{z}$. The T_2 for spherical cell is

$$\frac{1}{T_2} = \frac{1}{2T_1} + \frac{8\gamma^2 L^4}{175D}(\frac{\partial H_z}{\partial z})^2. \tag{C.2}$$

We consider the following case. Diffusion constant of ^{3}He, $D = 1370.2 cm^2/s$ for $1\ Torr$ and $300K$, is proportional to $T^{\frac{3}{2}}/P$. Gyromagnetic ratio of ^{3}He, γ, is $0.2037\ Sec^{-1}\ nT^{-1}$. We ignore T_1 term $(T_1 \sim 2 \times 10^7)$ and $\frac{\partial H_z}{\partial y}$ term. The cylindrical cell length is $L = 12.35\ cm$. The spherical cell radius, $R = 4.96/2\ cm$. The pressure of the cylindrical cell is $5\ Torr$ so that $D' = D/5$. The pressure of the spherical cell is 10 Torr so that $D' = D/10$. Fig. C.2 reproduces McGregor's result.

C.3 Calculation of the holding field B_0

The NMR system at UIUC has a (rough) Helmholtz coil consisting of two identical circular magnetic coils that are placed symmetrically on both sides of the experimental area along a common axis($\hat{z}$) and separated by a distance $h = 20 \pm 0.5\ in. = 0.508 \pm 0.0127\ m$ equal to the radius $R = 20\ in. = 0.508\ m$ of
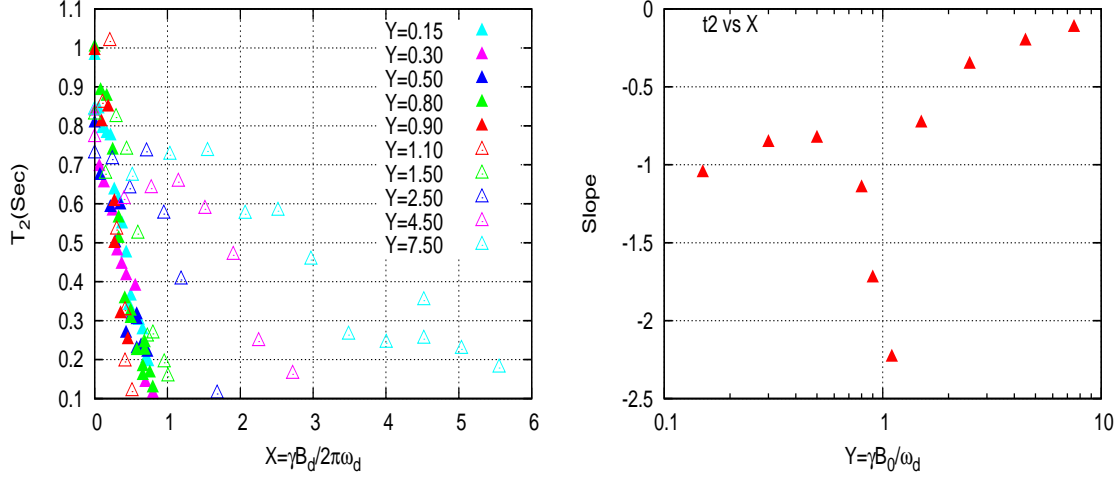
Figure C.1: Left) T_2 versus x for various values of y. Right) The slope of T_2 verse x plotted as a function of y. It shows the steep slopes as y approaches 1.

the coil. Each coil has $N = 15$ turns and with the current $I = 8\ Amp$. Assume the width of the wire is $0.001\ m$ and the total width of the coil is $0.015\ m$. The center is located at perfect Helmholtz coil position. We divide the ϕ of the coil into 180 pieces as in Fig. C.3. The cylindrical ^{3}He cell placed at the center along the Helmholtz coil ($\hat{z}$) has length $L = 0.057\ m$ and radius $r = 0.025\ m$. We divide the ϕ into 180 pieces, ρ into 20 pieces and z into 20 pieces. Fig. C.4 presents the space division of the cell.

We use the Biot-Savart law to calculate the magnetic field at each point, as described above, of the experimental area between two coils.

$$\vec{B}(\vec{r}) = \sum_{\vec{dl}} (\frac{\mu_0}{4\pi}) IN \frac{\vec{dl} \times (\vec{l} - \vec{r}/|\vec{l} - \vec{r}|)}{(\vec{l} - \vec{r})^2}, \tag{C.3}$$

where $\vec{dl}$ is along the current segment, $\mu_0/4\pi = 4\pi \times 10^{-7}/4\pi = 1 \times 10^{-7} NA^{-2}$ and B is in unit [Tesla]. Fig. C.5 and Fig. C.6 show the magnetic field distribution at some location in the experimental area. We can use the same method to calculate the magnitude and the gradient of the magnetic field, shown in Tab. 3.1, which compensates the Earth vertical field.

C.4 Calculation of the T_2

T_2 depends on the gradient of the magnetic field and the geometric structure of the cell. Using the method in [49], we get

$$\frac{1}{T_2} = \frac{1}{2T_1} + \frac{\gamma^2 L^4}{120D}(\frac{\partial H_z}{\partial z})^2 + \frac{7\gamma^2 a^4}{96D}[(\frac{\partial H_z}{\partial x})^2 + (\frac{\partial H_z}{\partial y})^2], \tag{C.4}$$

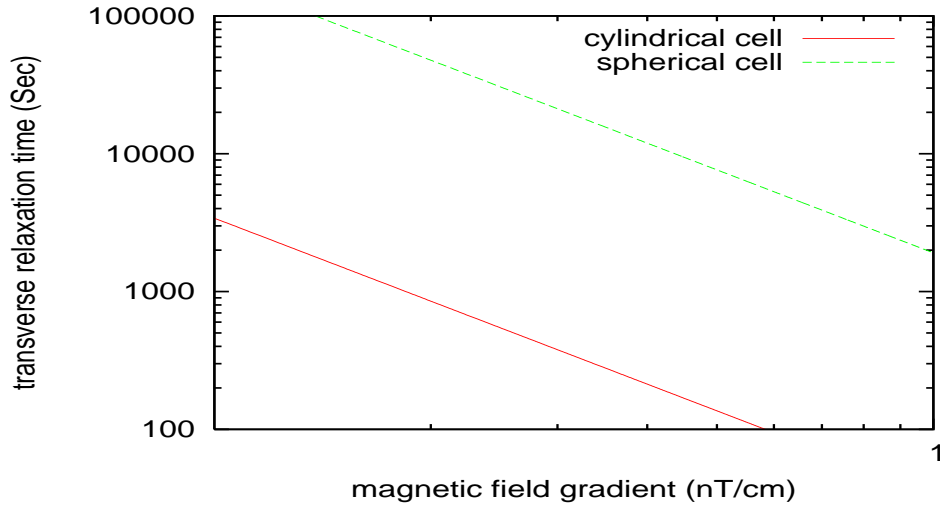where the length of the cell $L = 0.057\ m$ and the radius of the cell $a = 0.025\ m$.

100

Figure C.2: Transverse relaxation time of spin-polarized ^{3}He as a function of the magnetic field gradient.
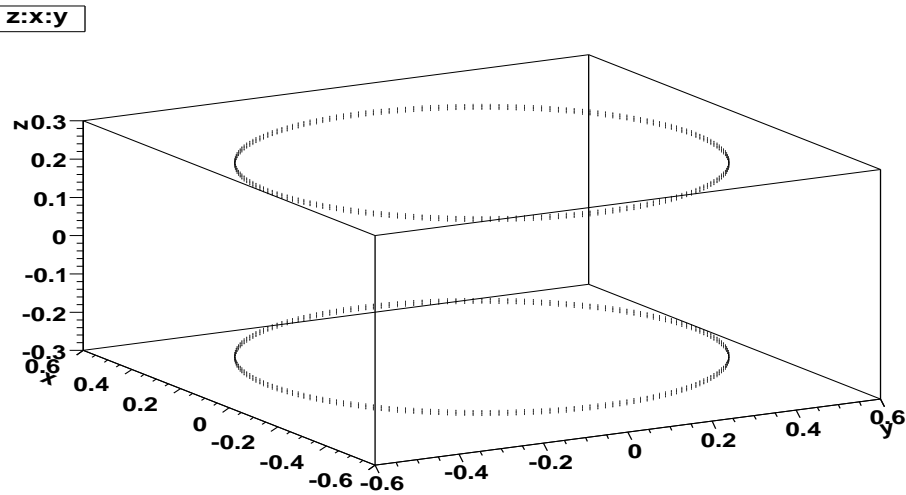

Figure C.3: Helmholtz coil in unit [m].

Considering the gradient of the holding field and the field compensating the vertical component of the Earth field, we get the T_2 result in Fig. C.7 at $\hat{x} - \hat{y}$ plane and Fig. C.8 at $\hat{x} - \hat{z}$ plane. To find out the T_2 for the cell, we average the T_2 through the whole volumn. The result is around ~ 0.9 sec which seems to be consistent with the measurement. The effect of the dressing field to the T_2 is still an open question.
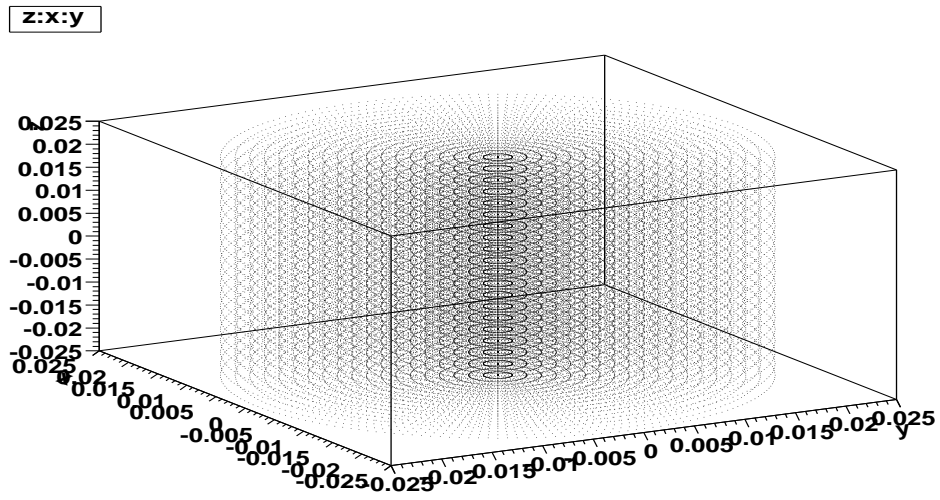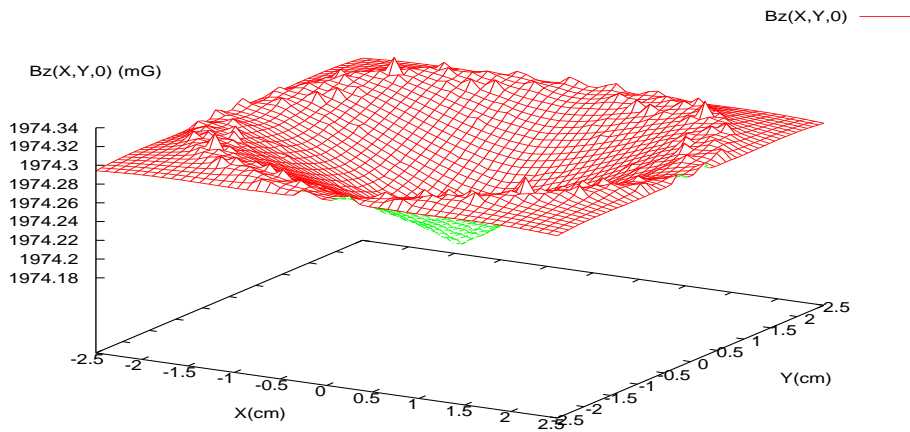
Figure C.4: The cylindrical cell in unit [m].

Figure C.5: Magnetic field distribution of B_z at $z = 0$ and $\hat{x} - \hat{y}$ plane .
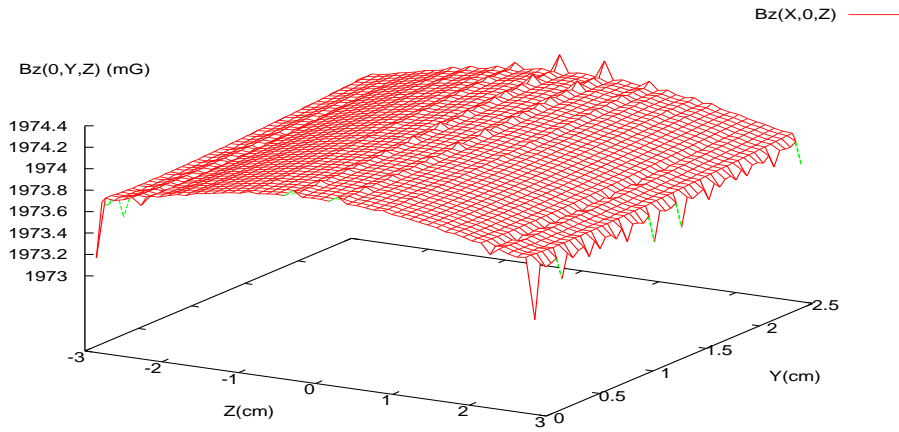
Bz(0,Y,Z) (mG)

Figure C.6: Magnetic field distribution of B_z at $\hat{x} - \hat{z}$ plane .
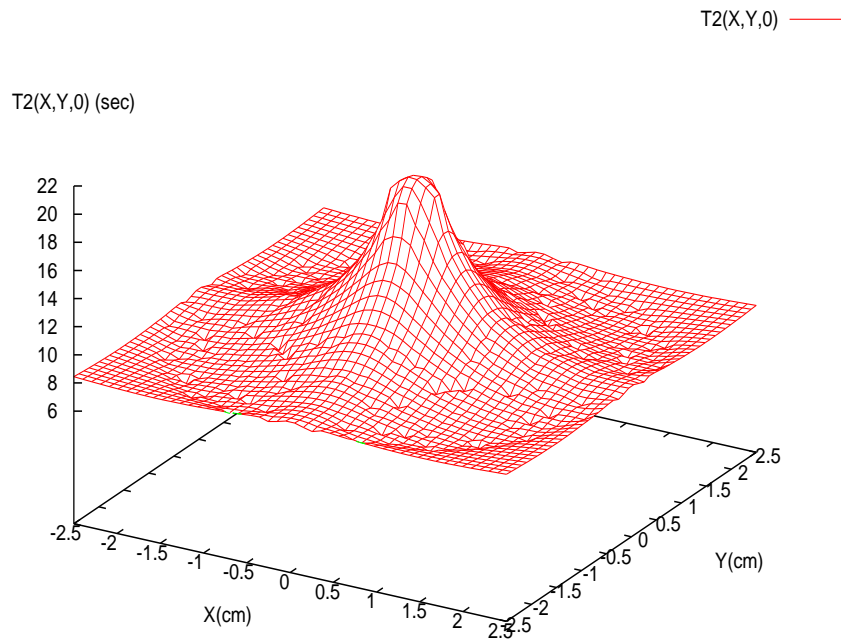
T2(X,Y,0) (sec)

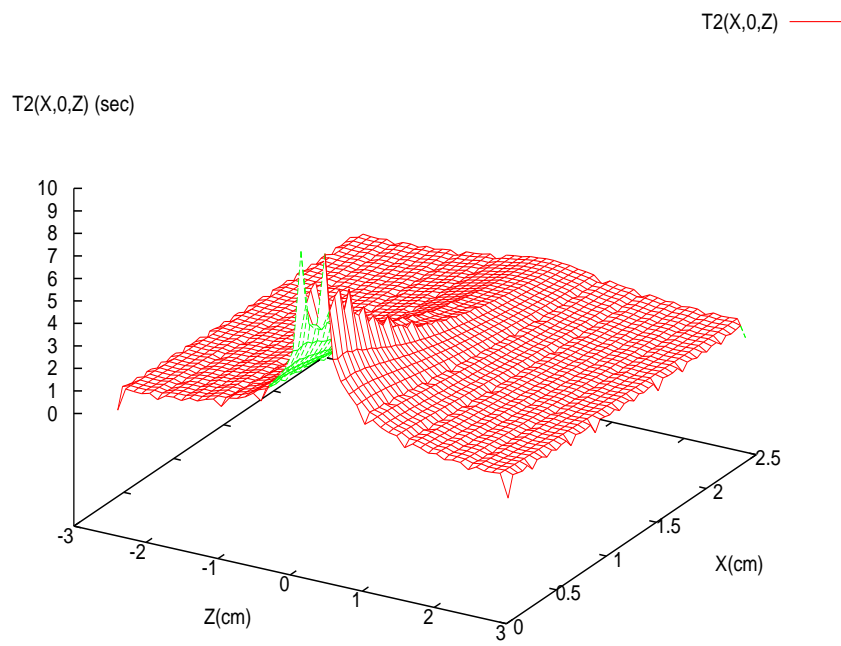Figure C.7: T_2 distribution at $\hat{x} - \hat{y}$ plane.

Figure C.8: T_2 distribution at $\hat{x} - \hat{z}$ plane.

APPENDIX D

SIGNALS OF THE PICKUP COILS

It is of interest to estimate the magnitude of signals of the pickup coils, which helps the design of the coils. For a magnetic moment $\vec{\mu}$ lying along the $\hat{x}$-axis, the magnetic field is given by

$$\vec{B}(\vec{r}) = \frac{\mu_0}{4\pi r^3}[3(\vec{\mu} \cdot \hat{r})\hat{r} - \vec{\mu}] \tag{D.1}$$

$$(\vec{\mu} \cdot \hat{r})\hat{r} = \mu \ \hat{x} \cdot (\cos\phi \ \hat{x} + \sin\phi \ \hat{y})(\cos\phi \ \hat{x} + \sin\phi \ \hat{y})$$

$$= \mu(\cos^2\phi \ \hat{x} + \cos\phi\sin\phi \ \hat{y})$$

$$\vec{B}(\vec{r}) = \frac{\mu_0}{4\pi R^3}[3\mu(\cos^2\phi \ \hat{x} + \cos\phi\sin\phi \ \hat{y}) - \mu \ \hat{x}]$$

$$= \frac{\mu_0\mu}{4\pi R^3}[(3\cos^2\phi - 1) \ \hat{x} + 3\cos\phi\sin\phi \ \hat{y})] \tag{D.2}$$

The flux of $\vec{B}$ through a loop of area A with outward normal is proportional to

$$\Phi \propto \vec{B} \cdot \hat{r} = \frac{\mu_0\mu}{4\pi R^3}[3\cos^3\phi - \cos\phi + 3\cos\phi\sin^2\phi] = \frac{\mu_0\mu}{4\pi R^3}[2\cos\phi]. \tag{D.3}$$

Therefore the flux is

$$\Phi(\phi) = \frac{\mu_0\mu A}{2\pi R^3}\cos\phi \tag{D.4}$$

The loop rotates around $\vec{\mu}$ in the $\hat{x} - \hat{y}$ plane at freqency ω so that

$$\frac{d\Phi(\phi)}{dt} = \frac{d\Phi}{d\phi}\frac{d\phi}{dt} = -\frac{\mu_0\mu A}{2\pi R^3}\sin\phi \cdot \omega \tag{D.5}$$

The induced emf for one loop is

$$emf = -\frac{d\Phi(t)}{dt} = \frac{\mu_0\mu A}{2\pi R^3}\sin\phi \cdot \omega. \tag{D.6}$$

Assuming the loop has C turns, n pickup coils, N atoms contributing to the B field and the average

projection of their spins onto $\hat{x}$-axis is P, the net signal is

$$\epsilon(t) = \frac{\mu_0 \mu C n N P A}{2\pi R^3} \omega \sin \omega t. \tag{D.7}$$

$$\epsilon_{RMS} = \frac{\mu_0 \mu C n N P A \omega}{2\sqrt{2}\pi R^3} \tag{D.8}$$

We can use the following values for Eq. D.8:

$$\mu_0 = 4\pi \times 10^{-7} N A^{-2}$$

$$\vec{\mu} = \frac{\gamma \hbar}{2} = \frac{2\pi \times 32.434 M Hz T^{-1} \times 6.582 \times 10^{-22} MeV s}{2} = 6.7 \times 10^{-14} MeV T^{-1}$$

$$C = 80$$

$$n = 4$$

$$N = \frac{PV}{kT} = \frac{1 torr \times (\pi(0.025)^2(0.057)) m^3}{1.38 \times 10^{-23} J K^{-1} \times 291 K}$$

$$= \frac{133.322 N m^{-2} \times 1.11919 \times 10^{-4} m^3}{401.58 \times 10^{-23} J} = \frac{1.49213 \times 10^{-2} N m}{401.58 \times 10^{-23} J}$$

$$= 3.71565 \times 10^{18}$$

$$P = 20\%$$

$$A = 0.05 \times 0.0635 m^2 = 3.175 \times 10^{-3} m^2$$

$$\omega = 2\pi \times 1200 Hz = 7539.82 Hz$$

$$R = 0.025 m.$$

We will get ϵ_{RMS} is

$$\epsilon_{RMS} = 3.45214 \times 10^6 \times 1.6 \times 10^{-13} \frac{kg \cdot m^2}{C \cdot s^2} = 5.52342 \times 10^{-7} Volt$$

$$= 0.552342 \mu V. \tag{D.9}$$

The impedance of the pickup coils is 65.7 Ω.

APPENDIX E

SIGNALS OF LOCK-IN AMPLIFIER

The width of signals in Fig. 3.4 can be well explained by considering the function of the Lock-in Amplifier. We use a function generator to test the width of lock-in amplifier output. The function generator generates a sine wave at $1200\ Hz$ and $1\ Volt$. If the reference frequency of the lock-in amplifier is set at $1200\ Hz$, we will get a DC signal at $0.7053\ Volt$, consistent with the rms of the amplitude. Next we vary the function generator frequency. For different time constants τ and different roll-off's, Fig. E.1 shows the correponding output voltage versus the frequency shift.

The Lock-in amplifier sets a bandwidth of low-pass filter by changing the time constant which is simply $1/2\pi\nu$. To understand the relation between the time constant and the bandwidth, we introduce a differential equation as

$$\frac{dV}{dt} + \frac{V}{\tau} = f(t) = Ae^{i\omega t}. \tag{E.1}$$

where τ represents the exponential decay constant and V is a function of time t. The right-hand side is an external driving function, which can be regarded as the system input, to which V(t) is the response, or the system output. The general solution, assuming $V(t = 0) = V_0$, is

$$V(t) = V_0 e^{-\frac{t}{\tau}} + Ae^{-\frac{t}{\tau}} \int_0^t dt' e^{\frac{t'}{t}} e^{i\omega t'},$$

$$= V_0 e^{-\frac{t}{\tau}} + \frac{A}{i\omega + \frac{1}{\tau}} (e^{i\omega t} - e^{-\frac{t}{\tau}}). \tag{E.2}$$

At large t, the decaying exponentials become negligible and the steady-state solution is

$$V_\infty(t) = A\frac{e^{i\omega t}}{i\omega + 1/\tau}. \tag{E.3}$$

The magnitude of this response is

$$|V_\infty(t)| = \frac{A}{(\omega^2 + 1/\tau^2)^{1/2}} = \frac{A\tau}{\sqrt{1 + (\omega\tau)^2}}. \tag{E.4}$$

The bandwidth of this system is the frequency where $|V_\infty|^2$ drops to half-value, or where $\omega\tau = 1$.
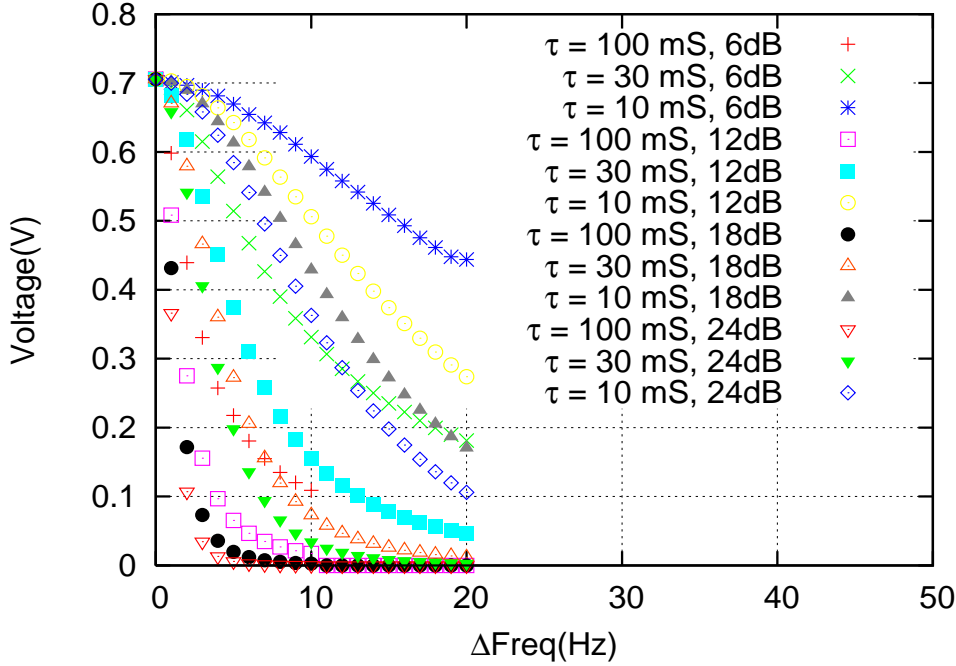
Figure E.1: The output voltage versus the frequency shift.

For a RC filter, the voltage transfer function, A, is

$$A = \frac{V_o}{V_i} = \frac{1}{1 + i\omega RC}. \tag{E.5}$$

At $\omega_c = 1/RC = 1$, the power ratio is

$$|A|^2 = \frac{1}{1 + (\omega/\omega_c)^2} = \frac{1}{1 + (\omega)^2}, \tag{E.6}$$

which can be expressed as a loss,

$$L = -10 \log |A|^2 = 10 \log (1 + \omega^2) \approx 10 \log \omega^2 = 20 \log \omega \tag{E.7}$$

The roll-off is given by

$$\Delta L = 20 \log \frac{\omega_2}{\omega_1}. \tag{E.8}$$

If $\omega_2/\omega_1 = 2$, ΔL is equal to $20 \log 2 = 6dB/oct$ which means the power drops 6 dB where the frequency drops half. We can normalize Fig. E.1 by ν_{-3dB} which is defined as the $-3dB$ frequency of the filter when the power is half. Fig. E.2 shows the gain, which is defined as $(V/V(\nu = 0))^2$, versus ν/ν_{-3dB}. For $6dB/oct$, we can see gain is equal to 0.5 at $\nu/\nu_{-3dB} = 1$. Higher order roll-off can be achievable. The
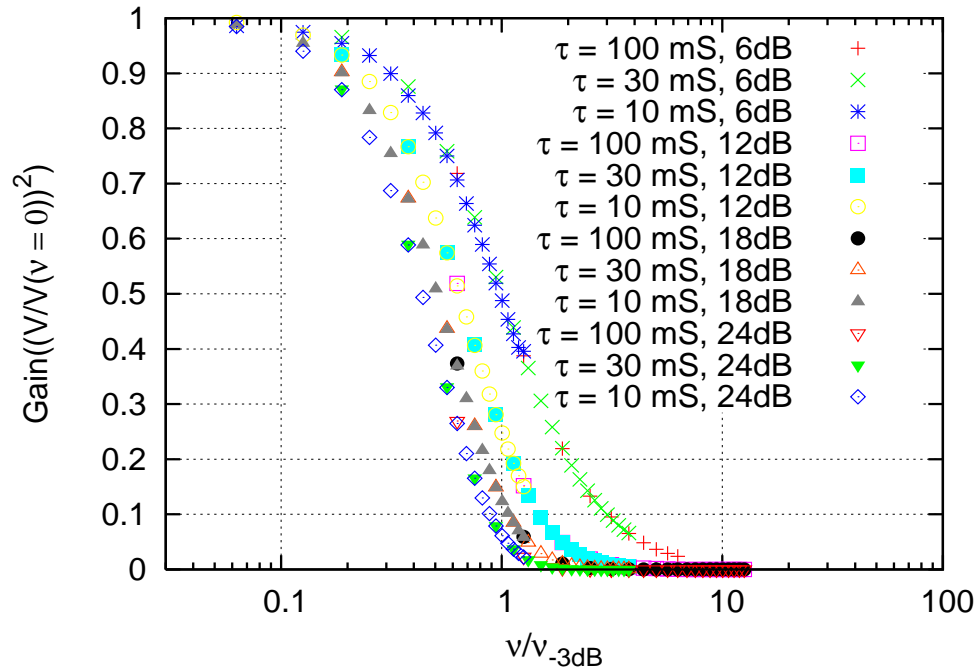
Figure E.2: $(V/V(\nu = 0))^2$ verse ν/ν_{-3dB}.

digital signal processor can achieve up to four filter stages at 24 dB/oct of roll-off.

Therefore, the width of signals in Fig. 3.4 can be well understood from the consideration of the time constant and the roll-off.

APPENDIX F

SENSITIVITY AND THE REQUIRED UNIFORMITY OF THE MAGNETIC FIELDS

The neutron and ^{3}He absorption signal depends on the relative precession frequency between two particles. The relative precession frequency can be described as

$$\omega_\gamma = 2\pi f_\gamma \equiv (\gamma_3 - \gamma_n)B_0 \pm 2Ed_n/\hbar, \tag{F.1}$$

where 3 is for ^{3}He and n is for neutron. From measuring the frequency difference, we can determine neutron EDM value. The drift of B_0 is a source of systematic error. The ILL collaboration showed that their $B_0 = 10$mG has a drift around 5×10^{-4} mG shown in Fig. 2.5, which can cause a relative precession frequency shift of $\Delta f_\gamma = 164\mu$Hz. The frequency shift from the EDM is $\omega_e = 2Ed_n/\hbar$. If $d_n = 6 \times 10^{-26}e \cdot cm$ and $E = 50KV/cm$, $\omega_e = 2\pi \times 1.45\mu$Hz. The ILL applied the comagnetometer ^{199}Hg to monitor B_0 in order to reduce the effect of B_0 drift.

An alternative method is to apply the dressed spin technique. The statistical sensitivity with and without dressed spin should be comparable [29, 44]. However, to apply the dressed spin technique, we also need to consider the uniformity of the magnetic field to achieve the critical dressing field condition.

When the dressing field is applied, Eq. F.1 becomes.

$$2\pi f_\gamma = (\gamma_3' - \gamma_n')B_0 \pm 2Ed_n/\hbar = f_\gamma(x,y) \pm 2Ed_n/\hbar,$$
$$\Delta f_\gamma(x,y) = \left(\frac{\partial f_\gamma(x,y)}{\partial x}\right)_y \Delta x + \left(\frac{\partial f_\gamma(x,y)}{\partial y}\right)_x \Delta y \tag{F.2}$$

Assuming we can make the dressing field frequency very stable, we only consider possible drifts of the magnetic fields. The ILL group shows that the drift at $B_0 = 10mG$ can be on order of $5 \times 10^{-4}mG$. We assume the same relative drift for both B_0 and B_1. If $x = \frac{\gamma_n B_1}{\omega}$ and $y = \frac{\gamma_n B_0}{\omega}$, we can get

$$\frac{\Delta B_1}{B_1} = \frac{\Delta B_0}{B_0} = \frac{5 \times 10^{-4}}{10} = 5 \times 10^{-5}, \tag{F.3}$$
$$\frac{\Delta x}{x} = \frac{\Delta y}{y} = 5 \times 10^{-5}. \tag{F.4}$$

F.1 B_0 drift

The Hamiltonian in unit of $\hbar\omega$ for a particle with gyromagnetic ratio γ subjected to a constant magnetic field $B_0\hat{z}$ and a linearly polarized rf field $B_1\cos\omega t\hat{x}$ can be written as

$$\begin{aligned}
\frac{\mathcal{H}}{\hbar\omega} &= (\frac{\gamma B_0}{\hbar\omega})\hat{S}_z + \hat{a}^\dagger\hat{a} + \frac{\lambda}{\hbar\omega}\hat{S}_x(\hat{a} + \hat{a}^\dagger) \\
&\equiv \frac{y}{2}\hat{\sigma}_z + \hat{a}^\dagger\hat{a} + \frac{x}{4\sqrt{\bar{n}}}\hat{\sigma}_x(\hat{a} + \hat{a}^\dagger),
\end{aligned} \tag{F.5}$$

where $\hat{S}_x = \frac{\hbar}{2}\hat{\sigma}_x$ and $\hat{S}_z = \frac{\hbar}{2}\hat{\sigma}_z$ are the spin operators along $\hat{x}$ and $\hat{z}$ respectively. The first term in Eq. F.5 is the Zeeman interaction of the spin with B_0, and the second term is the energy of the dressing field (rf field) with creation and annihilation operators $\hat{a}^\dagger$ and $\hat{a}$. The final term describes the coupling between the spins of the particles and the rf field with strength $\lambda = \gamma B_1/2\sqrt{\bar{n}}$, where $\bar{n} \gg 1$ is the average number of photons. This interaction term allows the particle to absorb or emit photons and exchange energy and angular momentum with the rf field. Because the rf field is perpendicular to B_0 and can be decomposed into a superposition of right- and left-handed circularly polarized fields, only $\Delta m_z = \pm 1$ transitions are allowed.

In the weak-field region, i.e., $B_0 \ll \omega/\gamma$ ($y \ll 1$), Eq. F.5 can be solved analytically with the result $\gamma' = \gamma J_0(x)$ [63]. The precession frequency becomes

$$\frac{\omega^{eff}}{\omega_0} = \frac{\gamma' B_0}{\gamma B_0} = J_0(x), \tag{F.6}$$

which only depends on the dressing strength $x = \gamma B_1/\omega$.

In reference [29], the higher-order corrections to the eigenvalues were also shown. They are given as:

$$E_n^{(0)} = n \tag{F.7}$$

$$E_{n,m}^{(1)} = \frac{y}{2}mJ_0(x) \tag{F.8}$$

$$\begin{aligned}
E_{n,m}^{(2)} &= \sum_{m',n'\neq n} \frac{\left|\left\langle m',n'\left|\frac{y}{2}\sigma_z\right|m,n\right\rangle\right|^2}{E_{n'}^{(0)} - E_n^{(0)}} \\
&= \frac{y^2}{4}\sum_{m',n'\neq n} \frac{\frac{1}{4}(m^2 J_q(x)^2 + m'^2 J_q(-x)^2 + 2mm' J_q(x)J_q(-x))}{q} \\
&= \frac{1}{8}y^2\sum_{q\neq 0}\frac{J_q(x)^2}{q} = 0
\end{aligned} \tag{F.9}$$

$$E_{n,m}^{(3)} \approx -\frac{m}{8}y^3 J_0(x)\sum_{q=1}^{\infty}\frac{J_q(x)^2}{q^2}, \tag{F.10}$$

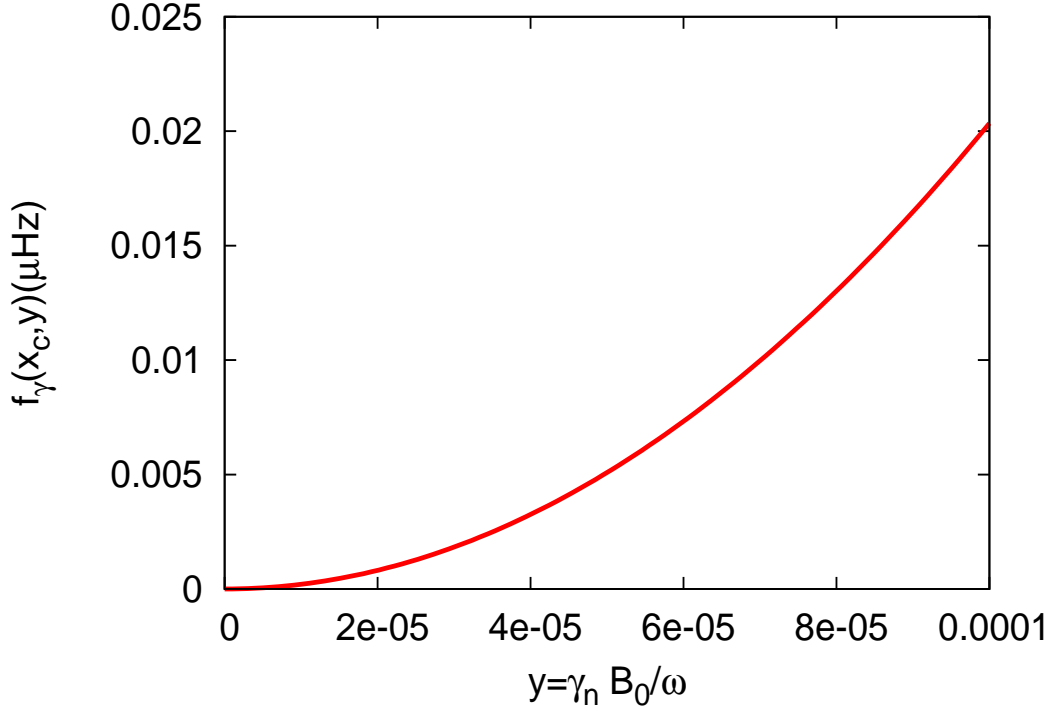where $m = \pm 1$. $E^{(2)} = 0$, since the sum extends over all $\pm q \neq 0$.

Figure F.1: $f_\gamma(x_c, y)$ v.s. y

To calculate the precession frequency, we have

$$y = \frac{2\pi f_0}{\omega},$$

$$f_{neutron} \equiv f_n = (\frac{\omega}{2\pi}) \cdot (E_+ - E_-) = E_+^{(1)} - E_-^{(1)} + E_+^{(3)} - E_-^{(3)}$$

$$= f_0 J_0(x) - f_0 \frac{y^2}{4} J_0(x) \sum_{q=1}^{\infty} \frac{J_q(x)^2}{q^2}. \tag{F.11}$$

The precession frequency between neutron and ^{3}He at the critical point x_c shown in Fig. F.1 will be

$$f_\gamma(x_c, y) = f_3 - f_n = f_{n,0} \frac{y^2}{4} J_0(x_c) \sum_{q=1}^{\infty} \frac{J_q(x_c)^2}{q^2} - f_{3,0} \frac{(\frac{\gamma_3}{\gamma_n} y)^2}{4} J_0(\frac{\gamma_3}{\gamma_n} x_c) \sum_{q=1}^{\infty} \frac{J_q(\frac{\gamma_3}{\gamma_n} x_c)^2}{q^2}$$

$$\approx 2.035 y^2 \tag{F.12}$$

and

$$\Delta\omega_\gamma = 2\pi\Delta f_\gamma = 2\pi \times 2.035 \times 2 \times y \times \Delta y \approx 8\pi \times y^2 (\Delta y/y)(\mu Hz). \tag{F.13}$$
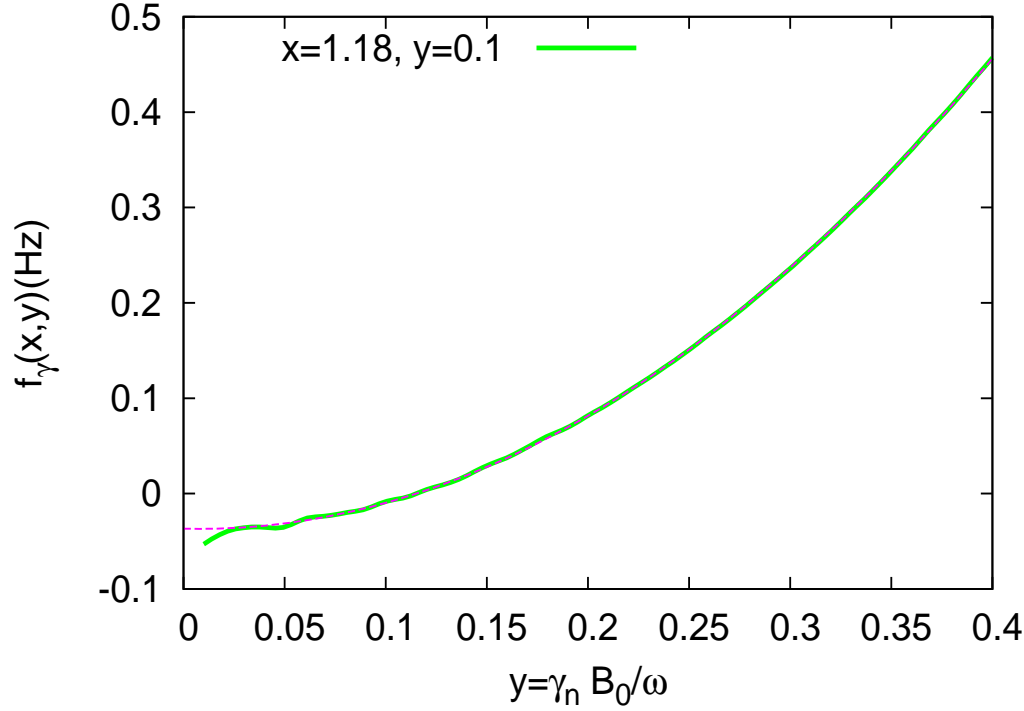
Figure F.2: $\Delta f_\gamma(\Delta x/x)$ v.s. y. We obtain the fitting function:$f_\gamma(x_c = 1.18, y) = -0.0367783 - 0.0492097y + 3.20374y^2$

Eq. F.13 shows that for $y = 0.01$ and $\Delta y/y = 5 \times 10^{-5}$, $\Delta f_\gamma = 0.02\mu Hz$. One can conclude that the effect due to shift in y (originating from shifts in B_0 or ω) is small, provided that y is small.

If we set $x_c = 1.18$, we can find out the relative precession frequency versus y. To fit the data as shown in Fig. F.2, we obtain the function $f_\gamma(x_c, y) = -0.0367783 - 0.0492097y + 3.20374y^2$. When $y = 0.115099$, $f_\gamma(x_c, y) = 0$. The corresponding drift is given as

$\Delta f_\gamma(x_c, y = 0.115) = (-0.0492097y + 6.40748y^2)(\frac{\Delta y}{y}) = 0.0792206(\frac{\Delta y}{y})$.

F.2 B_1 drift

Assuming we can fix y at the Bessel function limit, we now examine how the relative precession frequency would shift due to the drift of x, Δx. We consider the situation at the critical dressing field, $x_c = 1.188682344$. We have

$$f_\gamma(\Delta x, y \to 0) = B_0 \frac{\gamma_3 J_0(\frac{\gamma_3}{\gamma_n}(x_c - \Delta x)) - \gamma_n J_0(x_c - \Delta x)}{2\pi}$$

$$\approx 4.5679\Delta x \tag{F.14}$$

Fig. F.3 shows the frequency shift $f_\gamma(\Delta x)$ v.s. Δx.
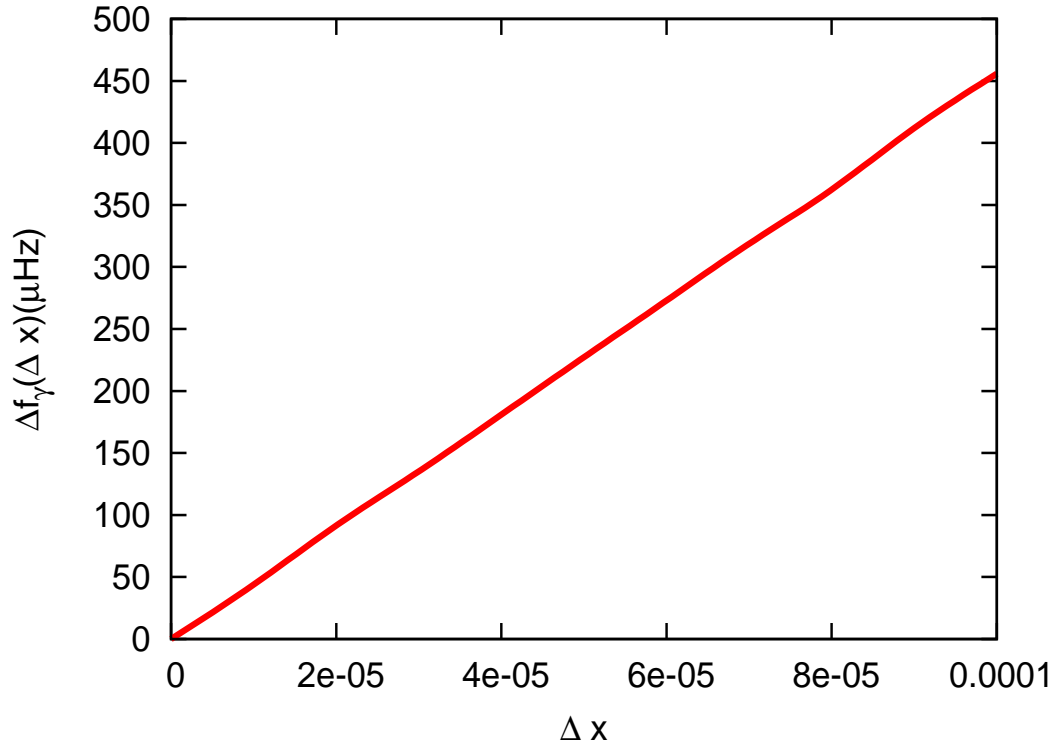
Figure F.3: $f_\gamma(x_c + \Delta x)$ v.s. Δx

If we assume $\Delta x = 5 \times 10^{-5} x_c$, the frequency shift will be $0.000027149 Hz = 271.5 \mu Hz$. If we need to fix at the critical point at less than 1 μHz, the Δx has to be smaller than $2 \times 10^{-6} x$.

Comparing Fig. F.3 with Fig. F.1, we conclude that B_1 needs to be much more stable than B_0. It seems a challenge to keep the dressing field very stable. But the requirement is much less severe as long as the two cells experience the same fields.

Figure F.4: $\Delta f_\gamma(\Delta x/x)$ v.s. $\Delta x/x$

APPENDIX G

TIME EVOLUTION OF THE UCN SPIN IF $\omega_E^D \to 0$

Set $\vec{V} = \pm\frac{1}{2}\omega_{z,0}\hat{z} + \frac{1}{2}\omega_a'\hat{x}$, $V = \frac{1}{2}\sqrt{\omega_{z,0}^2 + (\omega_a')^2} \approx \frac{1}{2}\omega_{z,0}$ and define $\epsilon = \omega_a'/\omega_{z,0}$ which is at 1% level.
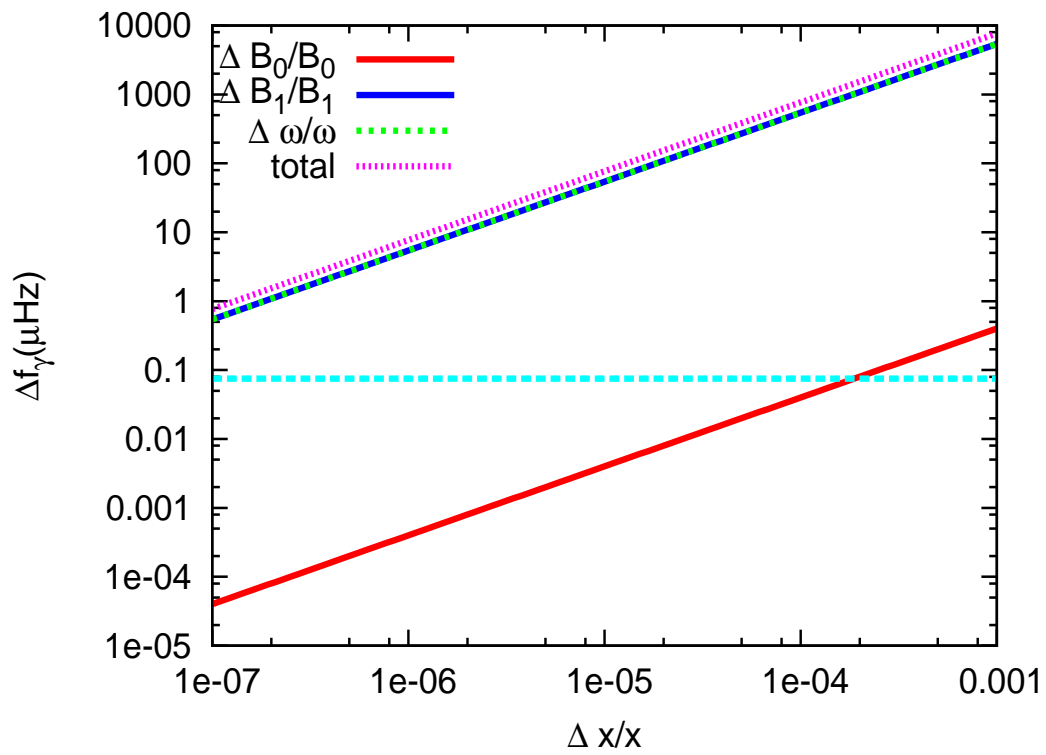Eq. 5.83 becomes

$$U_\pm(\tau) = \exp\left(-i\frac{H_\pm}{\hbar}t\right) = \exp\left(-\frac{1}{2}\frac{t}{\tau_0}\right)\begin{bmatrix} \exp\left(\mp i\frac{1}{2}\omega_{z,0}t\right) & -i\epsilon\sin\frac{1}{2}\omega_{z,0}t \\ -i\epsilon\sin\frac{1}{2}\omega_{z,0}t & \exp\left(\pm i\frac{1}{2}\omega_{z,0}t\right) \end{bmatrix}. \tag{G.1}$$

Apply the field $+\omega_{z,0}$ for time $\tau = \frac{1}{2}\tau_m$ followed by the field $-\omega_{z,0}$ for time τ to produce one modulation period of length $2\tau = \tau_m$. Ignoring ϵ^2 terms, the time-evolution operator for one modulation period τ_m will be

$$U_{-+}(2\tau) = U_-(\tau)U_+(\tau) = \exp\left(-\frac{\tau}{\tau_0}\right)\begin{bmatrix} 1 & -i2\epsilon\exp\left(i\frac{1}{2}\omega_{z,0}\tau\right)\sin\frac{1}{2}\omega_{z,0}\tau \\ -i2\epsilon\exp\left(-i\frac{1}{2}\omega_{z,0}\tau\right)\sin\frac{1}{2}\omega_{z,0}\tau & 1 \end{bmatrix} \tag{G.2}$$

$$\approx \exp\left(-\frac{\tau}{\tau_0}\right)(\hat{I} + b\hat{\sigma}_b) \tag{G.3}$$

where

$$b \equiv -i2\epsilon\sin\frac{1}{2}\omega_{z,0}\tau \quad\text{and}\quad \hat{\sigma}_b \equiv \begin{bmatrix} 0 & \exp\left(i\frac{1}{2}\omega_{z,0}\tau\right) \\ \exp\left(-i\frac{1}{2}\omega_{z,0}\tau\right) & 0 \end{bmatrix}. \tag{G.4}$$

Apply $U_{-+}(2\tau)$ n times and get

$$U_n = (U_{-+}(2\tau))^n = \exp\left(-\frac{n\tau}{\tau_0}\right)(\hat{I} + b\hat{\sigma}_b)^n$$

$$= \exp\left(-\frac{n\tau}{\tau_0}\right)(\hat{I}\frac{1}{2}[(1+b)^n + (1-b)^n] + \hat{\sigma}_b\frac{1}{2}[(1+b)^n - (1-b)^n]). \tag{G.5}$$

Use

$$(1 \pm b)^n = (1 \mp 2i\epsilon\sin(\frac{1}{2}\omega_{z,0}\tau))^n \approx \exp\left(\mp i\epsilon\sin(\frac{1}{2}\omega_{z,0}\tau)\frac{T}{\tau}\right) \equiv \exp\left(\mp i\alpha\right) \tag{G.6}$$

where $n = \frac{T}{2\tau}$ and

$$\alpha \equiv \epsilon \sin(\frac{1}{2}\omega_{z,0}\tau)\frac{T}{\tau} = i\frac{bT}{2\tau}. \tag{G.7}$$

Thus,

$$U_n = \frac{1}{2}\exp\left(-\frac{n\tau}{\tau_0}\right)[\hat{I}[\exp\left(-i\alpha\right) + \exp\left(i\alpha\right)] + \hat{\sigma}_b[\exp\left(-i\alpha\right) - \exp\left(i\alpha\right)]]$$

$$= \frac{1}{2}\exp\left(-\frac{T}{2\tau_0}\right)\begin{bmatrix} F_+ & F_- \exp\left(i\frac{1}{2}\omega_{z,0}\tau\right) \\ F_- \exp\left(-i\frac{1}{2}\omega_{z,0}\tau\right) & F_+ \end{bmatrix} \tag{G.8}$$

where

$$F_\pm \equiv \exp\left(-i\alpha\right) \pm \exp\left(i\alpha\right). \tag{G.9}$$

Consider the cos square wave modulation,

$$U_{tot}(T) = U_n \exp\left(-iH_-\frac{\tau}{2}\right) \approx \frac{1}{2}\exp\left(-\frac{T}{2\tau_0}\right)\begin{bmatrix} F_+ \exp\left(i\frac{1}{4}\omega_{z,0}\tau\right) & F_- \exp\left(i\frac{1}{4}\omega_{z,0}\tau\right) \\ F_- \exp\left(-i\frac{1}{4}\omega_{z,0}\tau\right) & F_+ \exp\left(-i\frac{1}{4}\omega_{z,0}\tau\right) \end{bmatrix} \tag{G.10}$$

The neutron initial states for parallel or antiparallel to ^{3}He which is along to $\hat{x}$-axis are

$$\psi_\pm(0) = \frac{1}{\sqrt{2}}\begin{bmatrix} 1 \\ \pm 1 \end{bmatrix}. \tag{G.11}$$

Then the final state is

$$\psi_\pm(T) = U_{tot}(T)\psi_\pm(0) = \frac{1}{2\sqrt{2}}\exp\left(-\frac{T}{2\tau_0}\right)(F_+ \pm F_-)\begin{bmatrix} \exp\left(i\frac{1}{4}\omega_{z,0}\tau\right) \\ \pm \exp\left(-i\frac{1}{4}\omega_{z,0}\tau\right) \end{bmatrix}. \tag{G.12}$$

The expected value of $\hat{\sigma}_x$ is

$$\langle\sigma_x\rangle_\pm = \psi_\pm^\dagger \sigma_x \psi_\pm = \frac{1}{8}\exp\left(-\frac{T}{\tau_0}\right)|F_+ \pm F_-|^2 (\pm 2\cos(\frac{1}{2}\omega_{z,0}\tau))$$

$$= \pm \exp\left(-\frac{T}{\tau_0}\right)\cos(\frac{1}{2}\omega_{z,0}\tau)\left|\exp\left(\mp i\alpha\right)\right|^2. \tag{G.13}$$

Define

$$\delta \equiv \frac{\sin(\frac{1}{2}\omega_{z,0}\tau)}{\frac{1}{2}\omega_{z,0}\tau}, \ \Omega \equiv \omega_a\delta, \ \text{and} \ \gamma \equiv \frac{P_3}{\tau_3}\delta. \tag{G.14}$$

Calculate

$$\left|\exp\left(\mp i\alpha\right)\right|^2 = \left|\exp\left(\mp i2\frac{T}{2\tau}\frac{\omega_a'}{\omega_{z,0}}\sin\frac{1}{2}\omega_{z,0}\tau\right)\right|^2 = \left|\exp\left(\mp i2\frac{T}{2\tau}\frac{\Omega + i\gamma}{\omega_{z,0}\delta}\sin\frac{1}{2}\omega_{z,0}\tau\right)\right|^2 = \exp\left[\pm\gamma T\right] \tag{G.15}$$

117

The time dependence of $\langle \sigma_x \rangle$ is not affected by the pseudomagnetic field, which is proportional to ω_a. Since

$$\langle \cos \theta_{n3} \rangle = \frac{\int_0^\tau \cos(\frac{1}{2}\omega_{z,0}t)dt}{\tau} = \frac{\sin(\frac{1}{2}\omega_{z,0}\tau)}{\frac{1}{2}\omega_{z,0}\tau} = \delta, \tag{G.16}$$

we can have

$$\langle \sigma_x \rangle_\pm = \pm e^{-\frac{\tau}{\tau_\beta}} e^{-\frac{\tau}{\tau_3}(1\mp P_3)\langle \cos \theta_{n3} \rangle} \cos(\frac{1}{2}\omega_{z,0}\tau). \tag{G.17}$$

APPENDIX H

NOISE ANALYSIS IN THE FEEDBACK SYSTEM

To analyze the feedback loop, a useful tool is the Laplace transform. We use the modulation signal of Eq. 5.102 as the input to the feedback loop. Since its coefficient depends slowly on time, treat $V_0 \equiv \frac{N_0}{\tau_3} e^{-\frac{T}{\tau_0}} P_3 P_n \sin \frac{1}{2} \omega_{z,0} \tau$ as a constant for a short modulation period. The feedback adds a correcting field ω_c so that $\omega_z = \omega_e^d - \omega_c$ becomes the new input. Then the Laplace transform of the input for a unit step $\omega_z u(t)$ [1] is

$$L[V_0 \omega_z t] = V_0 \frac{\omega_z}{s} \frac{1}{s} \equiv L_1(s) \frac{\omega_z}{s} \tag{H.1}$$

where $s = i\omega$, i is the imaginary number $\sqrt{-1}$. The correcting field ω_c is

$$\omega_c = \beta \cdot V_0 \omega_z t + \alpha \int_0^t V_0 \omega_z \tau d\tau, \tag{H.2}$$

$$L[\omega_c] = \beta L_1(s) \frac{\omega_z}{s} + \frac{\alpha}{s} L_1(s) \frac{\omega_z}{s} \equiv L_2(s) L_1(s) \frac{\omega_z}{s}. \tag{H.3}$$

So that the gain is

$$H(s) = \frac{\omega_c(s)}{\omega_e^d/s} = \frac{L_2 L_1 \omega_z/s}{\omega_z/s + \omega_c(s)} = \frac{L_2 L_1 \omega_z/s}{\omega_z/s + L_2 L_1 \omega_z/s} = \frac{L_2 L_1}{1 + L_2 L_1} = \frac{\beta V_0 s + \alpha V_0}{s^2 + \beta V_0 s + \alpha V_0}. \tag{H.4}$$

The natural frequency is

$$\omega_n = \sqrt{\alpha V_0}, \tag{H.5}$$

and the damping factor is

$$\zeta = \frac{1}{2} \sqrt{\frac{\beta^2 V_0}{\alpha}}. \tag{H.6}$$

Finally the gain is

$$H(s) = \frac{2\zeta \omega_n s + \omega_n^2}{s^2 + 2\zeta \omega_n s + \omega_n^2}. \tag{H.7}$$

---

[1] $u(t) = 1$ if $t > 0$; $u(t) = 0$ if $t < 0$.

Using the final value theorem [2], one obtain

$$\lim_{t\to\infty} \omega_c(t) = \lim_{s\to 0}[s\omega_c(s)] = \lim_{s\to 0}[s(H(s)\frac{\omega_e^d}{s})] = \omega_e^d. \tag{H.8}$$

It shows at sufficiently long period (long than the inversus of the loop natural frequency), the loop tracks the input variables exactly. If a white noise $n(t)$ is added to the input as

$$V_i(t) = V_0\omega_e^d t + n(t). \tag{H.9}$$

The Laplace transform gives

$$\frac{V_i(s)}{s} = \frac{V_0\omega_e^d/s}{s} + \frac{n(s)}{s} = \frac{V_0}{s}(\frac{\omega_e^d}{s} + \frac{n(s)}{V_0}) \equiv \frac{V_0}{s}(\frac{\omega_e^d}{s} + \frac{n_i}{s}) \tag{H.10}$$

where $n_i = \frac{s}{V_0}n$. The variance of n_i is

$$\sigma_{n_i}^2 = \frac{|s|^2\sigma_n^2}{V_0^2}, \tag{H.11}$$

and the variance of n_o is

$$\sigma_{n_o}^2 = \sigma_{n_i}^2 H^2(s) = \frac{|s|^2}{V_0^2}\sigma_n^2 H^2(s). \tag{H.12}$$

For sufficiently small ω,

$$\sigma_{n_o}^2 \approx \frac{\omega^2}{V_0^2}\sigma_n^2. \tag{H.13}$$

On the other hand, the variation in scintillation rate Φ_0 in a time T is

$$\delta\Phi_0 = \sqrt{\Phi_0/T}. \tag{H.14}$$

The angular frequency bandwidth is $B_i = \pi/T$. The variance of the input white noise is

$$\sigma_n^2 = \frac{(\delta\Phi_0)^2}{\pi/T} = \frac{\Phi_0}{\pi}. \tag{H.15}$$

The variance of n_o is

$$\sigma_{n_o}^2 \approx \frac{\Phi_0}{\pi}\frac{\omega^2}{V_0^2}, \tag{H.16}$$

---

[2]The theorem can be referred in the wikipedia http://en.wikipedia.org/wiki/Final_value_theorem.

which is exactly equal to Eq. 6.19 in [29]. The noise analysis shows a quite competitive sensitivity for the dressed spin technique.

REFERENCES

[1] K. Abe et al. Observation of large CP violation in the neutral b meson system. *Phys. Rev. Lett.*, 87(9):091802, Aug 2001.

[2] R. Alarcon et al. nedm magnetic fields and magnetic shielding preliminary design. *nEDM Collaboration internal note*, 2008.

[3] L. Alvarez and F. Bloch. A Quantitative Determination of the Neutron Moment in Absolute Nuclear Magnetons. *Physical Review*, 57(2):111–122, January 1940.

[4] B. Aubert et al. Observation of CP violation in the b^0 meson system. *Phys. Rev. Lett.*, 87(9):091801, Aug 2001.

[5] C. A. Baker et al. An improved experimental limit on the electric dipole moment of the neutron. *Phys. Rev. Lett.*, 97:131801, 2006.

[6] V. Baluni. CP-nonconserving effects in quantum chromodynamics. *Phys. Rev. D*, 19(7):2227–2230, Apr 1979.

[7] S. M. Barr. Natural class of non-peccei-quinn models. *Phys. Rev. D*, 30(8):1805–1811, Oct 1984.

[8] S. M. Barr. Solving the strong CP problem without the peccei-quinn symmetry. *Phys. Rev. Lett.*, 53(4):329–332, Jul 1984.

[9] E. Beise. Revisiting the EDM sensitivity. *nEDM Collaboration Meeting*, Feb. 2009.

[10] J. S. Bell. Time Reversal in Field Theory. *Royal Society of London. Series A, Mathematical and Physical Sciences*, 231(1187):479–495, 1955.

[11] F. Bloch. Nuclear induction. *Phys. Rev.*, 70(7-8):460–474, Oct 1946.

[12] D. Budker and et al. A New Search for the Neutron Electric Dipole Moment. page 41, 2002.

[13] N. Cabibbo. Unitary symmetry and leptonic decays. *Phys. Rev. Lett.*, 10(12):531–533, Jun 1963.

[14] Hai-Yang Cheng. The strong CP problem revisited. *Physics Reports*, 158(1):1 – 89, 1988.

[15] Y. Chibane, S. K. Lamoreaux, J. M. Pendlebury, and K. F. Smith. Minimum variance of frequency estimations for a sinusoidal signal with low noise. *Measurement Science and Technology*, 6(12):1671, 1995.

[16] J. H. Christenson, J. W. Cronin, V. L. Fitch, and R. Turlay. Evidence for the 2π decay of the $k2$ meson. *Phys. Rev. Lett.*, 13(4):138–140, Jul 1964.

[17] P.-H. Chu, A. Esler, J. Peng, D. Beck, D. Chandler, S Clayton, B.-Z. Hu, S. Ngan, C. Sham, L. So, S Williamson, and J Yoder. Dressed spin of polarized ^{3}He in a cell. *Physical Review C*, 84(2):1–4, August 2011.

[18] P.-H. Chu and J. C. Peng. Statistical sensitivity with dressed spin. *nEDM Collaboration Meeting*, May 2009.

[19] C. Cohen-Tannoudji. Cargèse *Lectures in Physics edited by M. Jean.* Gordon and Breach, New York, 1968.

[20] C. Cohen-Tannoudji and S. Haroche. Absorption et diffusion de photons optiques par un atome en interaction avec des photons de radiofréquence. *J. Phys. France*, 30(2-3):153–168, 1969.

[21] C. Cohen-Tannoudji and S. Haroche. Interprétation quantique des diverses résonances observées lors de la diffusion de photons optiques et de radiofréquence par un atome. *J. Phys. France*, 30(1):125–144, 1969.

[22] F. D. Colegrove, L. D. Schearer, and G. K. Walters. Polarization of ^{3}He gas by optical pumping. *Phys. Rev.*, 132(6):2561–2572, Dec 1963.

[23] R.J. Crewther, P. Di Vecchia, G. Veneziano, and E. Witten. Chiral estimate of the electric dipole moment of the neutron in quantum chromodynamics. *Physics Letters B*, 88(1-2):123 – 127, 1979.

[24] D. Thompson. An estimate of the uncertainty due to counting statistics in a novel type of neutron EDM experiment. *J. Phys. I France*, 2(3):241–245, 1992.

[25] J. Dunkley et al. Five-Year Wilkinson Microwave Anisotropy Probe (WMAP) Observations: Likelihoods and Parameters from the WMAP data. *Astrophys. J. Suppl.*, 180:306–329, 2009.

[26] A. Esler, J. C. Peng, D. Chandler, D. Howell, S. K. Lamoreaux, C. Y. Liu, and J. R. Torgerson. Dressed spin of ^{3}He. *Phys. Rev. C*, 76(5):051302, Nov 2007.

[27] F. M. Gardner. *Phaselock Techniques.* Wiley-Interscience; 3 edition, 2005.

[28] R. J. Glauber. Coherent and incoherent states of the radiation field. *Phys. Rev.*, 131(6):2766–2788, Sep 1963.

[29] R. Golub and S. K. Lamoreaux. Neutron electric dipole moment, ultracold neutrons and polarized ^{3}He. *Phys. Rept.*, 237:1–62, 1994.

[30] R. Golub and J. M. Pendlebury. Super-thermal sources of ultra-cold neutrons. *Physics Letters A*, 53(2):133 – 135, 1975.

[31] R. Golub and J. M. Pendlebury. The interaction of ultra-cold neutrons (ucn) with liquid helium and a superthermal ucn source. *Physics Letters A*, 62(5):337 – 339, 1977.

[32] R. Golub, D. Richardson, and S.K Lamoreaux. *Ultra-Cold Neutrons.* Taylor and Francis, 1991.

[33] K. Green, P. G. Harris, P. Iaydjiev, D. J. R. May, J. M. Pendlebury, K. F. Smith, M. van der Grinten, P. Geltenbort, and S. Ivanov. Performance of an atomic mercury magnetometer in the neutron EDM experiment. *Nuclear Instruments and Methods in Physics Research Section A: Accelerators, Spectrometers, Detectors and Associated Equipment*, 404(2-3):381 – 393, 1998.

[34] W. C. Griffith, M. D. Swallows, T. H. Loftus, M. V. Romalis, B. R. Heckel, and E. N. Fortson. Improved limit on the permanent electric dipole moment of ^{199}Hg. *Phys. Rev. Lett.*, 102(10):101601, Mar 2009.

[35] S. Haroche and C. Cohen-Tannoudji. Resonant transfer of coherence in nonzero magnetic field between atomic levels of different *g* factors. *Phys. Rev. Lett.*, 24(18):974–978, May 1970.

[36] P. G. Harris. The Neutron EDM Experiment. *arXiv*, hep-ex(0709.3100), 2007.

[37] W. W. Havens, I. I. Rabi, and L. J. Rainwater. Interaction of neutrons with electrons in lead. *Phys. Rev.*, 72(7):634–636, Oct 1947.

[38] T. Ito and the nEdm Collaboration. Plans for a Neutron EDM Experiment at SNS. *Journal of Physics: Conference Series*, 69:012037, May 2007.

[39] K. Jungmann. Searches for permanent electric dipole moments. 2007.

[40] I. B. Khriplovich and S. K. Lamoreaux. *CP Violation Without Strangeness*. Springer, 2004.

[41] D. Kleinman and G. Snow. The Index of Refraction for Neutrons. *Physical Review*, 82(6):952–952, June 1951.

[42] M. Kobayashi and T. Maskawa. *CP* violation in the renormalizable theory of weak interaction. *Prog. Theor. Phys.*, 49:652–657, 1973.

[43] S. K. Lamoreaux. The electric dipole moments of atoms: Limits on P, T violating interactions within the atom. *Nuclear Instruments and Methods in Physics Research Section A: Accelerators, Spectrometers, Detectors and Associated Equipment*, 284(1):43–49, November 1989.

[44] S. K. Lamoreaux. Estimation of the sensitivity of the neutron edm experiment when spin dressing is employed. *nEDM Internal Note*, Apr. 6 2009.

[45] L. Landau. On the conservation laws for weak interactions. *Nuclear Physics*, 3(1):127 – 131, 1957.

[46] G. Larders. Proof of the *TCP* theorem. *Annals of Physics*, 2:1–15, 1957.

[47] T. Lee and C. Yang. Question of Parity Conservation in Weak Interactions. *Physical Review*, 104(1):254–258, October 1956.

[48] W. Lorenzon, T. R. Gentile, H. Gao, and R. D. McKeown. NMR calibration of optical measurement of nuclear polarization in ^{3}He. *Phys. Rev. A*, 47(1):468–479, Jan 1993.

[49] D. D. McGregor. Transverse relaxation of spin-polarized ^{3}He gas due to a magnetic field gradient. *Phys. Rev. A*, 41(5):2631–2635, Mar 1990.

[50] Douglas McGregor. Transverse relaxation of spin-polarized $\hat{\,}\{3\}$He gas due to a magnetic field gradient. *Physical Review A*, 41(5):2631–2635, March 1990.

[51] E. Muskat, D. Dubbers, and O. Schärpf. Dressed neutrons. *Phys. Rev. Lett.*, 58(20):2047–2050, May 1987.

[52] D. V. Nanopoulos, A. Yildiz, and P. H. Cox. On the electric dipole moment of the neutron. *Physics Letters B*, 87(1-2):53 – 56, 1979.

[53] nEDM Collaboration. Conceptual desidn report. 2007.

[54] A. Nelson. Calculation of $\bar{\theta}$. *Physics Letters B*, 143(1-3):165 – 170, 1984.

[55] A. Nelson. Naturally weak *CP* violation. *Physics Letters B*, 136(5-6):387 – 391, 1984.

[56] T. G. Nichols, D. Beck, and S. Williamson. Determining the polarization of ^{3}He by means of an optical technique. *DNP08 Bulletin*, DA.00073, 2008.

[57] L. Passell and R. I. Schermer. Measurement of the spin dependence of the ^{3}He$(n,\ p)t$ reaction and of the nuclear susceptibility of adsorbed ^{3}He. *Phys. Rev.*, 150(1):146–151, Oct 1966.

[58] R. D. Peccei and Helen R. Quinn. Constraints imposed by *CP* conservation in the presence of pseudoparticles. *Phys. Rev. D*, 16(6):1791–1797, Sep 1977.

[59] R. D. Peccei and Helen R. Quinn. *CP* conservation in the presence of pseudoparticles. *Phys. Rev. Lett.*, 38(25):1440–1443, Jun 1977.

[60] J. M. Pendlebury. Peoples and events. *Physics World*, (Dec):55 –59, 1989.

[61] J. M. Pendlebury. Steps to improve the measurement of the neutron electric dipole moment. *Nuclear Physics A*, 546(1-2):359–368, August 1992.

[62] J. C. Peng. Neutron electric dipole moment experiments. *Modern Physics Letters A*, 23(17 & 20):1397, April 2008.

[63] N. Polonsky and C. Cohen-Tannoudji. Interprétation quantique de la modulation de fréquence. *J. Phys. France*, 26(7):409–414, 1965.

[64] H. R. Poolman, J. F. J. van den Brand, H. J. Bulten, M. Doets, R. Ent, M. Ferro-Luzzi, D. G. Geurts, M. Harvey, and F. A. Mul. A polarized 3he internal target for storage rings. *Nuclear Instruments and Methods in Physics Research Section A: Accelerators, Spectrometers, Detectors and Associated Equipment*, 439(1):91 – 110, 2000.

[65] E. Purcell and N. F. Ramsey. On the Possibility of Electric Dipole Moments for Elementary Particles and Nuclei, June 1950.

[66] I. I. Rabi. Space quantization in a gyrating magnetic field. *Phys. Rev.*, 51(8):652–654, Apr 1937.

[67] N. F. Ramsey. A New Molecular Beam Resonance Method. *Physical Review*, 76(7):996–996, October 1949.

[68] N. F. Ramsey. A new molecular beam resonance method. *Phys. Rev.*, 76(7):996, Oct 1949.

[69] N. F. Ramsey. A molecular beam resonance method with separated oscillating fields. *Phys. Rev.*, 78(6):695–699, Jun 1950.

[70] N. F. Ramsey. *Molecular Beams*. Oxford University Press, New York, 1956.

[71] N. F. Ramsey. Feasibility of a3He magnetometer for neutron electric dipole moment experiments. *ACTA PHYSICA HUNGARICA*, 55(1-4):117–126, 1984.

[72] N. F. Ramsey and H. Silsbee. Phase Shifts in the Molecular Beam Method of Separated Oscillating Fields. *Physical Review*, 84(3):506–507, November 1951.

[73] M.J. Ramsey-Musolf. Neutrons and the new Standard Model. *Nuclear Instruments and Methods in Physics Research Section A: Accelerators, Spectrometers, Detectors and Associated Equipment*, 611(2-3):111–116, December 2009.

[74] A. D. Sakharov. Violation of CP Invariance, c Asymmetry, and Baryon Asymmetry of the Universe. *Pisma Zh. Eksp. Teor. Fiz.*, 5:32–35, 1967.

[75] J. J. Sakurai. *Advanced Quantum Mechanics*. Addison Wesley, 1967.

[76] J. Schwinger. The Theory of Quantized Fields. I. *Physical Review*, 82(6):914–927, June 1951.

[77] V. F. Sears. Electromagnetic neutron-atom interactions. *Physics Reports*, 141(5):281 – 317, 1986.

[78] V. F. Sears. Neutron scattering lengths and cross sections. *Neutron News*, 3(3):26–37, June 1992.

[79] E. P. Shabalin. The electric dipole moments of baryons in the Kobayashi-Maskawa CP noninvariant theory. *Sov. J. Nucl. Phys.*, 32:228, 1980.

[80] F. L. Shapiro. Electric dipole moments of elementary particles. *Soviet Physics Uspekhi*, 11(3):345–352, March 1968.

[81] J. H. Shirley. Solution of the schrödinger equation with a hamiltonian periodic in time. *Phys. Rev.*, 138(4B):B979–B987, May 1965.

[82] C. G. Shull and R. Nathans. Search for a neutron electric dipole moment by a scattering experiment. *Phys. Rev. Lett.*, 19(7):384–386, Aug 1967.

[83] C. P. Slichter. *Principles of Magnetic Resonance*. Springer, 1996.

[84] J. H. Smith, E. M. Purcell, and N. F. Ramsey. Experimental limit to the electric dipole moment of the neutron. *Phys. Rev.*, 108(1):120–122, Oct 1957.

[85] J. Stark. Beobachtungen er den Effekt des elektrischen Feldes auf Spektrallinien. I. Quereffekt. *Annalen der Physik*, 348(7):965–982, 1914.

[86] S. Williamson. Helium-3 services. *nEDM Collaboration internal note*, 2008.

[87] C. S. Wu, E. Ambler, R. W. Hayward, D. D. Hoppes, and R. P. Hudson. Experimental Test of Parity Conservation in Beta Decay. *Physical Review*, 105(4):1413–1415, February 1957.

[88] T. Yabuzaki, S. Nakayama, Y. Murakami, and T. Ogawa. Interaction between a spin-1/2 atom and a strong rf field. *Phys. Rev. A*, 10(6):1955–1963, Dec 1974.

[89] E. Zavattini, G. Zavattini, G. Ruoso, E. Polacco, E. Milotti, M. Karuza, U. Gastaldi, G. Di Domenico, F. Della Valle, R. Cimino, S. Carusotto, G. Cantatore, and M. Bregant. Experimental observation of optical rotation generated in vacuum by a magnetic field. *Phys. Rev. Lett.*, 96(11):110406, Mar 2006.

[90] E. Zavattini, G. Zavattini, G. Ruoso, E. Polacco, E. Milotti, M. Karuza, U. Gastaldi, G. Di Domenico, F. Della Valle, R. Cimino, S. Carusotto, G. Cantatore, and M. Bregant. Editorial note: Experimental observation of optical rotation generated in vacuum by a magnetic field [phys. rev. lett. 96, 110406 (2006)]. *Phys. Rev. Lett.*, 99(12):129901, Sep 2007.

[91] O. Zimmer, G. Ehlers, B. Farago, H. Humblot, W. Ketter, and R. Scherm. A precise measurement of the spin-dependent neutron scattering length of ^{3}he. *EPJ direct*, 4:1–28, 2002. 10.1007/s1010502a0001.